AWARD NUMBER: W81XWH-16-1-0073

TITLE: Targeting Breast Cancer Micrometastases: To Eliminate the Seeds of Evil

PRINCIPAL INVESTIGATOR: Xiang Zhang

CONTRACTING ORGANIZATION: Baylor College of Medicine
Houston, TX 77030

REPORT DATE: April 2019

TYPE OF REPORT: Annual

PREPARED FOR: U.S. Army Medical Research and Materiel Command
Fort Detrick, Maryland 21702-5012

REPORT DOCUMENTATION PAGE

Form Approved
OMB No. 0704-0188

1. REPORT DATE	2. REPORT TYPE	3. DATES COVERED
April 2019	Annual	15 March 2018 - 14 March 2019

4. TITLE AND SUBTITLE
Targeting Breast Cancer Micrometastases: To Eliminate the Seeds of Evil

5a. CONTRACT NUMBER

5b. GRANT NUMBER
W81XWH-16-1-0073

5c. PROGRAM ELEMENT NUMBER

6. AUTHOR(S)
Xiang Zhang

E-Mail: xiangz@bcm.edu

5d. PROJECT NUMBER

5e. TASK NUMBER

5f. WORK UNIT NUMBER

7. PERFORMING ORGANIZATION NAME(S) AND ADDRESS(ES)
Baylor College of Medicine
One Baylor Plaza
Houston, TX, 77030

8. PERFORMING ORGANIZATION REPORT NUMBER

9. SPONSORING / MONITORING AGENCY NAME(S) AND ADDRESS(ES)
U.S. Army Medical Research and Materiel Command
Fort Detrick, Maryland 21702-5012

10. SPONSOR/MONITOR'S ACRONYM(S)

11. SPONSOR/MONITOR'S REPORT NUMBER(S)

12. DISTRIBUTION / AVAILABILITY STATEMENT
Approved for Public Release; Distribution Unlimited

13. SUPPLEMENTARY NOTES

14. ABSTRACT A substantial proportion of breast cancer patients develop metastases despite surgeries and adjuvant therapies. Metastasis is incurable and responsible for over 90% of breast cancer-related death. Thus, the prevention of metastasis is an imperative clinical need. We seek to understand how microscopic metastases in distant organs (e.g., bone), before becoming overt malignancies, survive and progress by interacting with specific normal cells in that organ. The rationale is that such interaction may confer resistance to current adjuvant therapies and may also render the cancer cells vulnerable to novel treatments. To date, very few pre-clinical models of micrometastases exist. We have filled this gap by developing a series of techniques that allow us to monitor and quantitate the progression of micrometastases. In this application, we will further establish the authenticity of these models in reflecting biological properties of micrometastases. We will also use them to identify therapies that may eliminate metastatic seeds, especially in the bone. We will examine all breast cancer subtypes with an emphasis on estrogen receptor-positive breast cancer and investigate how the bone environment influences cancer cells' response to endocrine therapies. Specifically the three goals are: 1) To assess the differential responses of bone micrometastases to adjuvant therapies as compared to their parental tumors in the mammary gland, and dissect if and how such differences are attributable to the interaction with their adjacent normal cells.; 2) to further establish an experimental platform called "Bone-in-culture array" (BICA) that can mimic bone micrometastases and allow rapid testing of drug efficacies; and 3) to perform drug screening/discoveries to identify compounds that can be combined with current standard-of-care and eradicate bone micrometastases. The fulfillment of these goals will provide novel strategies that may significantly reduce bone or possibly other metastases in breast cancer. Moreover, the same techniques can be easily applied to other cancer, including lung cancer and some pediatric sarcomas.

15. SUBJECT TERMS

16. SECURITY CLASSIFICATION OF:			17. LIMITATION OF ABSTRACT	18. NUMBER OF PAGES	19a. NAME OF RESPONSIBLE PERSON
a. REPORT	b. ABSTRACT	c. THIS PAGE			USAMRMC
Unclassified	Unclassified	Unclassified	Unclassified	11	19b. TELEPHONE NUMBER *(include area code)*

Table of Contents

Page

1. Introduction

In this project we aim to overcome the challenge of eliminating microscopic metastases of breast cancer, so that distant recurrences and related deaths can be significantly reduced in the foreseeable future. We will focus on bone micrometastases (BMM), which are precursors of overt bone metastases and possibly other metastases. In particular, we will delineate how breast cancer cells, when isolated in small quantity in a foreign milieu, react to therapies differently compared to the original primary tumor. We have designed and will continue to optimize various pre-clinical models to investigate the microenvironmental effects on BMM. These models will enable medium-throughput drug discovery/repositioning to expedite the elimination of breast cancer cells in the context of bone. The methodology may also be applied to metastases in other sites.

In the clinic, primary breast tumors are usually surgically removed soon after diagnosis, often leaving patients "tumor-free". However, 20-40% of breast cancer survivors will eventually suffer metastasis to distant organs, sometimes years after surgeries. Thus, the life-threatening enemy is typically not the bulk of primary tumors, but the dispersed metastatic seeds left behind, which have already disseminated to distant organs, may be temporarily dormant, and may resume aggressive outgrowth under certain yet-to-be-identified conditions. Current adjuvant therapies intend to eliminate these cells. However, the therapeutic decisions and strategies are usually based upon pathological features of primary tumors. Micrometastases are likely to differ from their parental primary tumors due to Darwinian selection and/or adaptation in a different milieu. In either case, the microenvironment in distant organs plays a critical role in driving the selection and/or in shaping the adaptive reaction of cancer cells. It is our vision that a critical barrier in curing breast cancer is the lack of knowledge about micrometastases and their microenvironment niches. Specifically, the key questions are the nature of the supporting pathways uniquely induced by cancer-niche interaction, and the mechanisms responsible for differential therapeutic responses as compared to parental primary tumors. To overcome this barrier, I propose to establish a series of pre-clinical models that recapitulate the cellular nature of micrometastases, mimic their habitat and allow expedited testing of their drug responses.

Three specific aims will be pursued. 1. To assess the differential responses of BMM to adjuvant therapies as compared to their parental tumors in the mammary gland, and dissect if and how such differences are attributable to the interaction with the microenvironment niche. 2. To establish the bone-in-culture array (BICA) platform, which aims to faithfully recapitulate the molecular profile, cell-biological behaviors, microenvironment niche, and therapeutic responses of BMM in vivo, and is amenable to medium-to-high throughput drug discovery/screening. 3. To identify and mechanistically investigate therapies against BMM by analyzing the omics data obtained from previous goals, and by screening pre-established libraries of FDA-approved drugs or small molecule inhibitors (SMIs).

2. Keywords:

Metastasis, microenvironment, drug discovery, therapeutic resistance, micrometastases, endocrine resistance

3. Accomplishment

Major Task 1 : Differential drug responses of bone micrometastases (BMM) as compared to the parental orthotopic tumors

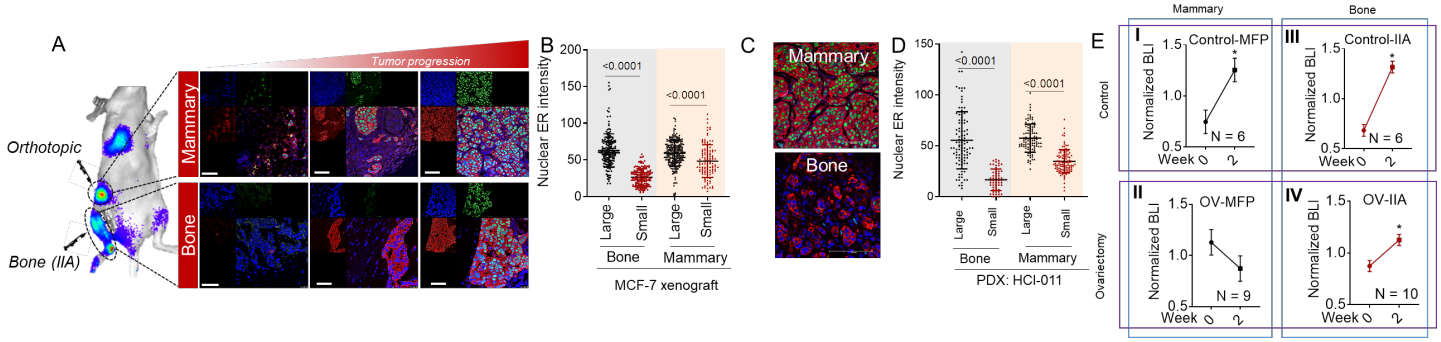

Figure 1: Bone microenvironment induces transient downregulation of ERα. (A) Left: schematic shows simultaneous transplantation of MCF-7 cells as orthotopic mammary tumors and bone lesions (through intra-iliac artery injection, or IIA) into the same

animal. Right: representative immunofluorescence staining of ERα (green) and cytokeratin 8 (red) on mammary tumors and bone lesions of different sizes. Scale bars, 100 μm. **(B)** Quantification of nuclear staining of ERα in mammary tumors and bone lesions of different sizes. Each point is a cell. Results are based on 3 animals in each group. **(C)** Mammary tumors and bone lesions derived from an ER+ PDX (HCI-011) are subjected to the same staining shown in (A). Scale bars, 100 μm. **(D)** The same as (B) except for HCI-011. **(E)** The growth of orthotopic MCF-7 tumors in mammary glands (I and II) or in bone as transplanted by intra-iliac artery injection (IIA) (III and IV) in control animals (I and III) or overiectomized (OV) animals (II and IV). A preliminary version of this data was shown in last year's report with smaller sample sizes.

Subtask 1: Tumor burden measurement (Month 1-24). We expect to use five PDXs (2 ER+, 1 Her2+ and 2 triple negative) and five cell lines (the same subtype distribution). The total # of models will be 10. Each model will need 55 mice. PDXs will be transplanted into SCID/Beige mice and cell lines will be transplanted into Athymic nu/nu mice. These mice will be divided into treated and untreated. Treatments: tamoxifen, fulvestrant, ovariectomy, and lapatinib. Measurement: Weekly bioluminescence imaging and tumor volume measurement. Some mice will be euthanized at intermediate time points for Subtasks 2 and 3 below.

This subtask has been accomplished, and a figure containing representative data is shown above. Through this study, we revealed a striking effect of bone microenvironment on expression of ER as well as responses to endocrine therapies in ER+ breast cancer models. Briefly, the bone microenvironment downregulates ER expression in bone micrometastases (BMMs) (Figure 1A-D) and confers resistance to endocrine therapies (Figure 1E). This downregulation is reversed when metastases progress to the osteolytic, macroscopic stage, although endocrine resistance may still partially persist. This finding is clinically relevant because it may partly address the long-standing question of why some ER+ tumors recur despite adjuvant endocrine therapies. These observations will be further studied to delineate underlying mechanisms. As will be mentioned in the "Change and Problem" section, we will adjust our plan to focus on this in subsequent grant years.

Subtask 2: Immunofluorescence staining to quantitate proliferation (e.g., Ki67+), survival (e.g., CC3) and self renewal (e.g., retention of H2B-GFP) (Month 1-18).

This subtask was deprioritized due to our discovery of a more interesting phenomenon related gap junctions formed between cancer cells and osteoblasts. In brief, we identified connexin 43 as one of the most upregulated genes in bone micrometastases as compared to orthotopic tumors both in clinical specimens and in experimental system. In the past year, we further demonstrated that the gap junction between cancer cells and the osteoblasts mediates calcium ion diffusion from osteoblasts to cancer cells, which activates the calcium-signaling network in cancer cells. This alteration confers on cancer cell proliferative advantage, and also leads to unexpected vulnerability to some novel therapies. These findings have been published on *Cancer Cell*, and a summery cartoon is shown below.

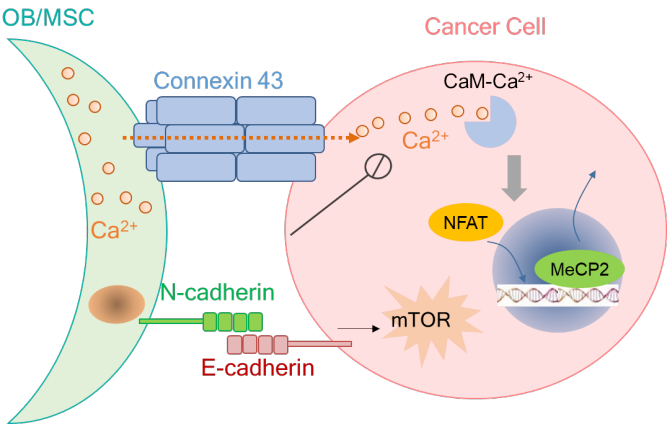

Figure 2. Schematic model for interaction between osteogenic cells and cancer cells in bone colonization.

Major Task 2: Test if the abolishment of cancer-niche interaction in conditional N-cadherin KO mice reverses the therapeutic responses of BMM.

Subtask 1: Mouse breeding to generate animals with various genetic background (including immunodeficiency). We will breed TetO-Osx-cre-GFP with $Cdh2^{f/f}$ mice both purchased from Jackson Laboratories (Stock No: 006361 and 007611, respectively) to generate offsprings with both genetic alterations. The mice will also be crossed with Rag1-/- mice (Stock No: 002216) to generate immunodeficiency for human cancer cell transplantation. (Month 1-24).

As mentioned in last year's report, this work has been finished and the resultant mouse colonies are being expanded for future experiments. However, it should be noted here that the discovery of gap junction between cancer cells and osteoblasts has prompted us to switch our approach from depletion of N-cadherin to inhibition of gap junction. This strategy worked well and helped us identify an essential role of gap junctions in mediating crosstalk between BMM and the osteogenic niche (see Figure 2 for a summary, and Figure 3 in subsequent section for more data).

Subtask 2: Repeat experiments in Major Task 1 in the conditional N-cadherin KO models, and Test if the abolishment of cancer-niche interaction in conditional N-cadherin KO mice reverses the therapeutic responses of BMM. TetO-Osx-cre-GFP; Cdh2$^{f/f}$ mice and TetO-Osx-cre-GFP; Cdh2f/f; Rag1-/- mice and their littermate female mice lacking Osx-Cre will be subjected to experiments as in Task #1. About 700 mice will be bred at this stage. Except that a few male mice carrying the wanted phenotype will be kept for strain maintaining, most male mice (estimated to be 340) will be euthanized right after genotyping. (Month 24-36)

As stated above, we have deprioritize the usage of N-cadherin KO mice, but prioritize the usage of connexin 43 KO mice. As a result, we have successfully derived TetO-Osx-cre-GFP; Gja1f/f mice (Gja1 is the gene encoding connexin 43). Representative results are shown below in Figure 3, which confirmed an important role of gap junction in early stage bone colonization.

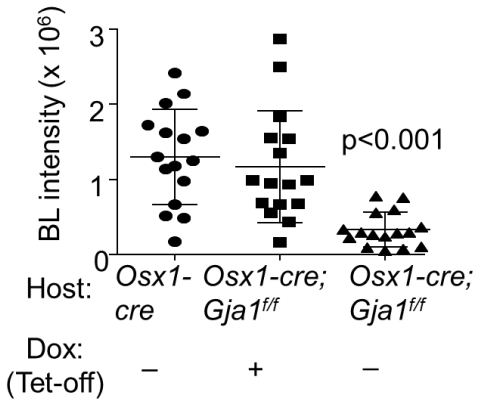

Figure 3. The effect of inducible condition knockout (KO) of *Gja1* in Osx$^+$ lineage cells on MCF7 cell growth in bone microenvironment. The experimental group, *Osx1-GFP::Cre*;*Gja1*$^{f/f}$ (*Osx1-cre;Gja1*$^{f/f}$) animals with doxycycline withdrawn (KO induced), are compared to control groups, *Osx1-GFP::Cre* (*Osx1-cre*) and *Osx1-GFP::Cre*;*Gja1*$^{f/f}$ on doxycycline. n=16 for each group. Representative BL images are shown on the right. p value by one-way ANOVA.

Major Task 3: To establish and validate BICA

Subtask 1 : Characterize the cell-biological features of cancer cells in BICA (e.g., proliferation, self-renewal, and survival). We expect to use five PDXs (2 ER+, 1 Her2+ and 2 triple negative) and five cell lines (the same subtype distribution). The total # of models will be 10. Each model will need 20 mice. PDXs will be transplanted into SCID/Beige mice and cell lines will be transplanted into Athymic nu/nu mice. (Month 1-18)

This task has been finished and a manuscript has been published on Nature Communications (attached to last report). Please refer to last report as well as the publication for detailed results.

Subtask 2: To characterize the microenvironment niche in BICA using different subtypes of cancer models. This will be achieved by immunohistochemical and immunofluorescence staining of the following markers: ALP, Col-I, CTSK, Osterix, Runx2, CD31, NG2, and SOX9. The same numbers and PDXs and cell lines will be used as specified in Subtask 1 above. (Month 1-24).

This subtask has been finished and the exemplar data was shown in our publication on Nature Communications (see last report).

Subtask 3: To perform RNA-seq of cancer cells in BICA, and compared the profiles to cancer cells in intact bones and in mammary glands. For this task we will use 2 PDX (1 ER+ and 1 Her2+) and 2 cell lines (1ER+ and 1 Her2+). Each will be injected into 25 animals (5 for orthotopic tumors, 10 for intact bone metastases, and 10 for BICA). (Month 18-36)

As mentioned above, we have obtained our first batch of results of MCF-7 and a few other models. By sorting human mRNAs and mouse mRNAs, we can "purify" human cells in silico and ask whether BICA recapitulate cancer-intrinsic gene expression profiles of bone micrometastases. Toward this end, we have performed unbiased principle component analysis (PCA) and t-distributed stochastic neighbor embedding (t-SNE). The results were shown in last year's report, and clearly demonstrated the similarity between cancer cells in BICA and in in vivo bone lesions (IVBL), with orthotopic tumors and in vitro cultures as references.

We performed further analyses the mouse reads from the RNA-seq which represent the microenvironment portion of metastases. Using an algorithm called CIBERSORT and reference transcriptomes of major cell populations in the bone microenvironment, we predicted cellular composition of bone metastases in BICA. The results are shown below, which confirmed that 1) the majority of microenvironment cells are osteogenic (mesenchymal stem cells to osteoblasts) both in BICA and in bone lesions in vivo (IVBL), and 2) BICA recapitulates the bone microenvironment, but is very distinctive from primary tumors (Figure 4).

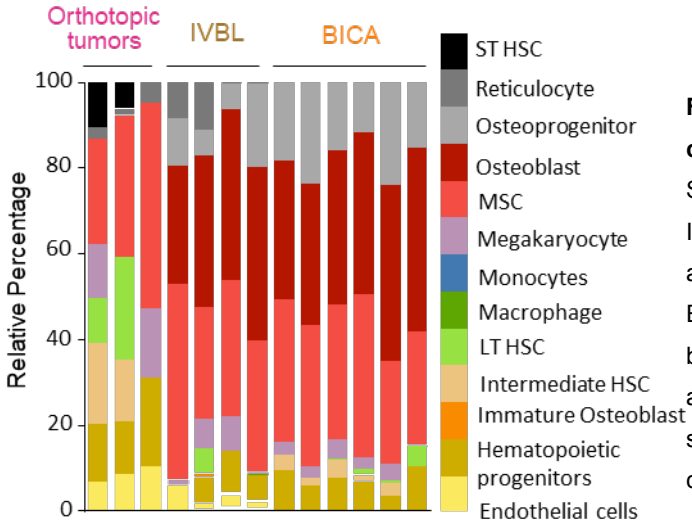

Figure 4. Further analyses of microenvironment composition based on RNA-seq data of BICA. Stromal components of MCF-7 orthotopic tumors, IVBL, and BICA predicted by CYBERSORT algorithm to mouse sequences in RNA-seq results. Each column represents one tumor (orthotopic), one bone (IVBL), or pooled bone segments from one animal (BICA). ST HSC: short-term hematopoietic stem cells. LT HSC: long-term hematopoietic stem cells.

Subtask 4: To determine the therapeutic responses of cancer cells in BICA as compared to those of BMM in vivo and cancer cells in culture. We expect to use five PDXs (2 ER+, 1 Her2+ and 2 triple negative) and five cell lines (the same subtype distribution). The total # of models will be 10. Each model will need 50 mice. PDXs will be transplanted into SCID/Beige mice and cell lines will be transplanted into Athymic nu/nu mice. (Month 30-48)

This effort has already been started and we have generated the first batch of interesting results. We are currently focusing on two questions. First, how do ER+ breast cancer cells respond differently to endocrine therapies in bone microenvironment (BICA and in vivo) as compared to other microenvironment. As previously mentioned, our working hypothesis is that the bone-like microenvironment confers endocrine resistance. This hypothesis will be further evaluated and mechanisms will be pursued in the following grant year. Second, how can gap junctions and calcium signaling (see Figure 1) be targeted to block the effects of osteogenic niche, and facilitate elimination of BMMs. Some results related to the second question are shown below, demonstrating that blockade of gap junctions and calcium signaling appear to have bone-specific effects on cancer cells in BICA as well as in bones.

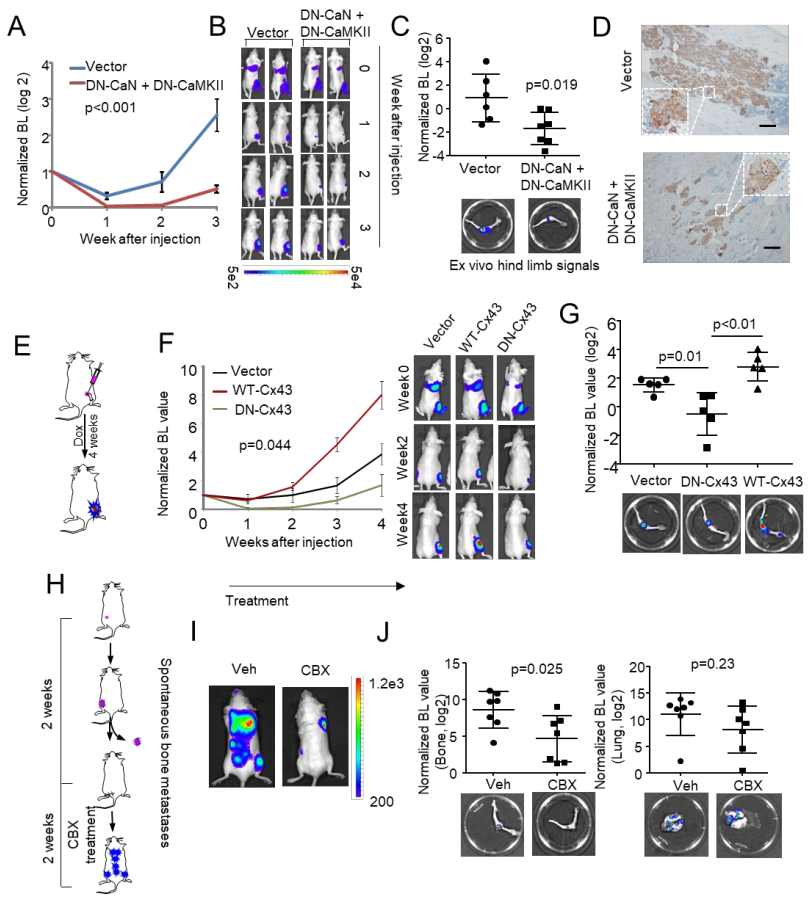

Figure 5. The bone microenvironment confers sensitivity to inhibition of gap junctions and calcium signaling. (A) Bone colonization curves of IIA-injected MCF7 cells, either expressing empty vector or DN-CaN+DN-CaMKII. n=6 and 7 for the two groups, respectively. (B) Represented BL pictures of mice in the vector and DN-CaN+DN-CaMKII (DN) groups. (C) Quantitation of ex vivo BL signals emitted from extracted hind limb bones. Representative pictures are shown. (D) Representative IHC staining of bone lesions derived from (C). Tumor lesions were indicated by K8 (brown) staining. Scale bar, 100 μm. (E) A schematic illustration of experiments assessing the effects of inducible overexpression of WT-Cx43 or DN-Cx43 on bone colonization. (F) Growth curves of IIA-injected MCF7 cells with indicated genetic perturbation in hind limbs. Error bars = S.E.M. n=5 for each group. ges are shown on the right. (G) Nop value by repeated measures ANOVA test across three groups. Representative BL imarmalized, log2-transformed BL intensity of hind limb bones extracted from the three groups described in (F). p value by LSD test. (H) A schematic illustration of experiments assessing the effects of CBX treatment on spontaneous bone metastasis of 4T1.2 cells. (I) Representative BL images of spontaneous metastases two weeks after orthotopic tumor resection. (J) BL intensity of hind limbs and lungs extracted from control and CBX-treated animals. n=7 for each group. p values by Student's t tests.

Major Task 4: Analyze the RNA-seq data obtained from Specific Aim 1 to identify and validate candidate pathway/genes that can be targeted to eliminate BMMs

Subtask 1: Bioinformatics analyses to identify candidate pathways/genes. (Month 1-36)

We have implemented several lines of analyses to identify relevant pathways/genes that may play roles in early stage bone colonization. These analyses are not restricted to data obtained from Specific Aim 1, but also utilized other resources in the literature. Indeed, gap junctions, calcium signaling, and downregulation of ER pathways all emerged as key pathways and genes from these analyses. Specifically, the gene encoding one of the major components of gap junctions, Gja1, is expressed at a significantly higher level in clinical bone metastases, as compared to other metastases in other organs (Figure 6A). It is also one of the most upregulated genes when cancer cells reside in a bone-like microenvironment (Figure 6B). Transcription factors downstream of calcium signaling, NFAT and MEF2, exhibited enhanced activities in bone metastases compared to others (Figure 6C), and were also more active in experimental models recapitulating osteogenic niches (Figure 6D). Finally, downregulation of ER was validated in matched primary tumor-bone metastasis sample pairs (Figure 6E). Going forward, we will follow these leading candidates while continuing to analyze data for new discoveries.

Subtask 2: Select candidates for functional validation in vivo and in BICA. (Month 36-60)

This effort has started and we will deliver results in future reports.

Major Task 5: Screening of small SMI libraries to identify FDA-approved drugs or new compounds that can eliminate BMM.

Subtask 1: Screening using BICA. We will use one ER+ PDX and one ER+ cell lines. Each model will be applied to 100 mice. This will generate approximately 5000 bone fragments, and can be used for screening of small drug libraries described in the proposal. Four libraries and BICA-screening will be performed. (Month 24-36)

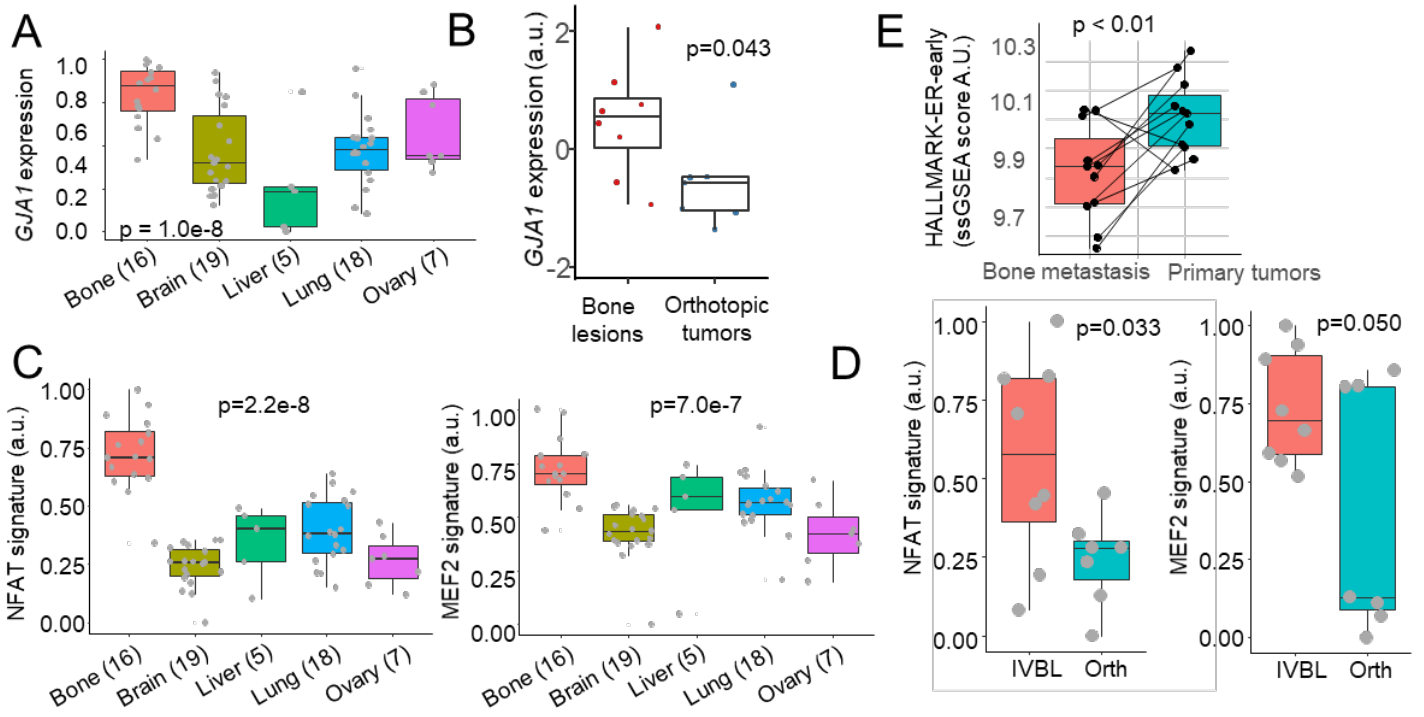

Figure 6. Bioinformatics evidence supporting relevance of gap junction, calcium signaling and down-regulation of ER signaling in bone colonization. (A) Expression of GJA1, the gene encoding Cx43, a major component of gap junctions, across breast cancer metastases in indicated organs. Sample size of each group is shown in parentheses. **(B)** Expression of GJA1 in bone lesions vs. orthotopic mammary tumors in experimental models based on MCF7 cells. **(C)** The expression of NFAT target genes and MEF2 target genes across breast cancer metastases in different organs. The sum of target gene expression indicates activities of these transcription factors downstream of calcium signaling. **(D)** The expression of NFAT and MEF2 signatures in experimental in vivo bone lesions (IVBL) and orthotopic tumors. **(E)** ssGSEA scores of the Hallmark early ER response pathways across 11 matched primary tumor-bone metastasis pairs of human breast cancer patients.

We have finished screening of two small libraries: one contains FDA-approved anti-neoplasm drugs, and the other contains compounds targeting epigenomic modulators. We focused on drugs/compounds that alter cancer cell growth in BICA but not in 2D cell cultures. In each screening, we identified interesting one or more candidates for further analyses. These results are shown below in Figure 7. Specifically, in the first library we identified arsenic trioxide (As2O3) as a drug that can eliminate cancer cells from BICA at a dosage 10-fold lower than that required in 2D cell cultures (Figure 7B). This is interesting as As2O3 is already approved to treat specific leukemia, which also localizes mainly in the bone marrow. In the 2nd screening, we identified an inhibitor of histone methyltransferase, EPZ6438 (in Phase 2 clinical trial for leukemia), which selectively enhance cancer cell growth in BICA (Figure 7C). These candidates are clinically interesting. Their in vivo efficacies were validated (see next subtask). We therefore decided to further investigate them.

Because of the interesting discoveries in the first two screening, we have decided to deprioritize screening of the 3rd and 4th libraries. We propose to conduct more screening later in the project should the need arises for more candidate drugs.

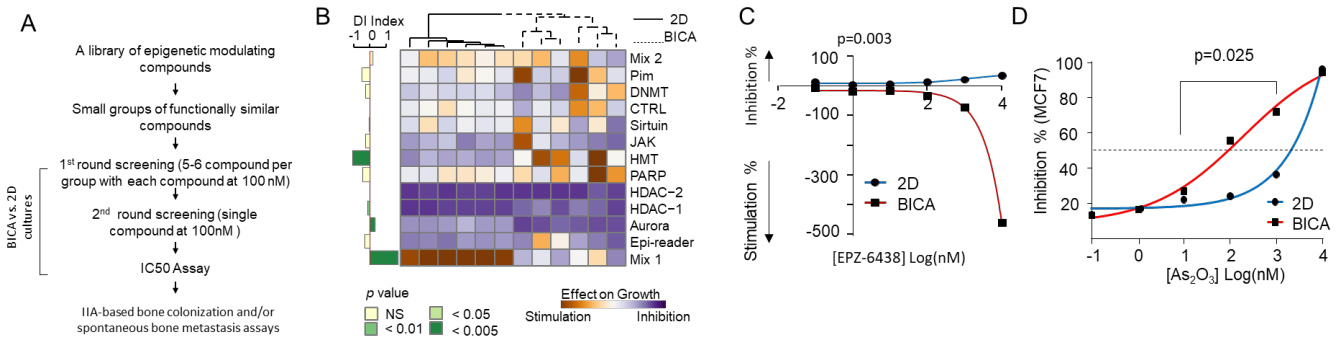

Figure 7. Exemplar data from the BICA-based drug screening using two small libraries. (A) Schematic shows the major steps of parallel 2D/BICA tests to identify compounds with impacts on cancer cells in the bone microenvironment. **(B)** A heat map summarizing the output of first-round testing using groups of functionally related compounds. (See Supplementary Table 1 for detailed information of each group.) MCF-7 samples are under corresponding treatment for 3 weeks and measured by bioluminescence. The differential inhibition (DI) index is obtained by subtracting the 2D inhibition score from BICA inhibition score (BICA - 2D). The positive value means the drug works better in BICA in terms of growth inhibition (e.g. Aurora); the negative value means the drug inhibits cancer cell growth in 2D condition better (e.g. HMT). Each column represents an independent cell culture (2D) or bone fragment (BICA). The p values are determined by two-tailed unpaired Mann–Whitney *U* test. **(C)** Dose responsive curves of MCF-7 cells to EPZ-6438 in 2D culture and BICA. For 2D cultures, three technical replicates were included for each drug concentration. For BICA, N=5 bone fragments for each drug concentration. Samples are under corresponding treatment for 3 weeks and measured by bioluminescence. P values are determined by repeated measures ANOVA tests. **(D)** The same as (C) except for As2O3. Note that the directions of action of As2O3 and EPZ-6438 are opposite.

Subtask 2: Identify and validate the efficacies of top candidates on BMM. We will use the same models as subtask 1. (Month 30-36)

As mentioned before, we have validated the effects of EPZ6438 (Figure 8A) and As2O3 (Figure 8B) in intact animals. Remarkably, we actually further uncovered that the effect of As2O3 is at least partially by calcium signaling, as expression of constitutive activation of CaMKII, a key signaling transducer in calcium pathway, confers resistance to As2O3 (Figure 8B). This not only elucidated mechanisms underlying As2O3's effects but also once again supported the relevance of the calcium signaling.

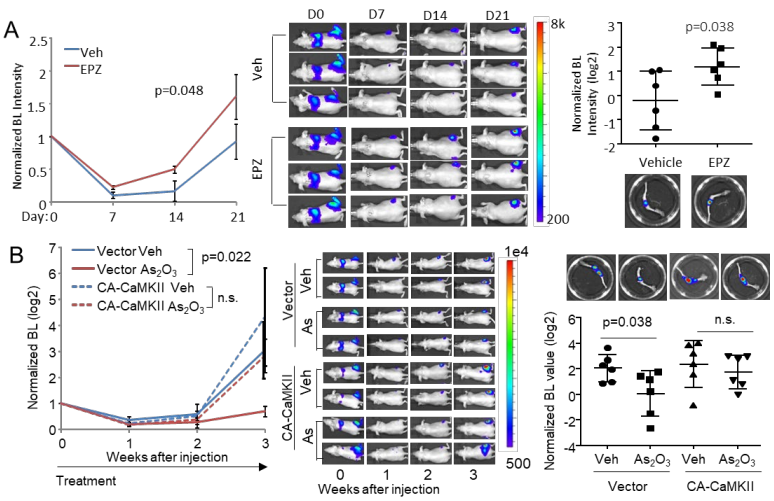

Figure 8. In vivo validation of the effects of EPZ-6438 and As2O3 on bone metastases. (A) The effects of EPZ-6438 on IIA-injected MCF-7 bone lesions. Left: growth curves as measured by *in vivo* BL imaging. N=6 mice per group. P values are determined by repeated measures ANOVA tests on the growth curves. Error bars: S.E.M. Middle: Representative BL pictures show bone lesion arising with or without EPZ-6438 treatment. Right: Quantification of BL intensity after hind limbs are extracted. Representative *ex vivo* BL imaging results are shown below the dot plot quantification. Error bars: S.D. The experiment was replicated twice and showed consistent results. Data shown is the combined results. The P value was determined by *t*-test (2-tailed). **(B)** Quantification (left) and representative BL images (middle) of in vivo bone colonization kinetics of IIA-injected MCF7 cells expressing empty vectors or CA-CaMKII treated with vehicles or As2O3 (n=6 for each group) and quantitation and representative BL images (right) of BL intensity (normalized, log2-transformed) of extracted bones. p value by repeated measures ANOVA (left) or LSD test (right). Error bars = S.E.M.

Subtask 3: Optimize and modify the compounds to achieve higher efficiency. We will use the same models as subtask 1. (Month 36-48)

To begin by Month 36.

Subtask 4: In-depth mechanistic studies of the validated compounds. We will perform RNAseq on BMM in vivo to delineate pathways affected by the compounds. We will then identify key genes that may mediate the compounds' effects. Genetic depletion will then be performed to perturb these genes. The models are the same as subtask 1. (Month 36-60)

To begin by Month 36.

4. Impact

The proposed research is innovative and distinctive in the field of breast cancer research for the following reasons. First, to date few experimental models can be used to test the therapeutic responses of BMM. The vast majority of pre-clinical research has been done using orthotopic tumor models, despite the fact that micrometastases are the major targets of adjuvant therapies. We have established unique in vivo and ex vivo models to fill this gap. We will use these models to elucidate how different subtypes of breast cancer respond to their respective adjuvant therapies as microscopic lesions embedded in the bone, a significant step toward full recapitulation of clinical scenarios. Second, BICA combines the complexity of bone microenvironment and the scalability of in vitro culturing. Compared to previous "tissue-in-culture" approaches, bone-in-culture represents a better mimicry of the counterpart organ because BMM are tightly integrated into the osteogenic niche and are difficult to be dissociated from the bone tissue. As a result, the cancer-niche crosstalk is preserved after tissue fragmentation. Thus, BICA provides distinctive opportunities to rapidly assay hundreds of compounds and reveal novel treatments of BMM. Third, the proposed research assembles a number of experts with different expertise including the-state-of-art breast cancer PDX models (Lewis), single/few cell RNA-seq (Zong), and drug design and synthesis (Song). This is expected to generate significant synergy.

The research outcomes from the first three grant years include the discovery of novel mechanisms underlying cancer-bone interactions and identification of potential novel therapies that may help eliminate bone micrometastases and prevent overt recurrences.

5. Changes/Problems

So far, we have been making rapid progress and made multiple discoveries. Based on these discoveries, we have slightly adjusted our future plan. Instead of doing more exploratory studies (e.g., drug screening), we would like to deepen our studies on intriguing pathways and corresponding inhibitors that were already discovered. Specifically, we will focus on how the bone microenvironment induces downregulation of ER in ER+ cancer cells and confers endocrine resistance. We will also investigate how gap junctions, calcium signaling and the ER pathways interact with one another. We will proactively seek opportunities and additional funding to translate our current findings.

6. Products

Wang H, Lin T, Liu J, Goldstein A, Zhang W, Bado I, Li Z, Zhao H, Wong ST, **Xiang H.-F. Zhang**. (2018) *"The osteogenic niche is a calcium reservoir of breast cancer bone micrometastases and confers unexpected therapeutic vulnerability"* Cancer Cell, 34(5):823:839. PMCID: PMC6239211.

7. Participants & Other Collaborating Organizations

Name:	Chenghang Zong
Project Role:	Co-investigator
Researcher Identifier:	N/A
Nearest person month worked	0.36
Contribution	Dr. Zong is an expert of single-cell sequencing, and is helping us establish protocols to sequence BMM transcriptomes, which is

	critical to delineate molecular mechanisms underlying endocrine resistance of BMM.
Funding Support	Dr. Zong was also supported by NIH New Innovator1DP2EB020399-01
Name:	Yongcheng Song
Project Role:	Co-investigator
Researcher Identifier:	N/A
Nearest person month worked	0.6
Contribution	Dr. Song is an expert of chemical synthesis and modification of drugs. He is helping us to improve bioavailability and pharmacokinetics of potential bone metastasis drugs.
Funding Support	Dr. Song was also supported by NIH R01NS080963, Cancer Prevention and Research Institute of Texas RP140469 and RP150129
Name:	Michael Lewis
Project Role:	Co-investigator
Researcher Identifier:	N/A
Nearest person month worked	0.6
Contribution	Dr. Lewis established a cohort of PDX models. He is helping us utilize PDX models to generate metastasis models for mechanistic and therapeutic studies.
Funding Support	Dr. Lewis is also supported by fundings from NSF (1263742), NIH (CA179720) and Helis Foundation.
Name:	Hai Wang
Project Role:	Research Associate
Researcher Identifier:	N/A
Nearest person month worked	12
Contribution	Dr. Wang specialize in bone metastasis research techniques and is leading the efforts of establishing BICA.
Name:	Yang Gao
Project Role:	Postdoctoral Fellow
Researcher Identifier:	N/A

Nearest person month worked	6
Contribution	Dr. Yang focuses on the role of estrogen receptors in driving bone microenvironment-dependent endocrine resistance.
Name:	Zhan Xu
Project Role:	Postdoctoral Fellow
Researcher Identifier:	N/A
Nearest person month worked	12
Contribution	Dr. Xu focuses on the roles of various bone microenvironment niches during bone metastasis colonization.
Name:	Emmale Davis
Project Role:	Research Technician
Research Identifier:	N/A
Nearest person month worked	4
Contribution	Assistance to animal experiments.

Name:	Xiang Zhang
Project Role:	PI/PD
Researcher Identifier:	N/A
Nearest person month worked	3.0
Contribution	Dr. Zhang designed and supervised the experiments described in this report.
Funding Support	Dr. Zhang is also supported by NIH/NCI, Breast Cancer Research Foundation, and McNair Medical Institute.

All collaborators and participants are at Baylor College of Medicine.

8. Special Reporting Requirements
None.

9. Appendices
A copy of the publications.

Article

Cancer Cell

The Osteogenic Niche Is a Calcium Reservoir of Bone Micrometastases and Confers Unexpected Therapeutic Vulnerability

Graphical Abstract

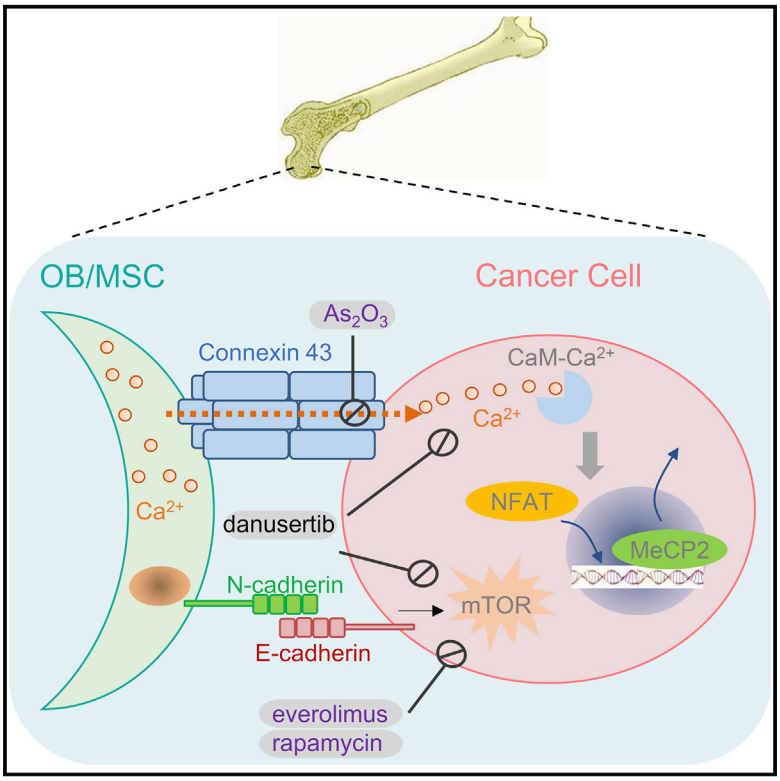

Highlights

- Calcium signaling is enhanced in bone metastasis compared with other metastases
- Cancer cells rely on direct calcium influx from osteogenic cells to increase [Ca^{2+}]
- Gap junctions mediate Ca^{2+} flow from osteogenic cells to cancer cells
- As_2O_3 suppresses latent bone metastasis by inhibiting calcium signaling

Authors

Hai Wang, Lin Tian, Jun Liu, ..., Stephen T.C. Wong, Zbigniew Gugala, Xiang H.-F. Zhang

Correspondence

xiangz@bcm.edu

In Brief

Wang et al. report that cancer cells obtain calcium from the osteogenic niche through gap junctions and that Ca signaling together with mTOR signaling promotes bone metastasis progression. They identify that As_2O_3 and danusertib affect Ca signaling and preferentially target cancer cells in the bone microenvironment.

Wang et al., 2018, Cancer Cell *34*, 823–839
November 12, 2018
https://doi.org/10.1016/j.ccell.2018.10.002

CellPress

Cancer Cell
Article

The Osteogenic Niche Is a Calcium Reservoir of Bone Micrometastases and Confers Unexpected Therapeutic Vulnerability

Hai Wang,[1,2,3] Lin Tian,[1,2] Jun Liu,[1,2,3] Amit Goldstein,[1,2,3] Igor Bado,[1,2,3] Weijie Zhang,[1,2,3] Benjamin R. Arenkiel,[4,5] Zonghai Li,[6] Meng Yang,[7] Shiyu Du,[8] Hong Zhao,[9] David R. Rowley,[2,3] Stephen T.C. Wong,[2,3,9] Zbigniew Gugala,[10] and Xiang H.-F. Zhang[1,2,3,5,11,*]

[1]Lester and Sue Smith Breast Center, Baylor College of Medicine, One Baylor Plaza, Houston, TX 77030, USA
[2]Dan L. Duncan Cancer Center, Baylor College of Medicine, One Baylor Plaza, Houston, TX 77030, USA
[3]Department of Molecular and Cellular Biology, Baylor College of Medicine, One Baylor Plaza, Houston, TX 77030, USA
[4]Department of Human and Molecular Genetics, Baylor College of Medicine, One Baylor Plaza, Houston, TX 77030, USA
[5]McNair Medical Institute, Baylor College of Medicine, BCM600, One Baylor Plaza, Houston, TX 77030, USA
[6]State Key Laboratory of Oncogenes and Related Genes, Shanghai Cancer Institute, Renji Hospital, Shanghai Jiao Tong University School of Medicine, Shanghai 200032, P.R. China
[7]Department of General Surgery, China-Japan Friendship Hospital, Beijing 100029, China
[8]Department of Gastroenterology, China-Japan Friendship Hospital, Beijing 100029, China
[9]Department of Systems Medicine and Bioengineering, Houston Methodist Research Institute, 6670 Bertner Avenue, Houston, TX 77030, USA
[10]Department of Orthopaedic Surgery & Rehabilitation, University of Texas Medical Branch, Galveston, TX 77555, USA
[11]Lead Contact
*Correspondence: xiangz@bcm.edu
https://doi.org/10.1016/j.ccell.2018.10.002

SUMMARY

The fate of disseminated tumor cells is largely determined by microenvironment (ME) niche. The osteogenic niche promotes cancer cell proliferation and bone metastasis progression. We investigated the underlying mechanisms using pre-clinical models and analyses of clinical data. We discovered that the osteogenic niche serves as a calcium (Ca) reservoir for cancer cells through gap junctions. Cancer cells cannot efficiently absorb Ca from ME, but depend on osteogenic cells to increase intracellular Ca concentration. The Ca signaling, together with previously identified mammalian target of rapamycin signaling, promotes bone metastasis progression. Interestingly, effective inhibition of these pathways can be achieved by danusertib, or a combination of everolimus and arsenic trioxide, which provide possibilities of eliminating bone micrometastases using clinically established drugs.

INTRODUCTION

In breast cancer (BCa), spread of tumor cells may occur before diagnosis (Huang et al., 2013). The resultant metastatic seeds in distant organs are left behind by surgeries, survive adjuvant therapies, enter and then exit a presumable dormancy/latency state, and eventually resume aggressive outgrowth (Massagué and Obenauf, 2016). Bone is the most frequently affected organ by BCa metastasis (Kennecke et al., 2010; Smid et al., 2008), and often the first site of metastasis, especially after long latency (Zhang et al., 2013a).

In the clinic, bone metastases are usually diagnosed with significant skeletal-related events (Ell and Kang, 2012; Weilbaecher et al., 2011). At this stage, metastases are driven by a vicious

Significance

Breast cancer bone metastasis often occurs asynchronously, years after primary tumor resection and adjuvant therapies, suggesting mechanisms driving therapeutic resistance and tumor re-growth specifically in the bone ME. We discovered that Ca influx from the osteogenic niche to cancer cells is essential for proliferation of early-stage bone metastasis, in addition to the previously identified role of mTOR signaling. We performed target-driven search for therapeutic agents inhibiting both pathways and identified danusertib and arsenic trioxide as potent candidates. Danusertib is currently under clinical development. Arsenic trioxide is an FDA-approved drug for leukemia. The preferential efficacies of these drugs on BMM argue for immediate applications to eliminate latent cancer cells in the bone marrow and reduce metastasis recurrences.

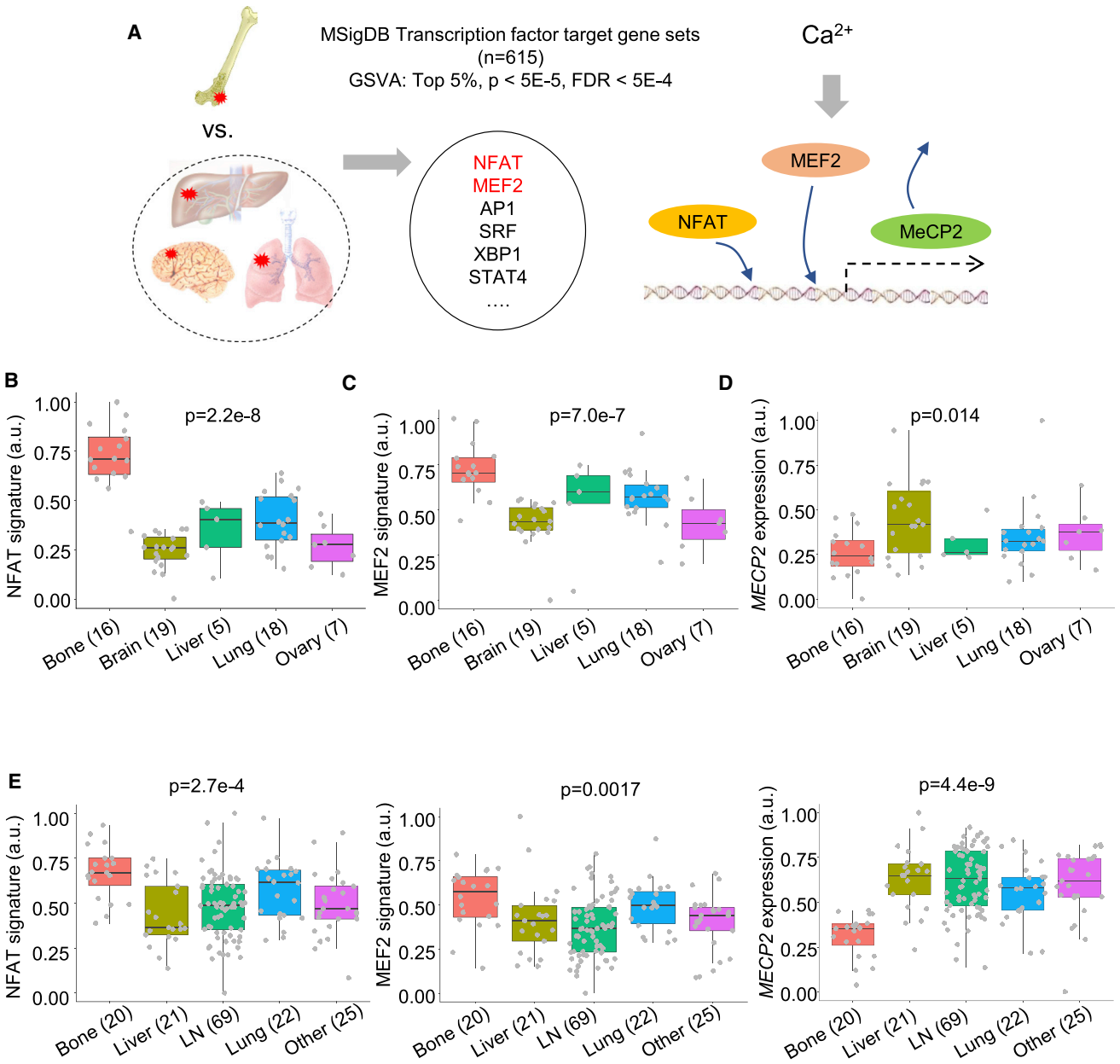

Figure 1. Ca Signaling Is Enriched in Bone Metastasis Compared with Metastases in Other Organs

(A) An overview of bioinformatics analysis leading to Ca signaling. GSVA, gene set variation analysis; FDR, false discovery rate. Both p values and FDR were computed by the statistics of microarray (SAM) algorithm. MSigDB C3 transcription factor targets (TFT) database was analyzed.

(B–D) Boxplots show the expression of an NFAT signature (B), an MEF2 signature (C), and *MECP2* (D) across human BCa metastases in different organs (GEO: GSE14020).

(E) Similar to (B–D), except that human PCa metastases (GEO: GSE77930) is examined.

(B–E) p values by one-way ANOVA.

For all boxplots: line inside the box, median value; top/bottom of the box, 75th/25th percentile; upper/lower whiskers, largest/smallest values no further than 1.5× inter-quartile range from the hinge; data points beyond whiskers, possible outliers. Same for the boxplots in other figures. See also Figure S1.

cycle between cancer cells and osteoclasts (Boyce et al., 1999; Kang et al., 2003). Targeting osteoclasts by bisphosphonates and denosumab, can limit metastasis progression but cannot extend overall survival (Mackiewicz-Wysocka et al., 2012). Several molecular pathways have been implicated in the vicious cycle, including Notch (Sethi et al., 2011), transforming growth factor β (Fournier et al., 2015; Waning et al., 2015), integrin (Ross et al., 2017), and interleukin-6 (Luo et al., 2016). These discoveries have significantly enriched the options of treating overt bone metastases.

Relatively less is known about early-stage bone colonization before the vicious cycle occurs. Disseminated tumor cells

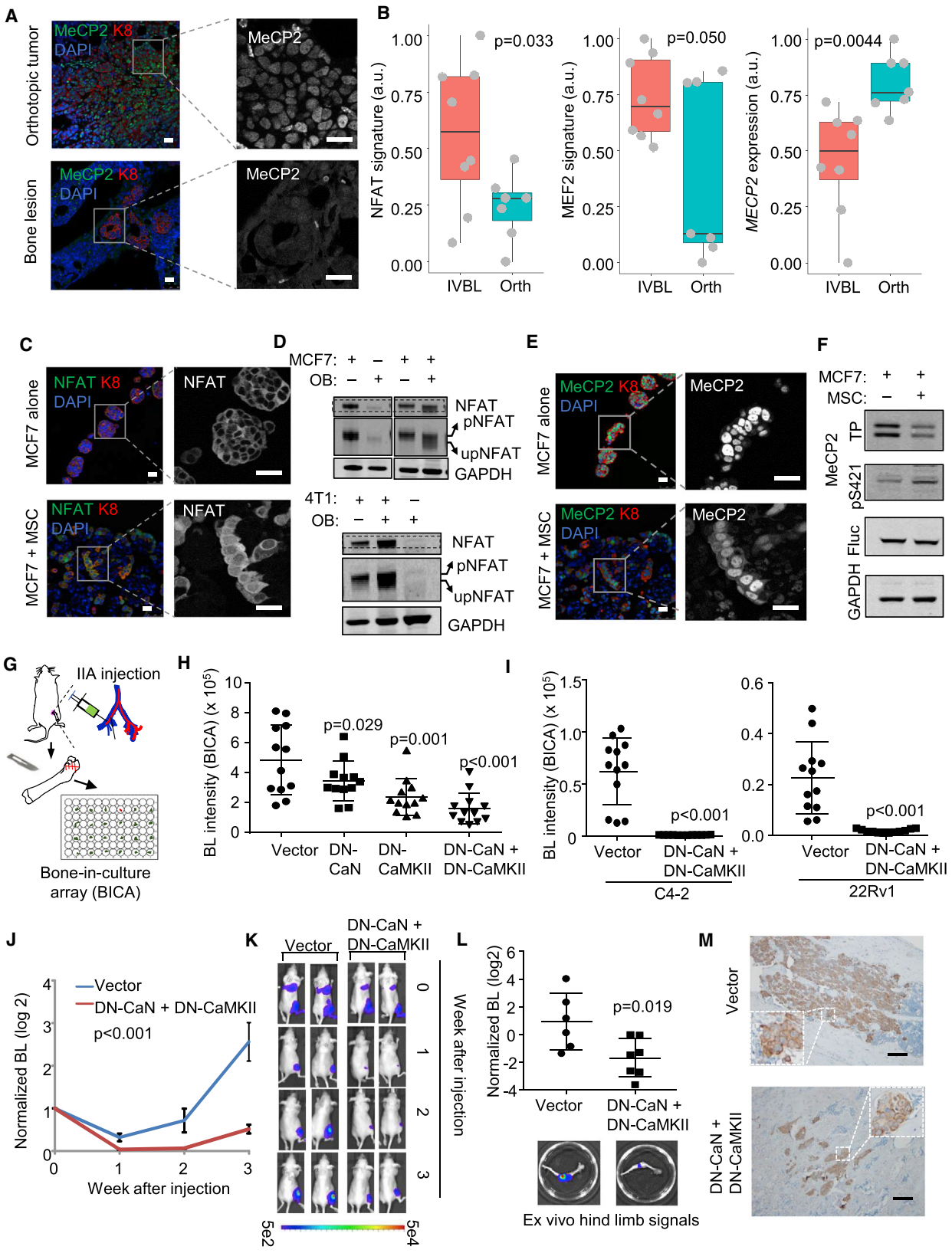

(legend on next page)

(DTCs) in the bone marrow are associated with poor survival of patients, suggesting that they are precursors of late, overt metastases (Wan et al., 2013). Specific microenvironment (ME) niches have been implicated to determine DTC fate. In particular, the peri-vascular niche regulates dormancy of DTCs (Ghajar et al., 2013; Price et al., 2016), whereas the osteogenic niche promotes bone micrometastases (BMM) proliferation and progression (Wang et al., 2015) and resistance to chemotherapies (Zheng et al., 2017). However, molecular mechanisms behind cancer-niche crosstalk are largely elusive, and need to be elucidated for eradication of DTCs and BMM.

Our previous studies demonstrate that cancer cells and osteogenic cells (osteoblasts [OBs] and their precursors) can form heterotypic adherens junctions (hAJs), which in turn activate the mammalian target of rapamycin (mTOR) signaling to promote BMM progression (Wang et al., 2015). mTOR inhibitors were approved by the US Food and Drug Administration (FDA) to treat endocrine-resistant estrogen receptor alpha-positive (ER^+) tumors (Baselga et al., 2012). The treatment significantly delayed tumor progression, but failed to extend overall survival. We hypothesize that there are additional pathways that may cooperate with the mTOR signaling to mediate osteogenic niche's metastasis-promoting effects.

RESULTS

Transcription Factor Activities Downstream of Calcium Signaling Are Enriched in Bone Metastases

To understand how the bone ME may affect signaling pathways in cancer cells, we conducted an unbiased comparison to identify transcription factors (TFs) with differential activities between bone and other metastases of BCa in a published dataset (GEO: GSE14020) (Zhang et al., 2013b). We utilized gene set variation analysis (Hänzelmann et al., 2013) and focused on TF target gene sets defined by binding motifs in promoter regions (Subramanian et al., 2005). We identified the top 5% of TFs whose activities are enriched in bone metastases. These include NFAT and MEF2, which are both downstream of calcium (Ca) signaling (Figures 1A and S1A) (Berridge et al., 2003; Macian, 2005; McKinsey et al., 2002). This finding was validated by a different approach and independent NFAT and MEF2 signatures (Di Giorgio et al., 2017; Tripathi et al., 2014) (Figures 1B and 1C). Moreover, activation of Ca signaling is associated with epigenomic reprogramming (Raynal et al., 2016). We asked if any epigenetic modulator is differentially expressed in bone metastases. MeCP2 is a nuclear protein that binds methylated DNA and recruits other factors such as histone deacetylases, acting as a transcriptional repressor (Shahbazian et al., 2002). Ca signaling triggers the CaMKII-dependent MeCP2 phosphorylation (S421), and releases MeCP2 from silenced promotors in various cellular contexts (Buchthal et al., 2012; Li et al., 2014). Consistently, the alteration of *MECP2* expression displayed a trend opposite to that of NFAT and MEF2—it is expressed at a lower level in bone metastasis than in other sites (Figure 1D). Due to the availability of high-quality antibodies, the expression level and localization of MeCP2 may serve as an indicator of Ca signaling *in vivo*.

In another dataset of BCa metastases (GEO: GSE46141), similar differences in NFAT, MEF2, and *MECP2* expression were observed between bone and visceral metastases, although statistical significance was not achieved due to smaller sample size (Figure S1B). Moreover, in a cohort of 615 primary BCa (Zhang et al., 2009), the NFAT signature appeared to be associated with bone metastasis-free survival, but not with lung or brain metastasis-free survival (Figure S1C).

Prostate cancer (PCa) is another cancer type that frequently metastasizes to bone. In a dataset of PCa metastases in different organs (GEO: GSE77930) (Kumar et al., 2016), we observed a significant increase of expression of NFAT and MEF2 signatures, and a dramatic decrease of *MECP2* expression (Figure 1E) in bone metastases compared with other sites.

Figure 2. Experimental Models Recapitulate the Enhancement of Ca Signaling in Cancer Cells Interacting with the Bone ME

(A) Representative immunofluorescence (IF) staining of MeCP2 in orthotopic tumors and bone lesions. Keratin 8 (K8) marks cancer cell cytoplasm; DAPI marks nucleus; trans-localization is highlighted by single-channel images; Scale bars, 25 μm.

(B) Boxplots show the expression of the NFAT signature, the MEF2 signature, and *MECP2* in *in vivo* bone lesions (IVBL) (n = 8) or orthotopic tumors (Orth) (n = 7) derived from MCF7 cells.

(C) IF staining of NFAT is shown in mammospheres of MCF7 cells alone or heterotypic organoids of admixed MSCs and MCF7 cells to mimic bone ME. Scale bars, 25 μm.

(D) Western blot of indicated (phospho-)proteins in 3D cultures of cancer cells or OBs either alone or admixed. The slight shift between phosphor-NFAT (pNFAT) or non-phosphor-NFAT (npNFAT) is highlighted by altering the display width/length ratio of the gel shown as an additional row.

(E) Similar to (C) except that MeCP2 staining is shown.

(F) Western blot shows total (TP) or S421-phosphorylated MeCP2 in MCF7 cells with or without MSCs in 3D co-cultures. Firefly luciferase (Fluc) was used as loading control for cancer cells.

Samples of (C–F) were harvested after mono- or co-culture for 48 hr.

(G) A schematic illustration of BICA platform.

(H) Bioluminescence intensity (BL) in BICA of MCF7 cells expressing empty vector, dominant-negative CaN (DN-CaN), dominant-negative CaMKII (DN-CaMKII), and both (DN-CaN + DN-CaMKII). n = 12 bone fragment for each group.

(I) Similar to (H) except that prostate cancer cell lines C4-2 and 22Rv1 were used.

(J) Bone colonization curves of IIA-injected MCF7 cells, either expressing empty vector or DN-CaN + DN-CaMKII. n = 6 and 7 for the two groups, respectively.

(K) Represented BL pictures of mice in the vector and DN-CaN + DN-CaMKII (DN) groups.

(L) Quantitation of *ex vivo* BL signals emitted from extracted hindlimb bones. Representative pictures are shown.

(M) Representative immunohistochemistry (IHC) staining of bone lesions derived from (J). Tumor lesions were indicated by K8 (brown) staining. Scale bars, 100 μm.

p values by one-way ANOVA (B), least significant difference (LSD) (H), Student's t tests (I and L), or repeated measures ANOVA test (J). Error bars = SD (H, I, and L) or SEM (J). See also Figure S2.

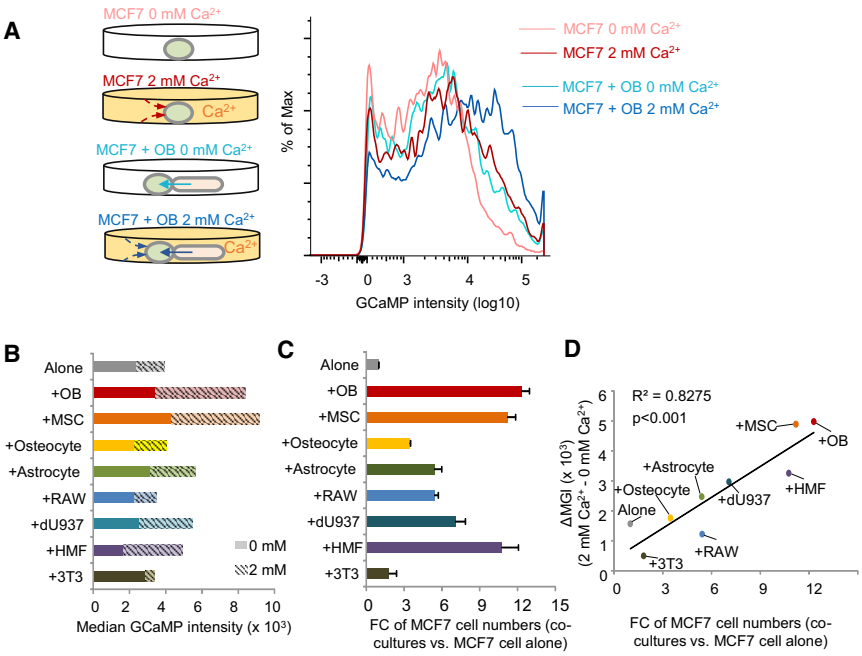

Figure 3. Ca^{2+} Flows from Osteogenic Cells to Cancer Cells

(A) A schema of MCF7-OB co-culture assay with GCaMP indicating alteration of [Ca^{2+}] in cancer cells (left) and representative intensity curves of GCaMP under the indicated four conditions (right).

(B) GCaMP intensity in MCF7 cells (alone or co-cultured with indicated cell types) as a function of different cell types in co-cultures and medium [Ca^{2+}]. Bars show GCaMP intensity in MCF7 cells in medium with [Ca^{2+}] = 0 mM (solid) or [Ca^{2+}] = 2 mM (hashed). MSC, mesenchymal stem cells.

(C) Fold change (FC) of MCF7 cell quantity in 3D co-cultures with indicated cell types as compared with MCF7 alone. MCF7 cells were quantitated by BL. Error bars = SD (n = 3 technical replicates).

(D) A scatterplot shows the correlation between increase of [Ca^{2+}] as indicated by changes of median GCaMP intensity (MGI) and the FC of MCF7 cells in co-cultures.

In (B)–(D): RAW, RAW264.7 cells, osteoclast precursors; dU937, differentiated U937 cells, osteoclasts; HMF, human mammary fibroblast cells; 3T3, NIH3T3cells, mouse embryo fibroblasts.

Pearson correlation coefficient and p values (by Student's t test) are shown. See also Figure S3.

In Vivo and *Ex Vivo* Bone Metastasis Models Recapitulate Ca Signaling Alterations in Cancer Cells

We previously established *in vivo* models based on intra-iliac artery (IIA) injection and *in vitro* 3D co-culture of cancer cells and osteogenic cells (including OBs and mesenchymal stem cells [MSCs]). These models allow us to investigate how BCa cells interact with bone cells and initiate the colonization (Wang et al., 2015; Yu et al., 2016).

In our *in vivo* model, bone lesions introduced by IIA injection of MCF7 cells exhibited diminished immunofluorescence (IF) MeCP2 staining as compared with orthotopic tumors established by the same cells using mammary fat pad injection (Figure 2A). Transcriptomic profiling (GEO: GSE110451, Figure S2A) indicated upregulation of NFAT and MEF2 transcription activities and downregulation of *MECP2* expression at RNA level in the bone lesions compared with orthotopic tumors (Figure 2B). Thus, IIA-based bone metastasis models recapitulate the observations in clinical datasets.

In vitro 3D co-culture of cancer cells and osteogenic cells is a further simplified model that focuses on osteogenic cells only. Cancer cells and osteogenic cells form heterotypic organoids after 48 hr, causing an increase of cancer cell proliferation and survival as we showed previously (Wang et al., 2015). The interaction with osteogenic cells led to an increase of NFAT IF signal intensity in the nucleus, indicating nuclear trans-localization of NFAT (Figure 2C, of note, NFAT antibodies did not work well on decalcified tissues, preventing application to *in vivo* bone tissues). NFAT subcellular localization is regulated by dephosphorylation (Sharma et al., 2011), and can be reflected by a slight but obvious gel-shift on western blot (Figure 2D). By IF, MeCP2 appeared to follow an opposite trend upon the interaction with osteogenic cells—its signal intensity increases in cytoplasm but decreases in the nucleus. The overall intensity also appeared to decrease (Figure 2E). This indicates trans-localization from the nucleus to the cytoplasm, as well as an overall reduction at the protein level. Western blot again confirmed this change, and, in addition, revealed an increase of phosphorylation of MeCP2 at S421 (Figure 2F), a regulatory modification leading to nuclear exportation (Buchthal et al., 2012). Because the osteogenic cell lines express little NFAT or MeCP2 (Figures 2D, 2E, and S2B), the alterations seen in western blots were likely to occur in cancer cells. To further validate this point, we used murine osteogenic cells so that gene expression in human cells can be assessed by qPCR with human-specific primers. Both the eight-gene NFAT signature (Tripathi et al., 2014) as well as *MECP2* exhibited expected changes (Figure S2C). Thus, the major ME factor that drives the alteration of Ca signaling in cancer cells appears to be the direct interaction with osteogenic cells.

Inhibition of Ca Signaling Impedes Bone Colonization

Ca signaling involves transducers such as CaMKII and calcineurin (CaN), and TFs such as NFAT and MEF2, all of which are encoded by multiple genes, making genetic depletion difficult. Instead, we tested pharmacological inhibitors of CaN (FK506) and CaMKII (Kn93). Both reduced MeCP2 phosphorylation and NFAT de-phosphorylation (Figure S2D), and abolished the tumor-promoting effects of osteogenic cells in 3D co-cultures (Figure S2E).

We also employed the bone-in-culture array (BICA) to examine the role of Ca signaling in bone colonization. Specifically, bone tissues harboring IIA-introduced cancer cells are fragmented to generate a number of *ex vivo* bone segments (Figure 2G). We showed previously that cancer-bone interaction is maintained in BICA for up to 4–6 weeks, and allows multiplex treatments (Wang et al., 2017). As another way to overcome paralog redundancy, we employed dominant-negative (DN) CaN (ΔH160Q) (Shibasaki et al., 1996) and CAMKII (T286A) (Pi et al., 2010). DN-CaN and DN-CAMKII, alone or in combination, showed a moderate

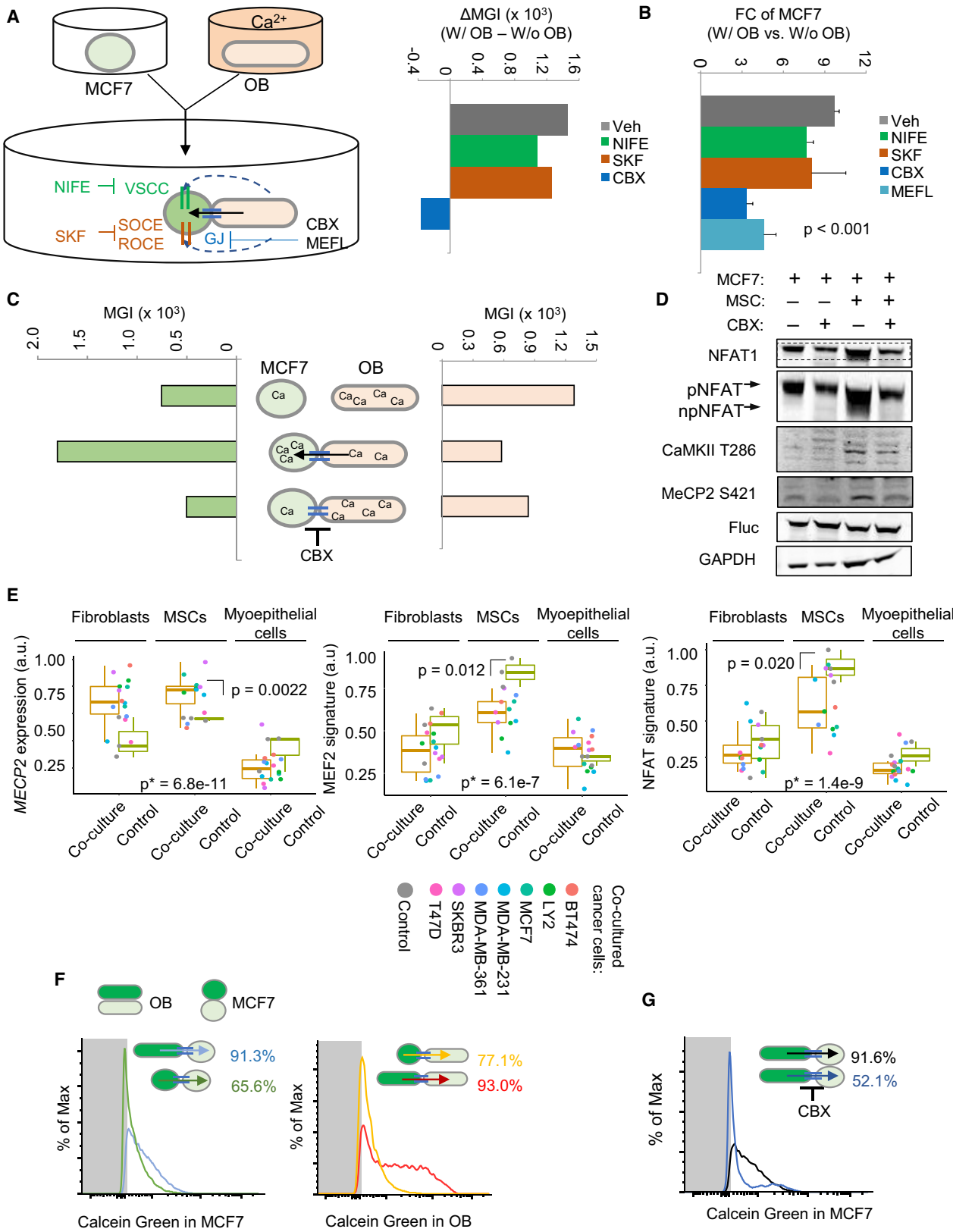

(legend on next page)

effect on tumor proliferation *in vitro* (Figure S2F) but dramatic decrease of growth of BCa and PCa in BICA (Figures 2H and 2I).

Finally, IIA-injected MCF7 cells expressing both DN-CaN and DN-CAMKII, compared with control cells, exhibited remarkably reduced bone colonization (Figures 2J–2M). The same trend was observed on PCa cells: IIA injection of C4-2 cells generated detectable bone lesions in four of seven mice in 6 weeks, whereas no lesions was detected when DN-CaN and DN-CAMKII were expressed (Figure S2G).

Osteogenic Cells Boost Ca Concentration in Cancer Cells

We examined alterations of steady-state intracellular Ca concentration ([Ca^{2+}]) of cancer cells. Classic approaches such as patch-clamp or microfluorometry (e.g., Fura2) (Ishikawa et al., 2011) were not applicable, as they could not distinguish different cell types in the co-culture system. As an alternative, we transduced MCF7 cells with GCaMP, a genetically encoded [Ca^{2+}] indicator (Chen et al., 2013). MCF7 cells appeared to have limited ability to absorb Ca directly from medium, as GCaMP intensity only increased moderately when 2 mM Ca^{2+} was added to medium (Figure 3A). In the Ca^{2+}-free medium, when human fetal OBs were added, cancer cell [Ca^{2+}] increased to a degree comparable with 2 mM Ca^{2+} medium (Figure 3A). A dramatic increase was observed when both OBs and 2 mM Ca^{2+} were combined (Figure 3A). This observation suggested that, compared with cancer cells, OBs are more efficient in absorbing Ca from environment and may in turn provide Ca to cancer cells.

To ask if this property is unique to OBs, we tested other cell types including MSCs, fibroblasts, osteoclasts, and astrocytes (Figures 3B and S3). These cells conferred variable degrees of growth advantages, but only MSCs appear to have a similar, Ca^{2+}-related effect, highlighting that the ''Ca provider'' function may be specific to osteogenic cells (OBs and MSCs) (Figure 3C). Overall, the fold changes of growth are correlative with the ability of these cells to boost [Ca^{2+}] in cancer cells (Figure 3D), indicating that the ability of increase [Ca^{2+}] in cancer cells is one mechanism among others to enhance tumor progression.

Ca^{2+} Flows from Osteogenic Cells to Cancer Cells via Gap Junctions

Osteogenic cells may increase cancer cell [Ca^{2+}] by a few possible mechanisms. They may release Ca^{2+} to medium, which in turn enters cancer cells through various Ca channels or receptors (Berridge et al., 2003; Dubois et al., 2014). Alternatively, Ca^{2+} may directly flow between cells via gap junctions (GJs) (Osswald et al., 2015). We employed inhibitors targeting these mechanisms and asked whether they could reverse the observed [Ca^{2+}] change. Inhibitors of voltage-sensitive Ca channel, store-operated Ca entry, and receptor-operated Ca entry, nifedipine (NIFE) or SKF96365 (Wu et al., 2015), could not stop [Ca^{2+}] increase in cancer cells (Figure 4A). In contrast, a GJ inhibitor, carbenoxolone (CBX), almost completely blocked the Ca^{2+} flow (Figure 4A). Consistently, CBX and another GJ inhibitor, mefloquine (MEFL), but not NIFE or SKF96365, suppress OB-induced growth of cancer cells in co-cultures (Figure 4B). ORAI proteins play important roles in prostate tumorigenesis by mediating store-independent Ca^{2+} entry (Dubois et al., 2014). *ORAI1* and *ORAI3* expression do not correlate significantly with BCa bone metastasis (Figures S4A and S4B), suggesting that ORAI channels might not play roles in later metastasis after initial tumorigenesis.

Direct flow of Ca^{2+} toward cancer cells may lead to depletion of Ca^{2+} in osteogenic cells. By expressing GCaMP in OBs, we observed a decrease of [Ca^{2+}] in these cells upon the establishment of cancer-bone interaction. This change in OBs, as well as the activation of Ca signaling in cancer cells, was abolished by CBX (Figures 4C and 4D). The reciprocal decrease of [Ca^{2+}] in osteogenic cells is also reflected by transcription. Analysis of patient-derived MSCs, fibroblasts, and myoepithelial cells revealed decreases of NFAT and MEF2 signatures and an increase of *MECP2* in MSCs when co-cultured with several cancer cell lines (GEO: GSE29036) (Figure 4E). These differences are less pronounced in fibroblasts and insignificant in myoepithelial cells (Figure 4E). Thus, the Ca^{2+} flow is specific between cancer cells and osteogenic cells, leading to increased Ca signaling in cancer cells but decreased Ca signaling in osteogenic cells (Figure S4C).

The GJs Mediate Bidirectional Substance Transfer

To assess the general directionality of the GJs between cancer cells and osteogenic cells, we incubated either cell type with calcein, a fluorescence dye that can diffuse through GJs, before setting up the 3D co-cultures. This experiment uncovered different efficiencies of heterotypic and homotypic GJs, with most efficient dye-transfer between osteogenic cells

Figure 4. GJs Mediate the Ca^{2+} Flow from Osteogenic Cells to Cancer Cells

(A) A schema of experiment design and key reagents and molecules (left) and the alteration of median GCaMP intensity by co-cultured OBs as a function of treatment of various inhibitors (right). The co-culture was performed in Ca^{2+}-free medium. VSCC, voltage-sensitive Ca channel; SOCE, store-operated Ca entry; ROCE, receptor-operated Ca entry; CBX, carbenoxolone; MEFL, mefloquine; NIFE, nifedipine; SKF, SKF96365; Veh, vehicle control; MGI, median GCaMP intensity.

(B) Fold change (FC) of MCF7 quantity, quantitated by BL, in the same experiment as (A). Error bars = SD (n = 3 per group). p values by one-way ANOVA.

(C) Changes of GCaMP intensity in MCF7 cells (left) and OBs (right) in monocultures, co-cultures, and co-cultures with 10 μM CBX. Data are based on two separate experiments: $GCaMP^+$ MCF7 + $GCaMP^-$ OB, and $GCaMP^+$ OB + $GCaMP^-$ MCF7.

(D) Western blot of indicated (phosphor-)proteins in MCF7 cells with or without 10 μM CBX treatment after mono- or co-culture for 4 hr. The gel-shift of NFAT1 is highlighted in additional rows.

(E) Expression of NFAT target gene set, MEF2 target gene set, and *MECP2* in fibroblasts, MSCs, and myoepithelial cells when they are co-cultured with various cancer cell lines. GSVA scores were calculated for NFAT and MEF2 target gene sets and re-scaled linearly between 0 and 1. Analyses were based on GEO: GSE27120. p values by Student's t tests between indicated groups; *p values by one-way ANOVA across all groups.

(F and G) Calcein transfer through GJs in co-culture of MCF7 cells and OBs in the absence (F) and presence (G) of 10 μM CBX. Negative control (no calcein) was indicated by gray area. The direction of transfer and percent positive recipient cells are indicated.

See also Figure S4.

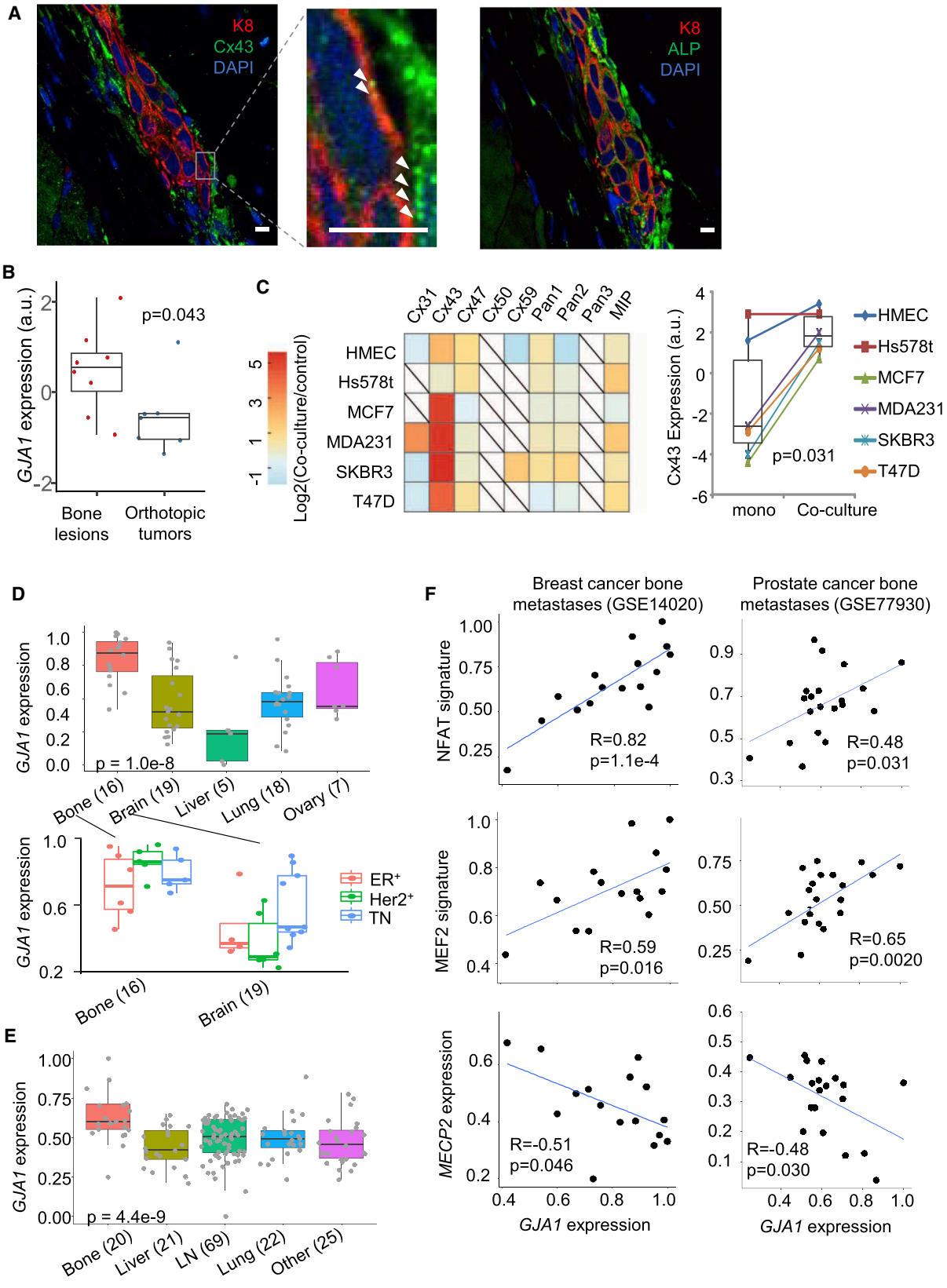

(legend on next page)

(Figures 4F and S4D). OBs and osteocytes are known to connect with one another with GJs to form a cellular network, which is an essential characteristic of bone tissue (Jiang et al., 2007). Calcein transfer was also detected between cancer cells, as well as between cancer cells and osteogenic cells in a bidirectional manner (Figures 4F and S4D). The transfer of calcein from osteogenic cells to cancer cells can be blocked by CBX (Figures 4G and S4E). These results suggest that the GJs between cancer cells and osteogenic cells are bidirectional. The apparently unidirectional flow of Ca^{2+} is likely driven by concentration gradient.

Connexin 43 Is Overexpressed in Bone Metastasis and Correlates with Ca Signaling in Clinical Samples

The connexin family proteins are the major constituents of GJs. Particularly in bone, osteocytes and OBs are widely connected by GJs composed of connexin 43 (Cx43) (Plotkin and Bellido, 2013). We asked if bone metastatic cells also express Cx43. IIA-injected MCF7 cells exhibited positive Cx43 staining at cancer-bone interface (Figure 5A). The expression level of Cx43 (encoded by *GJA1*) in cancer cells is significantly higher in bone lesions as compared with in orthotopic tumors (Figure 5B). Co-culture with MSCs induced expression of Cx43 in multiple cell lines (Figure 5C). Furthermore, the Ca transfer appears to be particularly significant between cancer cells and MSCs compared with fibroblasts and myoepithelial cells (Figure 4E). This trend is correlative to the expression of Cx43 in these stromal cells (Figure S5A).

In clinical data, bone metastasis exhibited the highest level of Cx43 expression among all sites of metastases of both BCa and PCa (Figures 5D and 5E). Cx43 expression in primary tumor is associated with bone metastasis-free survival (Figure S5B). Cx43 GJs play important roles in brain colonization in triple-negative (TN) BCa (Chen et al., 2016). By separating metastases based on ER, PR, and Her2 expression, we confirmed that all subtypes of bone metastases and TN brain metastases overexpress Cx43 (Figure 5D). Among bone metastases of BCa and PCa, Cx43 expression positively correlate with NFAT and MEF2 signatures, and negatively correlate with *MECP2* (Figure 5F). These correlations are weaker among metastases at other sites (Figure S5C), indicating that the connection between GJs and Ca signaling may be particularly strong in the bone ME.

Inhibition of GJs Suppresses Bone Colonization

In 3D co-culture, small interfering RNA-mediated knockdown of Cx43 in cancer cells or in OBs impeded the growth of MCF7 cells (Figure S6A). Overexpression of DN-Cx43 (G138R) (Roscoe et al., 2005), but not wild-type Cx43, could achieve similar effects (Figure S6B). The same observations were also made in murine BCa cells (Figure S6C).

In BICA, we found that ablation of Cx43 in either osteogenic cells or cancer cells, using cancer cells expressing DN-Cx43 or bone fragments derived from hosts with conditional knockout of *Gja1*, hindered bone colonization (Figures 6A–6C and S6D–S6F). Similar effects were observed when murine 4T1 cells were treated by CBX in BICA (Figure S6G). We previously reported that development of E-cadherin and N-cadherin hAJs promotes early bone colonization (Wang et al., 2015). Indeed, ablation of hAJs, either by knockout of *Cdh2*, encoding N-cadherin, in bone or knockdown of E-cadherin in cancer cells, causes reduced cancer growth in BICA (Figures S6E and S6F). It is well established that formation of adherens junctions precedes and facilitates GJ development (Jiang et al., 2007; Shaw et al., 2007). Our data support this notion and indicate that both AJs and GJs mediate cancer-niche interaction.

Several *in vivo* experiments were also conducted to tackle GJs in bone colonization. Firstly, compared with control cells, DN-Cx43-expressing MCF7 cells exhibited significantly delayed bone colonization after IIA injection, opposite to the wild-type Cx43 (Figures 6D–6F). Secondly, treatment of GJ inhibitors, MEFL or CBX, significantly delayed bone colonization of IIA-injected MCF7 cells (Figures 6G–6I and S6H). CBX treatment caused nuclear localization of MeCP2 in bone lesions (Figure S6I), suggesting reduced Ca signaling. Thirdly, 4T1.2 cells were orthotopically transplanted into syngeneic BALB/c mice, and orthotopic tumors were resected once reaching certain size. The following adjuvant CBX significantly reduced spontaneous bone metastasis, but had little effects on metastases in lungs (Figures 6J–6L). Taken together, these data strongly support the role of GJs in bone colonization.

Side Effects of GJ Inhibitors and High Effective Dosage of Ca Signaling Inhibitors Prompted Need for Alternative Therapeutic Strategies

Long-term CBX treatment led to an increased vertebral curvature and consequently a reduced length from head to tail (Figure S7A). This is not surprising given the important roles of GJs in normal bone development and homeostasis (Jiang et al., 2007). Thus, global GJs may not be an ideal target for chronic treatment. Ca^{2+} appeared to flow unidirectionally from osteogenic cells to cancer cells. The activation of Ca signaling is specific to cancer cells and may represent a more suitable target. Inhibitors, such as FK506 and Kn93, affected cancer

Figure 5. Connexin 43 Is the Major Constituent of GJs

(A) IF co-staining of K8 and connexin 43 (Cx43) (left) or K8 and ALP (OBs, right) in sequential sections of a microscopic bone lesion derived from IIA-injected MCF7 cells. Arrows in high magnification pictures indicate punctuated Cx43 staining. Scale bars, 10 μm.

(B) Normalized expression of *GJA1* in bone lesions versus orthotopic tumors (GEO: GSE110451). p values by Student's t test.

(C) A heatmap (left) showing the expression level difference of genes encoding connexin family proteins in five breast cancer cell lines and human mammary epithelial cells (HMEC) upon co-culture with OBs (GEO: GSE29036) and the paired Cx43 expression (right) between mono- and co-cultures of these cells. p values by paired t test.

(D) The expression of *GJA1* across BCa metastases in different organs (GEO: GSE14020, top) and in bone and brain metastases divided based on ER and human epidermal growth factor receptor 2 (Her2) statuses (bottom). Sample size of each group is shown in parentheses. p values by one-way ANOVA.

(E) Similar to (D) except that human PCa metastases (GEO: GSE77930) is examined.

(F) Scatterplots showing the correlations between *GJA1* expression and the NFAT signature, the MEF2 signature, and *MECP2* expression in bone metastases of BCa and PCa. All values were linearly re-scaled to between 0 and 1.

Pearson correlation coefficients and p values by Student's t tests are shown. See also Figure S5.

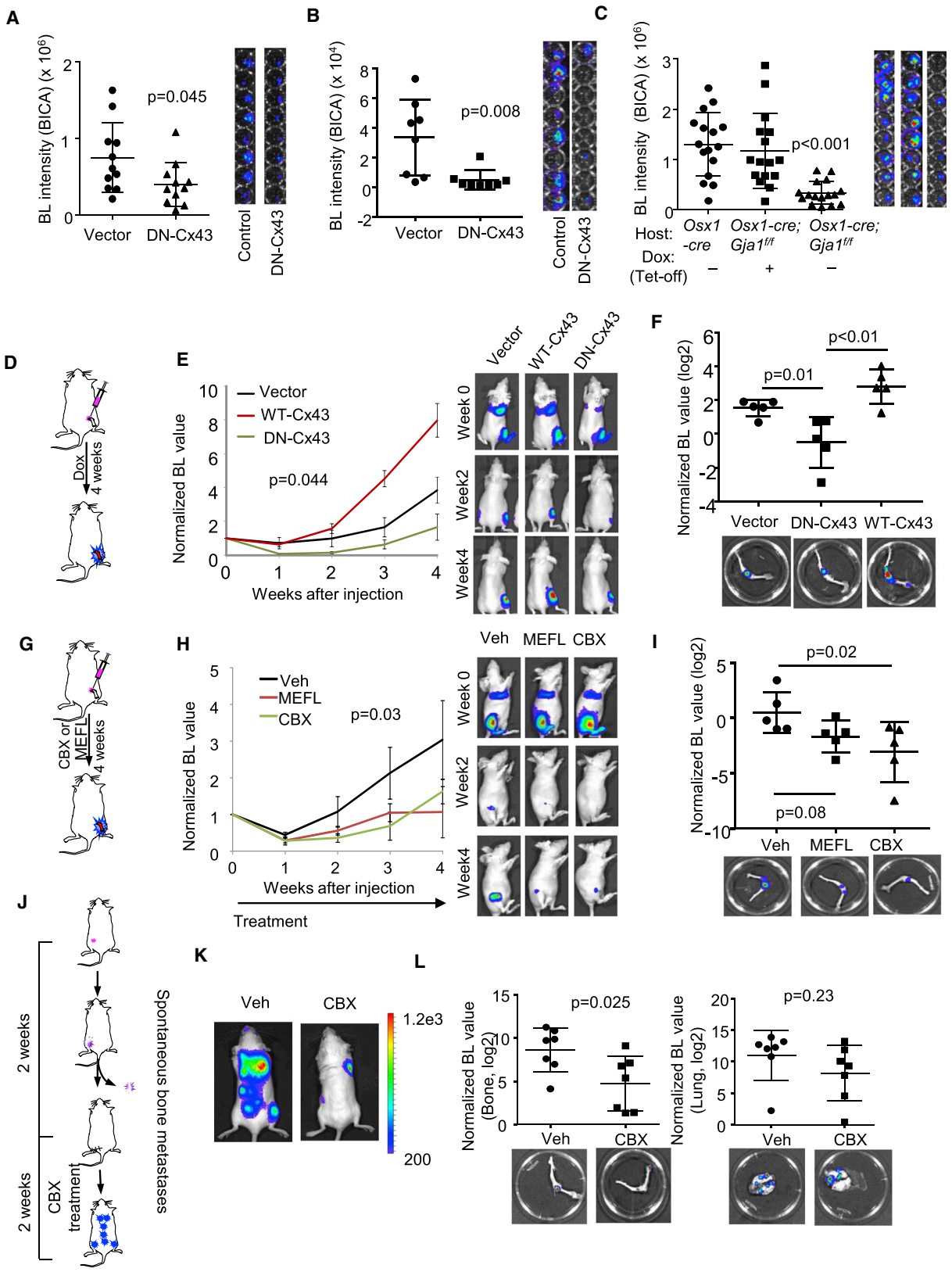

(legend on next page)

cell growth in the bone ME only at micromolar concentrations (Figure S7B), which renders it unrealistic to be applied *in vivo*. The mTOR signaling also contributes to promote bone colonization (Wang et al., 2015). We therefore conducted a mini-screening to identify agents that can inhibit bone colonization, preferentially through inhibition of Ca signaling and/or mTOR signaling at clinically relevant dosage.

BICA Screening Identified As_2O_3 and Danusertib that Preferentially Target Cancer Cells in the Bone ME

We previously performed a BICA screening on a library of 68 small-molecule epigenetic modulators (Wang et al., 2017). This screening led to identification of danusertib, a pan-aurora kinase inhibitor with bone metastasis-selective efficacies. Here, we performed another screening on a library containing 63 FDA- or foreign-approved anti-neoplasm drugs selected from John Hopkins University Clinical Compound Libraries (JH library, see Table S1), in order for potentially rapid drug repositioning. Two rounds of tests were conducted (Figure 7A), leading to the identification of arsenic trioxide (As_2O_3) (Figures S7C and S7D), which displayed a comparable efficacy with danusertib (Figure 7B). This effect appears to be bone-preferential: the half maximal inhibitory concentration (IC_{50}) of As_2O_3 is reduced by 10- and 1,000-fold in BICA compared with 2D culture of cancer cells alone for MCF7 and C4-2 cells (Figure 7C). We validated that, like danusertib, As_2O_3 treatment significantly decreased spontaneous bone metastasis in the syngeneic 4T1.2 model when applied after orthotopic tumor resection (Figure 7D). This did not appear to be a general anti-tumor effect, as the same dosage had no effects on orthotopic tumor growth (Figure S7E).

As_2O_3 and Danusertib Both Affect Ca Signaling and GJs, but Exhibit Less Side Effects

Since both mTOR and Ca signaling mediate early-stage bone colonization, we asked whether the effects of As_2O_3 and danusertib on bone metastasis are mediated by these pathways. Indeed, both drugs appeared to increase NFAT phosphorylation and/or decrease MeCP2 phosphorylation in co-cultures (Figure 7E), and led an increase of nuclear MeCP2 in bone lesions (Figure 7F). Danusertib also decreased S6K phosphorylation, indicating a reduction of mTOR signaling (Figure 7E). Finally, both As_2O_3 and danusertib reduced GCaMP intensity in cancer cells in co-cultures (Figure 7G), indicating a decrease of $[Ca^{2+}]$.

Despite their effects on GJs, As_2O_3 and danusertib did not exhibit obvious side effects. They did not change mouse weight (Figure S7F). Nor did they affect normal bone cell viability in BICA (Figure S7G). One explanation is that these drugs preferentially affect GJs in cancer cells. Cx43 is upregulated when cancer cells are co-cultured with osteogenic cells. As_2O_3 or danusertib might inhibit this alteration, thereby preventing the formation of heterotypic GJs. For As_2O_3, this is indeed the case: *GJA1* was one of the most downregulated genes in MSC-interacting cancer cells upon As_2O_3 treatment (Figure 7H), which is consistent with a previous finding in leukemia (Chou et al., 2005). By qPCR, we confirmed that the treatment abolished the increase of Cx43 transcription in co-cultures, whereas it exhibited little effects on Cx43 expression in MSCs alone (Figure 7I). The diminished Cx43 expression was possibly due to the As_2O_3-induced reactive oxygen species and oxidation of TFs Sp1 (Chou et al., 2005). Chromatin immunoprecipitation assay confirmed that Sp1 binds to the *GJA1* promoter, which was decreased in As_2O_3-treated cells (Figure S7H). Danusertib did not change Cx43 expression, and might use other mechanisms. Interestingly, aurora kinases, the targets of danusertib by design, can regulate the S421 phosphorylation of MeCP2, and thereby partially abolish the transcriptional output of Ca signaling (Figures 7E and 7F) (Li et al., 2014).

As_2O_3 Inhibits Bone Colonization via Ca Signaling

As_2O_3 may affect many processes in cancer cells. We asked if the efficacies of As_2O_3 are mediated by the heterotypic GJs and Ca signaling. First, blockade of GJs by DN-Cx43 abolished the effects of As_2O_3 in BICA (Figure S8A). Overexpression of a constitutively active (CA) CaMKII mutant (T286D) (Pi et al., 2010) significantly increased resistance to As_2O_3 (Figure S8B) and CBX (Figure S8C) in BICA. Moreover, the doxycycline-induced expression of Cx43 also rescued As_2O_3 treatment (Figure S8C). To quantitate contribution of Ca signaling to the effects of As_2O_3 in the bone ME, we examined dose-response curves of cancer cells with or without expression CA-CaMKII in BICA (Figure S8D). CA-CaMKII expression increased the IC_{50} of As_2O_3 by over 10-fold ($p \leqq 0.001$). More importantly, at a clinically relevant dosage (<0.28 μM, the median plasma arsenic maximum

Figure 6. Inhibition of Cx43 and GJs Retarded Bone Colonization

(A and B) The effect of re-expressing DN-Cx43 on MCF7 (A) and C4-2 (B) cell growth in BICA. n = 12 bone fragments for each group. Representative BL images are shown on the right. p values by Student's t test.

(C) The effect of inducible condition knockout (KO) of *Gja1* in Osx$^+$ lineage cells on MCF7 cell growth in BICA. The experimental group, *Osx1-GFP::Cre*;*Gja1*$^{f/f}$ (*Osx1-cre*;*Gja1*$^{f/f}$) animals with doxycycline withdrawn (KO induced), are compared with control groups, *Osx1-GFP::Cre* (*Osx1-cre*) and *Osx1-GFP::Cre*;*Gja1*$^{f/f}$ on doxycycline. n = 16 for each group. Representative BL images are shown on the right. p values by one-way ANOVA.

(D) A schematic illustration of experiments assessing the effects of inducible overexpression of wild-type Cx43 (WT-Cx43) or DN-Cx43 on bone colonization.

(E) Growth curves of IIA-injected MCF7 cells with indicated genetic perturbation in hind limbs. Error bars = SEM. n = 5 for each group. p values by repeated measures ANOVA test across three groups. Representative BL images are shown on the right.

(F) Normalized, log2-transformed BL intensity of hindlimb bones extracted from the three groups described in (D and E). p values by LSD test.

(G) A schematic illustration of experiments assessing the effects of CBX/MEFL treatment on bone colonization of MCF7 cells.

(H) Growth curves of IIA-injected MCF7 cells in hind limbs. CBX or MEFL treatment last for 4 weeks as indicated by the arrow. Error bars = SEM. n = 5 for each group. p values by repeated measures ANOVA test across three groups. Representative BL images are shown on the right. Veh, vehicle.

(I) BL intensity of hindlimb bones extracted from the three groups described in (G and H). p values by LSD test.

(J) A schematic illustration of experiments assessing the effects of CBX treatment on spontaneous bone metastasis of 4T1.2 cells.

(K) Representative BL images of spontaneous metastases 2 weeks after orthotopic tumor resection.

(L) BL intensity of hind limbs and lungs extracted from control and CBX-treated animals. n = 7 for each group. p values by Student's t tests.

Error bars = SD, except (E and H). See also Figure S6.

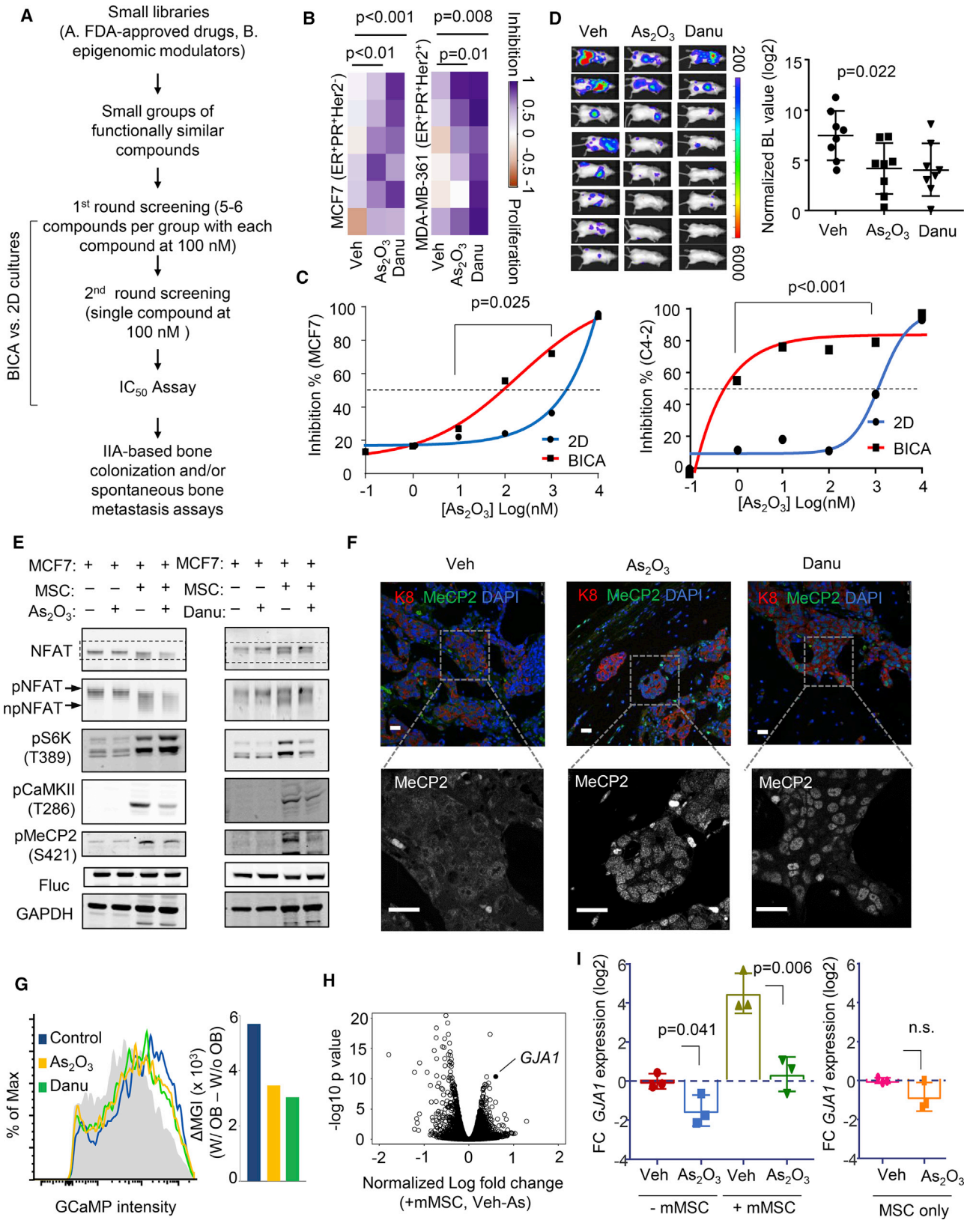

(legend on next page)

concentration of As_2O_3-treated patients at 0.15 mg/kg/day) (Fox et al., 2008), CA-CaMKII expression reverses most cell deaths caused by As_2O_3. Finally, expression of CA-CaMKII almost completely reversed the effects of As_2O_3 in bone colonization assays *in vivo* (Figure 8A). These results indicate that the efficacies of As_2O_3 are dependent, to a large extent, on GJ and Ca signaling.

Unlike As_2O_3, danusertib exerted additional inhibition on DN-Cx43 cells (Figure S8A). Correspondingly, CA-CaMKII only marginally rescued danusertib's effects (Figure S8B), suggesting that danusertib may affect multiple downstream pathways besides Ca signaling (e.g., mTOR).

Transient As_2O_3 Treatment Reduced Latent Bone Recurrence of ER^+ BCa

The luminal subtype of BCa exhibits a stronger bone-tropism than the TN subtype (Kennecke et al., 2010) and is more likely to give rise to late-onset bone metastasis (Zhang et al., 2009), suggesting that some BMM survive adjuvant therapies and persist. Eliminating these BMM is a clinical challenge as they are asymptomatic. One potential solution is to identify potent but safe drugs that can kill BMM by transient treatment in unselected patient population. As_2O_3 is an FDA-approved drug that could be used for this purpose. Since this hypothesis is pertinent to luminal ER^+ BCa and latent metastatic growth, we employed IIA injection of MCF7 cells, which can slowly colonize when directly delivered into bones. We purposely left host animals without extra estradiol so that the systemic estrogen level is lower than normally needed for orthotopic tumor growth. Under this condition, bone colonization could still occur in over 60% of animals after a 2–5 weeks latency time. Treatment of low-dosage As_2O_3 significantly decreased this proportion and resulted longer relapse-free survival (Figure 8B).

The mTOR signaling promotes early-stage bone colonization (Wang et al., 2015). The mTOR inhibitors, such as everolimus, are used to treat endocrine-resistant, metastatic ER^+ BCa (Baselga et al., 2012). In BICA, As_2O_3 and everolimus exhibited additive efficacies (Figure S8E) without additive toxicity (Figure S8F). We asked if combined treatment of everolimus and As_2O_3, under the low-estrogen condition, could further reduce bone colonization. BMM are asymptomatic, precluding preselection of high-risk patients. Therefore, short-term and low-toxicity treatments are strongly desired to balance risk and benefit in an unselected patient population. We kept the everolimus/As_2O_3 treatment for 2 weeks right after IIA injection, and then left the animals untreated. This transient treatment significantly reduced relapses, and achieved a better outcome compared with everolimus treatment alone (Figure 8C). This was corroborated by *ex vivo* bioluminescence intensity and immunohistochemistry analyses of K8 at terminal time point after overt bone metastases developed (Figure 8D). Through micro-computed tomography, we found that everolimus treatment alone significantly increased bone mineral density, which was not much further improved by adding As_2O_3 (Figures 8E and S8G). This suggests that the additional efficacies of As_2O_3 are predominantly through elimination of lesions that are not yet osteolytic. Taken together, these data indicate that short-term As_2O_3 treatment could be added to current standard-of-care to reduce long-latency bone metastasis.

DISCUSSION

The roles of Ca signaling in tumor progression have been well established (Dubois et al., 2014; Prevarskaya et al., 2011). One mechanism to increase cancer cell $[Ca^{2+}]$ is through interactions with the ME niche (Figure 8F). This mechanism is specific to metastatic cells during early-stage bone colonization, when they closely interact with the osteogenic niche cells, and is mediated by GJs, which distinguishes it from other important Ca entry/mobilization mechanisms involving Orai, Stim, and TRPM. Bone is the major Ca reservoir of the entire organism. During bone remodeling, ME $[Ca^{2+}]$ may fluctuate. This remodeling process may alter BMM progression through the changes of Ca signaling. Many processes induce bone remodeling, including microfractures, inflammation, and drug-induced alteration to bone homeostasis. Future studies may provide mechanistic connections of these processes to the increased risk of bone recurrences.

OBs and osteocytes are connected by GJs in the bone, forming a network that readily transmits small molecules among these cells. Once the GJs between cancer cells and OBs are developed and Ca^{2+} is depleted from OBs, it is conceivable that the concentration gradients may drive the flow from

Figure 7. BICA Screening Identified As_2O_3 and Danusertib as Candidate Therapies to Eliminate Cancer Cells Interacting with Osteoblasts

(A) Schematic pipeline of multiplex drug tests using BICA.

(B) Heatmaps showing the efficacies of As_2O_3 (100 nM) and danusertib (100 nM) on MCF7 and MDA-MB-361 cells in BICA. The color scale is based on proportion of proliferation (−1 = 100% cell number increase) and inhibition (1 = 100% cell number decrease). p values by LSD test.

(C) Efficacies of As_2O_3 on indicated cancer cells as a function of dosage in 2D culture or BICA. BL intensity was measured at week 2–3. Mean values of six bone pieces are shown for each dot. p values by repeated measures ANOVA test.

(D) Efficacies of As_2O_3 (1.9 mg/kg) and danusertib (15 mg/kg) on spontaneous bone metastasis of 4T1.2 cells in syngeneic hosts. Treatment started immediately after orthotopic tumor resection. n = 8 for each group. p values by one-way ANOVA test. Error bar = SD.

(E) Western blot shows the indicated (phosphor-)proteins under various (co-)cultures of MCF7 and MSCs, and treatment of 5 μM As_2O_3 or 100 nM danusertib. The gel-shift of NFAT is highlighted in an additional row.

(F) IF staining of MeCP2 in MCF7 bone lesions treated with vehicle, danusertib, or As_2O_3. K8 indicates cancer cells. Single-channel image of MeCP2 highlights cytoplasm or nucleus localization. Scale bars, 25 μm.

(G) The effects of As_2O_3 or danusertib on $[Ca^{2+}]$ in MCF7-OB co-cultures as assessed by GCaMP intensity. The gray area indicates no-OB control. Alteration of median GCaMP intensity (ΔMGI) was used to quantitate the difference and is shown as a bar graph on the right.

(H) "Volcano plot" showing gene expression alteration induced by As_2O_3 treatment in MCF7 co-cultured with MSCs. *GJA1* is indicated.

(I) The effects of 5 μM As_2O_3 on relative *GJA1* expression in cancer cells with or without co-culturing of murine MSCs, quantified by qPCR. *GJA1* expression in mono-culture, vehicle-treated MCF7, or MSC were normalized to 1. Log2-transformed fold change (FC) is plotted. Three biological replicates are included.

p values by Student's t tests. Error bar = SD. Veh, vehicle; Danu, danusertib. See also Figure S7 and Table S1.

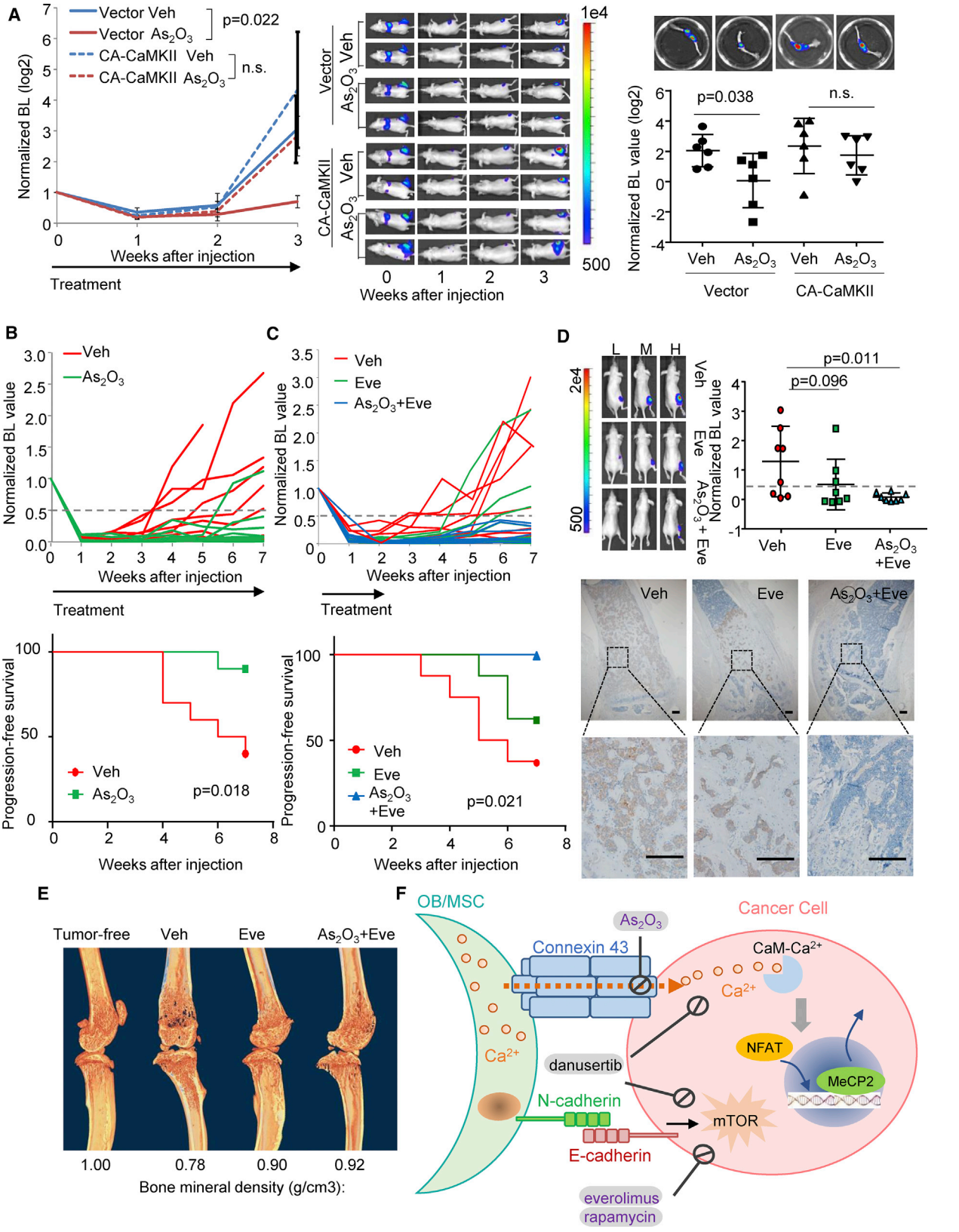

(legend on next page)

connected osteocytes to OBs. This could mean that the Ca reservoir may actually possess a larger capacity, also including the osteocytes buried in the bone matrix.

GJs are increasingly linked to tumor progression and metastasis (Aasen et al., 2016). GJs can serve as tumor suppressors (Plante et al., 2011). Recent studies also suggest that, in specific contexts, GJs may facilitate metastasis or therapeutic resistance (Chen et al., 2016; Osswald et al., 2015). Thus, the function of GJs is context dependent. Chronical inhibition of GJs exhibited severe side effects, as would be expected. Interestingly, As_2O_3 and danusertib can both inhibit GJ and Ca signaling without the same side effects. In particular, As_2O_3 is an FDA-approved drug for treatment of acute promyelocytic leukemia (Zhu et al., 2002). The exact mechanisms underlying its efficacies have not been fully understood. Previous studies suggested that As_2O_3 might affect Ca influx (Raynal et al., 2016). We further showed that *GJA1* is one of the top genes downregulated by As_2O_3 treatment specifically in cancer cells that are interacting with bone cells. The toxicity of As_2O_3 has been intensively investigated and safe regimens have been identified (Fox et al., 2008). As_2O_3 can eradicate cancer cells 10 times more efficiently in the bone ME, making the effective dosage well below the toxicity threshold, providing a rationale for further mechanistic and clinical studies.

Our data highlighted the importance of considering ME in searching for anti-metastasis drugs. The close interaction with osteogenic cells clearly confers cancer cells resistance to some drugs. For instance, a recent study demonstrated that the Notch signaling between cancer cells and the osteogenic niche renders cancer cells resistant to chemotherapies (Zheng et al., 2017). However, this interaction also confers vulnerability to other drugs, sometimes unexpectedly. Ca^{2+} flow from osteogenic cells to cancer cells is underlying some of these alterations. The unique *ex vivo* and *in vivo* platforms we developed in previous studies (Wang et al., 2015, 2017) were essential for the discoveries. In particular, BICA significantly accelerated our search for bone metastasis therapies.

STAR★METHODS

Detailed methods are provided in the online version of this paper and include the following:

- KEY RESOURCES TABLE
- CONTACT FOR REAGENT AND RESOURCE SHARING
- EXPERIMENTAL MODEL AND SUBJECT DETAILS
  - Animals
  - Cell Lines
- METHOD DETAILS
  - IIA Injection and IVIS Imaging
  - Spontaneous Bone Metastasis Assay
  - Pharmacological Treatment
  - Bone-in-Culture Array (BICA)
  - Drug Screening
  - Recombinant DNA Generation
  - 3D Co-culture Assay
  - Western Blot
  - Immunofluorsent and Immunohistochemical Staining
  - Flow Cytometry
  - MicroCT (μCT) Analysis
  - RNA Isolation and qRT-PCR Analysis
  - Chromatin Immunoprecipitation (ChIP)-Assay
  - RNA-Seq Experiment
- QUANTIFICATION AND STATISTICAL ANALYSIS
- DATA AND SOFTWARE AVAILABILITY

SUPPLEMENTAL INFORMATION

Supplemental Information includes eight figures and one table and can be found with this article online at https://doi.org/10.1016/j.ccell.2018.10.002.

ACKNOWLEDGMENTS

We thank the Zhang Laboratory members for helpful input. We thank Max Wicha, Eric Chang, Dasgupta Subhamoy, Robin. L. Anderson, Thomas Westbrook, and Florent Elefteriou for reagents. X.H.-F.Z. is supported by the US Department of Defense DAMD W81XWH-16-1-0073, NCI CA183878, the Breast Cancer Research Foundation, and the McNair Medical Institute. H.W. is supported in part by the US Department of Defense DAMD W81XWH-13-1-0296. X.H.-F.Z. and S.T.C.W. are supported by NIH U01188388, NIH U54CA149196, CPRIT RP110532-C1, and John S Dunn Research Foundation. We also acknowledge the Pathology Core of Lester and Sue Smith Breast Center and the Dan L. Duncan Cancer Center, and Cell Sorting Core (CCSC) at Baylor College of Medicine.

AUTHOR CONTRIBUTIONS

Conceptualization, H.W., L.T., I.B., W.Z., B.R.A., Z.L., M.Y., S.D., H.Z., D.R.R., S.T.C.W., Z.G., and X.H.-F.Z.; Methodology, Formal Analysis and Investigation, H.W., L.T., J.L., A.G., I.B., W.Z., Z.G., and X.H.-F.Z.; Resources, B.R.A., Z.L., M.Y., S.D., H.Z., D.R.R., S.T.C.W., Z.G., and X.H.-F.Z.; Software Data Curation and Visualization, H.W., L.T., I.B., Z.G., and X.H.-F.Z.; Writing – Original

Figure 8. Adjuvant Transient As_2O_3 Treatment of Reduced Latent Bone Recurrence of ER^+ Breast Cancer

(A) Quantification (left) and representative BL images (middle) of *in vivo* bone colonization kinetics of IIA-injected MCF7 cells expressing empty vectors or CA-CaMKII treated with vehicles or As_2O_3 (n = 6 for each group) and quantitation and representative BL images (right) of BL intensity (normalized, log2-transformed) of extracted bones. p values by repeated measures ANOVA (left) or LSD test (right). Error bars = SEM.

(B) Growth curves of individual bone lesions in vehicle and As_2O_3 groups (top) and Kaplan-Meier curves of the indicated groups (bottom). n = 10 for both groups. The arrow indicates duration of treatment. The endpoint is defined as the time point when hindlimb signal intensity reaches half of the day 0 value (normalized bioL intensity >0.5) and continues to increase at subsequent time points. p values by log rank test.

(C) Growth curves of individual bone lesions in vehicle-, everolimus-, and combined As_2O_3 and everolimus-treated groups (top) and Kaplan-Meier curves of different groups with indicated treatments (bottom). n = 8 for each group. The arrow, endpoint and p values are defined as in (B).

(D) Top left: representative BL images showing high (H), median (M), and low (L) signals in each group. Top right: quantitation of BL intensity. Bottom: representative IHC staining of bone lesions. Tumor lesions were indicated by K8 staining. Error bars = SD. p values by LSD tests. Scale bar, 100 μm.

(E) Micro-computed tomography scanning of hindlimb bones of tumor-free animal and representative animals in different treatment groups in (C and D). Bone mineral density values are shown below the images.

(F) Schematic model for interaction between osteogenic cells and cancer cells in bone colonization. FDA-approved drugs are indicated by purple font.

Veh, vehicle; Eve, everolimus. See also Figure S8.

Draft, H.W. and X.H.-F.Z.; Writing – Review & Editing, H.W., L.T., I.B., W.Z., D.R.R., S.T.C.W., Z.G., and X.H.-F.Z.; Funding Acquisition, H.W., S.T.C.W., and X.H.-F.Z.; Supervision, X.H.-F.Z.

DECLARATION OF INTERESTS

The authors declare no competing interests.

Received: January 19, 2018
Revised: July 10, 2018
Accepted: October 2, 2018
Published: November 12, 2018

REFERENCES

Aasen, T., Mesnil, M., Naus, C.C., Lampe, P.D., and Laird, D.W. (2016). Gap junctions and cancer: communicating for 50 years. Nat. Rev. Cancer *16*, 775–788.

Baselga, J., Campone, M., Piccart, M., Burris, H.A., 3rd, Rugo, H.S., Sahmoud, T., Noguchi, S., Gnant, M., Pritchard, K.I., Lebrun, F., et al. (2012). Everolimus in postmenopausal hormone-receptor-positive advanced breast cancer. N. Engl. J. Med. *366*, 520–529.

Berridge, M.J., Bootman, M.D., and Roderick, H.L. (2003). Calcium: calcium signalling: dynamics, homeostasis and remodelling. Nat. Rev. Mol. Cell Biol. *4*, 517–529.

Boyce, B.F., Yoneda, T., and Guise, T.A. (1999). Factors regulating the growth of metastatic cancer in bone. Endocr. Relat. Cancer *6*, 333–347.

Buchthal, B., Lau, D., Weiss, U., Weislogel, J.M., and Bading, H. (2012). Nuclear calcium signaling controls methyl-CpG-binding protein 2 (MeCP2) phosphorylation on serine 421 following synaptic activity. J. Biol. Chem. *287*, 30967–30974.

Chen, T.-W., Wardill, T.J., Sun, Y., Pulver, S.R., Renninger, S.L., Baohan, A., Schreiter, E.R., Kerr, R.A., Orger, M.B., Jayaraman, V., et al. (2013). Ultrasensitive fluorescent proteins for imaging neuronal activity. Nature *499*, 295–300.

Chen, Q., Boire, A., Jin, X., Valiente, M., Er, E.E., Lopez-Soto, A., Jacob, L., Patwa, R., Shah, H., Xu, K., et al. (2016). Carcinoma–astrocyte gap junctions promote brain metastasis by cGAMP transfer. Nature *533*, 493–498.

Chou, W.C., Chen, H.Y., Yu, S.L., Cheng, L., Yang, P.C., and Dang, C.V. (2005). Arsenic suppresses gene expression in promyelocytic leukemia cells partly through Sp1 oxidation. Blood *106*, 304–310.

Dubois, C., Vanden Abeele, F., Lehen'kyi, V., Gkika, D., Guarmit, B., Lepage, G., Slomianny, C., Borowiec, A., Bidaux, G., Benahmed, M., et al. (2014). Remodeling of channel-forming ORAI proteins determines an oncogenic switch in prostate cancer. Cancer Cell *26*, 19–32.

Ell, B., and Kang, Y. (2012). SnapShot: bone metastasis. Cell *151*, 690–690.e1.

Fournier, P.G.J., Juárez, P., Jiang, G., Clines, G.A., Niewolna, M., Kim, H.S., Walton, H.W., Peng, X.H., Liu, Y., Mohammad, K.S., et al. (2015). The TGF-β signaling regulator PMEPA1 suppresses prostate cancer metastases to bone. Cancer Cell *27*, 809–821.

Fox, E., Razzouk, B.I., Widemann, B.C., Xiao, S., O'Brien, M., Goodspeed, W., Reaman, G.H., Blaney, S.M., Murgo, A.J., Balis, F.M., et al. (2008). Phase 1 trial and pharmacokinetic study of arsenic trioxide in children and adolescents with refractory or relapsed acute leukemia, including acute promyelocytic leukemia or lymphoma. Blood *111*, 566–573.

Fraedrich, K., Schrader, J., Ittrich, H., Keller, G., Gontarewicz, A., Matzat, V., Kromminga, A., Pace, A., Moll, J., Bläker, M., et al. (2012). Targeting aurora kinases with danusertib (PHA-739358) inhibits growth of liver metastases from gastroenteropancreatic neuroendocrine tumors in an orthotopic xenograft model. Clin. Cancer Res. *18*, 4621–4632.

Ghajar, C.M., Peinado, H., Mori, H., Matei, I.R., Evason, K.J., Brazier, H., Almeida, D., Koller, A., Hajjar, K.A., Stainier, D.Y.R., et al. (2013). The perivascular niche regulates breast tumour dormancy. Nat. Cell Biol. *15*, 807–817.

Di Giorgio, E., Franforte, E., Cefalù, S., Rossi, S., Dei Tos, A.P., Brenca, M., Polano, M., Maestro, R., Paluvai, H., Picco, R., et al. (2017). The co-existence of transcriptional activator and transcriptional repressor MEF2 complexes influences tumor aggressiveness. PLoS Genet. *13*, e1006752.

Hänzelmann, S., Castelo, R., and Guinney, J. (2013). GSVA: gene set variation analysis for microarray and RNA-Seq data. BMC Bioinformatics *14*, 7.

Huang, C.K., Tsai, M.Y., Luo, J., Kang, H.Y., Lee, S.O., and Chang, C. (2013). Suppression of androgen receptor enhances the self-renewal of mesenchymal stem cells through elevated expression of EGFR. Biochim. Biophys. Acta *1833*, 1222–1234.

Ishikawa, M., Iwamoto, T., Nakamura, T., Doyle, A., Fukumoto, S., and Yamada, Y. (2011). Pannexin 3 functions as an ER Ca 2+ channel, hemichannel, and gap junction to promote osteoblast differentiation. J. Cell Biol. *193*, 1257–1274.

Jiang, J.X., Siller-Jackson, A.J., and Burra, S. (2007). Roles of gap junctions and hemichannels in bone cell functions and in signal transmission of mechanical stress. Front. Biosci. *12*, 1450–1462.

Kang, Y., Siegel, P.M., Shu, W., Drobnjak, M., Kakonen, S.M., Cordon-Cardo, C., Guise, T.A., and Massague, J. (2003). A multigenic program mediating breast cancer metastasis to bone. Cancer Cell *3*, 537–549.

Keiser, J., Manneck, T., and Vargas, M. (2011). Interactions of mefloquine with praziquantel in the *Schistosoma mansoni* mouse model and in vitro. J. Antimicrob. Chemother. *66*, 1791–1797.

Kennecke, H., Yerushalmi, R., Woods, R., Cheang, M.C., Voduc, D., Speers, C.H., Nielsen, T.O., and Gelmon, K. (2010). Metastatic behavior of breast cancer subtypes. J. Clin. Oncol. *28*, 3271–3277.

Kumar, A., Coleman, I., Morrissey, C., Zhang, X., True, L.D., Gulati, R., Etzioni, R., Bolouri, H., Montgomery, B., White, T., et al. (2016). Substantial interindividual and limited intraindividual genomic diversity among tumors from men with metastatic prostate cancer. Nat. Med. *22*, 369–378.

Li, H., Zhong, X., Chau, K.F., Santistevan, N.J., Guo, W., Kong, G., Li, X., Kadakia, M., Masliah, J., Chi, J., et al. (2014). Cell cycle-linked MeCP2 phosphorylation modulates adult neurogenesis involving the Notch signalling pathway. Nat. Commun. *5*, 5601.

Luo, X., Fu, Y., Loza, A.J., Murali, B., Leahy, K.M., Ruhland, M.K., Gang, M., Su, X., Zamani, A., Shi, Y., et al. (2016). Stromal-initiated changes in the bone promote metastatic niche development. Cell Rep. *14*, 82–92.

Macian, F. (2005). NFAT proteins: key regulators of T-cell development and function. Nat. Rev. Immunol. *5*, 472–484.

Mackiewicz-Wysocka, M., Pankowska, M., and Wysocki, P.J. (2012). Progress in the treatment of bone metastases in cancer patients. Expert Opin. Investig. Drugs *21*, 785–795.

Massagué, J., and Obenauf, A.C. (2016). Metastatic colonization by circulating tumour cells. Nature *529*, 298–306.

McKinsey, T.A., Zhang, C.L., and Olson, E.N. (2002). MEF2: a calcium-dependent regulator of cell division, differentiation and death. Trends Biochem. Sci. *27*, 40–47.

Morecki, S., Moshel, Y., Gelfend, Y., Pugatsch, T., and Slavin, S. (1997). Induction of graft vs. tumor effect in a murine model of mammary adenocarcinoma. Int. J. Cancer *71*, 59–63.

Osswald, M., Jung, E., Sahm, F., Solecki, G., Venkataramani, V., Blaes, J., Weil, S., Horstmann, H., Wiestler, B., Syed, M., et al. (2015). Brain tumour cells interconnect to a functional and resistant network. Nature *528*, 93–98.

Pi, H.J., Otmakhov, N., El Gaamouch, F., Lemelin, D., De Koninck, P., and Lisman, J. (2010). CaMKII control of spine size and synaptic strength: role of phosphorylation states and nonenzymatic action. Proc. Natl. Acad. Sci. U S A *107*, 14437–14442.

Plante, I., Stewart, M.K.G., Barr, K., Allan, A.L., and Laird, D.W. (2011). Cx43 suppresses mammary tumor metastasis to the lung in a Cx43 mutant mouse model of human disease. Oncogene *30*, 1681–1692.

Plotkin, L.I., and Bellido, T. (2013). Beyond gap junctions: connexin43 and bone cell signaling. Bone *52*, 157–166.

Prevarskaya, N., Skryma, R., and Shuba, Y. (2011). Calcium in tumour metastasis: new roles for known actors. Nat. Rev. Cancer *11*, 609–618.

Price, T.T., Burness, M.L., Sivan, A., Warner, M.J., Cheng, R., Lee, C.H., Olivere, L., Comatas, K., Magnani, J., Kim Lyerly, H., et al. (2016). Dormant breast cancer micrometastases reside in specific bone marrow niches that regulate their transit to and from bone. Sci. Transl. Med. *8*, 340ra73.

Raynal, N.J.M., Lee, J.T., Wang, Y., Beaudry, A., Madireddi, P., Garriga, J., Malouf, G.G., Dumont, S., Dettman, E.J., Gharibyan, V., et al. (2016). Targeting calcium signaling induces epigenetic reactivation of tumor suppressor genes in cancer. Cancer Res. *76*, 1494–1505.

Roscoe, W., Veitch, G.I.L., Gong, X.Q., Pellegrino, E., Bai, D., McLachlan, E., Shao, Q., Kidder, G.M., and Laird, D.W. (2005). Oculodentodigital dysplasia-causing connexin43 mutants are non-functional and exhibit dominant effects on wild-type connexin43. J. Biol. Chem. *280*, 11458–11466.

Ross, M.H., Esser, A.K., Fox, G.C., Schmieder, A.H., Yang, X., Hu, G., Pan, D., Su, X., Xu, Y., Novack, D.V., et al. (2017). Bone-induced expression of integrin β3 enables targeted nanotherapy of breast cancer metastases. Cancer Res. *77*, 6299–6312.

Sethi, N., Dai, X., Winter, C.G., and Kang, Y. (2011). Tumor-derived JAGGED1 promotes osteolytic bone metastasis of breast cancer by engaging notch signaling in bone cells. Cancer Cell *19*, 192–205.

Shahbazian, M.D., Young, J.I., Yuva-Paylor, L.A., Spencer, C.M., Antalffy, B.A., Noebels, J.L., Armstrong, D.L., Paylor, R., and Zoghbi, H.Y. (2002). Mice with truncated MeCP2 recapitulate many Rett syndrome features and display hyperacetylation of histone H3. Neuron *35*, 243–254.

Sharma, S., Findlay, G.M., Bandukwala, H.S., Oberdoerffer, S., Baust, B., Li, Z., Schmidt, V., Hogan, P.G., Sacks, D.B., and Rao, A. (2011). Dephosphorylation of the nuclear factor of activated T cells (NFAT) transcription factor is regulated by an RNA-protein scaffold complex. Proc. Natl. Acad. Sci. U S A *108*, 11381–11386.

Shaw, R.M., Fay, A.J., Puthenveedu, M.A., von Zastrow, M., Jan, Y.N., and Jan, L.Y. (2007). Microtubule plus-end-tracking proteins target gap junctions directly from the cell interior to adherens junctions. Cell *128*, 547–560.

Shibasaki, F., Price, E.R., Milan, D., and McKeon, F. (1996). Role of kinases and the phosphatase calcineurin in the nuclear shuttling of transcription factor NF-AT4. Nature *382*, 370–373.

Smid, M., Wang, Y., Zhang, Y., Sieuwerts, A.M., Yu, J., Klijn, J.G., Foekens, J.A., and Martens, J.W. (2008). Subtypes of breast cancer show preferential site of relapse. Cancer Res. *68*, 3108–3114.

Subramanian, A., Tamayo, P., Mootha, V.K., Mukherjee, S., Ebert, B.L., Gillette, M.A., Paulovich, A., Pomeroy, S.L., Golub, T.R., Lander, E.S., et al. (2005). Gene set enrichment analysis: a knowledge-based approach for interpreting genome-wide expression profiles. Proc. Natl. Acad. Sci. U S A *102*, 15545–15550.

Tripathi, M.K., Deane, N.G., Zhu, J., An, H., Mima, S., Wang, X., Padmanabhan, S., Shi, Z., Prodduturi, N., Ciombor, K.K., et al. (2014). Nuclear factor of activated T-cell activity is associated with metastatic capacity in colon cancer. Cancer Res. *74*, 6947–6957.

Wan, L., Pantel, K., and Kang, Y. (2013). Tumor metastasis: moving new biological insights into the clinic. Nat. Med. *19*, 1450–1464.

Wang, H., Yu, C., Gao, X., Welte, T., Muscarella, A.M., Tian, L., Zhao, H., Zhao, Z., Du, S., Tao, J., et al. (2015). The osteogenic niche promotes early-stage bone colonization of disseminated breast cancer cells. Cancer Cell *27*, 193–210.

Wang, H., Tian, L., Goldstein, A., Liu, J., Lo, H.-C., Sheng, K., Welte, T., Wong, S.T.C., Gugala, Z., Stossi, F., et al. (2017). Bone-in-culture array as a platform to model early-stage bone metastases and discover anti-metastasis therapies. Nat. Commun. *8*, 15045.

Waning, D.L., Mohammad, K.S., Reiken, S., Xie, W., Andersson, D.C., John, S., Chiechi, A., Wright, L.E., Umanskaya, A., Niewolna, M., et al. (2015). Excess TGF-β mediates muscle weakness associated with bone metastases in mice. Nat. Med. *21*, 1262–1271.

Weilbaecher, K.N., Guise, T.A., and McCauley, L.K. (2011). Cancer to bone: a fatal attraction. Nat. Rev. Cancer *11*, 411–425.

Wu, P., Wang, Y., Davis, M.E., Zuckerman, J.E., Chaudhari, S., Begg, M., and Ma, R. (2015). Store-operated Ca^{2+} channels in mesangial cells inhibit matrix protein expression. J. Am. Soc. Nephrol. *26*, 2691–2702.

Yu, C., Wang, H., Muscarella, A., Goldstein, A., Zeng, H.-C., Bae, Y., Lee, B.H.I., and Zhang, X.H.-F. (2016). Intra-iliac artery injection for efficient and selective modeling of microscopic bone metastasis. J. Vis. Exp. 1–7, https://doi.org/10.3791/53982.

Zhang, X.H.F., Wang, Q., Gerald, W., Hudis, C.A., Norton, L., Smid, M., Foekens, J.A., and Massagué, J. (2009). Latent bone metastasis in breast cancer tied to Src-dependent survival signals. Cancer Cell *16*, 67–78.

Zhang, X.H.-F., Giuliano, M., Trivedi, M.V., Schiff, R., and Osborne, C.K. (2013a). Metastasis dormancy in estrogen receptor-positive breast cancer. Clin. Cancer Res. *19*, 6389–6397.

Zhang, X.H.F., Jin, X., Malladi, S., Zou, Y., Wen, Y.H., Brogi, E., Smid, M., Foekens, J.A., and Massagué, J. (2013b). Selection of bone metastasis seeds by mesenchymal signals in the primary tumor stroma. Cell *154*, 1060–1073.

Zheng, H., Bae, Y., Kasimir-Bauer, S., Tang, R., Chen, J., Ren, G., Yuan, M., Esposito, M., Li, W., Wei, Y., et al. (2017). Therapeutic antibody targeting tumor- and osteoblastic niche-derived jagged1 sensitizes bone metastasis to chemotherapy. Cancer Cell *32*, 731–747.e6.

Zhu, Q., Zhang, J.W., Zhu, H.Q., Shen, Y.L., Flexor, M., Jia, P.M., Yu, N., Cai, X., Waxman, S., Lanotte, M., et al. (2002). Synergic effects of arsenic trioxide and cAMP during acute promyelocytic leukemia cell maturation subtends a novel signaling crosstalk. Blood *99*, 1014–1022.

STAR★METHODS

KEY RESOURCES TABLE

REAGENT or RESOURCE	SOURCE	IDENTIFIER
Antibodies		
NFAT1 in 1:200 (IF) or 1:1000(WB), Rabbit	Cell Signaling Technology	Cat#5861S; RRID:AB_10835147
pS6K(T389) in 1:1000(WB), Rabbit	Cell Signaling Technology	Cat#9234S; RRID:AB_2269803
pCamKII(T286) in 1:1000 (WB), Rabbit	Cell Signaling Technology	Cat#12716S; RRID:AB_2713889
MeCP2 in 1:200 (IF) or 1:1000(WB), Rabbit	Cell Signaling Technology	Cat#3456S; RRID:AB_2143849
pMeCP2(S421) in 1:1000(WB), Rabbit	Rockland	Cat#600-401-X14; RRID:AB_2614557
Firefly luciferase in 1:5000 (WB), Rabbit	Thermo	Cat#PA5-32209; RRID:AB_2549682
SP1 antibody (Chip grade)	Cell Signaling Technology	CST # 9389S; RRID:AB_11220235
normal rabbit IgG	Cell Signaling Technology	CST # 2729S; RRID:AB_1031062
Cx43 in 1:200 (IF), Rabbit	Sigma	Cat#C6219; RRID:AB_476857
Chemicals, Peptides, and Recombinant Proteins		
D-luciferin	Goldbio	Cat# LUCNA-1G
Carbenoxolone	Sigma	Cat# C4790
Mefloquine	Sigma	Cat#1379059
Danusertib	ApexBio	Cat# A4116
Nifedipine	ApexBio	Cat#B1988
SKF96365	ApexBio	Cat#B6616
Arsenic trioxide	Sigma	Cat# A1010
John Hopkins University Clinical Compound Library	gift from Dr. Stephen T. C. Wong's laboratory at Houston Methodist Research Institute	NA
Everolimus	ApexBio	Cat# A8169
Critical Commercial Assays		
Nextera XT DNA Library Prep Kit	Illumina	Cat# FC-131-1096
Nextseq 500/550 high output v2 kit	Illumina	Cat# FC-404-2002
Deposited Data		
breast cancer metastases dataset	GEO	GSE46141
human breast cancer metastases dataset in different organs	GEO	GSE14020
Stroma cells in the breast cancer microenvironment	GEO	GSE27120
Cancer-osteoblast heterotypic interactions dataset	GEO	GSE29036
Subpopulations of MDA-MB-231 and Primary Breast Cancers	GEO	GSE2603
Breast cancer relapse free survival and lung metastasis free survival	GEO	GSE5327
Breast cancer relapse free survival	GEO	GSE2034
Expression data from primary breast tumors	GEO	GSE12276
Metastatic prostate cancer dataset	GEO	GSE77930
in vivo Bone Lesion (IVBL) and Orthotopic tumors dataset	GEO	GSE110451
ATO treatment on mesenchymal stem cells (MSCs) interacting breast cancer cells	GEO	GSE118923
Experimental Models: Cell Lines		
Human breast cancer MCF7	ATCC	Cat# HTB-22; RRID: CVCL_0031
Human breast cancer MDA-MB-361	ATCC	Cat# HTB-27; RRID: CVCL_0620
Mouse pre-osteoclast RAW264.7	ATCC	Cat# TIB-71; RRID: CVCL_0493

(*Continued on next page*)

Continued

REAGENT or RESOURCE	SOURCE	IDENTIFIER
Human monocyte U937	ATCC	Cat# CRL-1593.2; RRID: CVCL_0007
Mouse breast cancer 4T1	Barbara Ann Karmanos Cancer Center	RRID: CVCL_0125
Mouse breast cancer 4TO7	Barbara Ann Karmanos Cancer Center	RRID: CVCL_B383
Mouse breast cancer 4T1.2	Gift from Dr. Robin Anderson at Peter MacCallum Cancer Center	RRID: CVCL_GR32
Human Mesenchymal stem cell	gift from Dr. Max Wicha's laboratory at University of Michigan	
Human osteocyte MLO-Y4	gift from Dr. Florent Elefteriou at Baylor College of Medicine	RRID: CVCL_M098
Human Astrocyte	ScienceCell	Catalog #1800
Human mammary fibroblast cell	gift from Dr. Eric Chang's laboratory at Baylor College of Medicine	
Mouse fibroblast NIH3T3	ATCC	Cat# CRL-1658; RRID: CVCL_0594
Human pre-Osteoblast hFOB1.19	ATCC	Cat#CRL-11372; RRID: CVCL_3708
Human prostate cancer C4-2, Fluc^{+}	gift from Dr. Dasgupta Subhamoy's lab at Roswell Park Comprehensive Cancer Center	
Human prostate cancer 22RV1	ATCC	Cat#CRL-2505; RRID: CVCL_1045
Experimental Models: Organisms/Strains		
Mouse Bal/cJ	Envigo	NA
Mouse C57BL/6	Envigo	NA
Athymic nude mice	Envigo	NA
Osx1-GFP::Cre mice	Jackson Laboratory	Cat#006361
Gja1 flox mice	Jackson Laboratory	Cat#008039
Cdh2 flox mice	Jackson Laboratory	Cat#007611
Oligonucleotides		
FAP-F	Tripathi et al., 2014	TGGCGATGAACAATATCCTAGA
FAP-R	Tripathi et al., 2014	ATCCGAACAACGGGATTCTT
ACTB-F	This paper	GTTGTCGACGACGAGCG
ACTB-R	This paper	GCACAGAGCCTCGCCTT
TWIST1_F	Tripathi et al., 2014	AGCTACGCCTTCTCGGTCT
TWIST1_R	Tripathi et al., 2014	TCCTTCTCTGGAAACAATGACA
MRC2_F	Tripathi et al., 2014	AACTTCCGGGACAGTCTGG
MRC2_R	Tripathi et al., 2014	TTACAGGGACTGTCGTTCCA
COL3AL_F	Tripathi et al., 2014	ACTGGAGCACGGGGTCTT
COL3AL_R	Tripathi et al., 2014	TCCTGGTTTCCCACTTTCAC
ANGPTL2_F	Tripathi et al., 2014	GCCCACTATGCCCACTCTC
ANGPTL2_R	Tripathi et al., 2014	CTGCAGGCAGTCTCTCCAT
MGP_F	Tripathi et al., 2014	TGAAAGCATGGAATCTTATGAACTT
MGP_R	Tripathi et al., 2014	CTGCTGAGGGGATATGAAGG
PTRF_F	Tripathi et al., 2014	CAGCGTCAACGTGAAGACC
PTRF_R	Tripathi et al., 2014	CCGGCAGCTTCACTTCAT
MECP2_F	This Paper	GCGAGGAGGAGAGACTGGA
MECP2_R	This Paper	TTTAAACTTGAGGGGTTTGTCC
GJA1-F	This Paper	TCCTCCTCTTTCTTGTTCAGTTTCTCT
GJA1-R	This Paper	CCTGCAGATCATATTTGTGTCTGTTC
GAPDH-F	This Paper	TTGAGGTCAATGAAGGGGTC
GAPDH-R	This Paper	GAAGGTGAAGGTCGGAGTCA

(*Continued on next page*)

Continued

REAGENT or RESOURCE	SOURCE	IDENTIFIER
Actb-F	This Paper	GGCTGTATTCCCCTCCATCG
Actb-R	This Paper	CCAGTTGGTAACAATGCCATGT
Nfatc1_F	This Paper	TCCAAAGTCATTTTCGTGGA
Nfatc1_R	This Paper	CTTTGCTTCCATCTCCCAGA
Nfatc2_F	This Paper	CAACGGAAAGAGGAAACGAA
Nfatc2_R	This Paper	CTGTCTTGATGGCAGGGACT
Gapdh-F	This Paper	AGGTCGGTGTGAACGGATTTG
Gapdh-R	This Paper	TGTAGACCATGTAGTTGAGGTCA
FW-SP1-CX43	This Paper	ACTGCTGCTCTTTGCCTCTT
RV-SP1-CX43	This Paper	TGTAACTTGGAGCACAGAGCTT
Recombinant DNA		
pMD2.G	Addgene	Cat#12259
psPAX2		Cat#12260
pwpt-Fluc/GFP or pwpt-Fluc/RFP	Wang et al., 2015	
pHAGE-RSV-GCaMP6s	Addgene	Cat#80146
pInducer22	gift from Dr. Thomas Westbrook's lab at Baylor College of Medicine	
pInducer22-DN-Ecad	Wang et al., 2015	
pInducer22-WT-Cx43	This paper	
pInducer22-DN-Cx43(G138R)	This paper	
pInducer22-DN-CaMKII(T286A)	This paper	
pInducer22-CA-CaMKII(T286D)	This paper	
pInducer22-DN-Calcineurin(delta H160Q)	This paper	
Software and Algorithms		
ImageJ	National Institute of Health	NA
Cyverse	National Science Foundation	Award Numbers DBI-0735191 and DBI-1265383
R 3.3.4	R Core Team	NA
Graphpad Prism7	GraphPad Software, Inc.	NA
Flow Jo v10.0.	FlowJo, LLC	NA
SPSS 19	IBM	NA
Other		
Code of analysis by R programming	This paper	https://github.com/lethesea/Targeting-calcium-signaling-in-bone-micrometastases

CONTACT FOR REAGENT AND RESOURCE SHARING

Further information and requests for resources or reagents should be directed to the lead contact Dr. Xiang H.-F. Zhang at xiangz@bcm.edu

EXPERIMENTAL MODEL AND SUBJECT DETAILS

Animals

Athymic nude mice and Balb/c mice were purchased from Envigo. *Osx1-GFP::Cre* mice, *Gja* ^{flox} mice and *Cdh2* ^{flox} mice were purchased from Jackson Laboratories (stock numbers: 006361; 008039; and 007611, respectively). These strains were intercrossed to produce experimental cohorts *Osx1-GFP::Cre;Cdh2* $^{f/f}$ *and Osx1-GFP::Cre;Gja1* $^{f/f}$ mice. Mice genotyping was performed under the guidance of JAX genotyping protocol. To halt EGFP/Cre fusion protein expression, doxycycline was added to water bottles at a final concentration of 200 mg/L and changed weekly until 2 weeks before the experiment. The 5- to 7-week-old female mice were used in all *in vivo*/BICA experiments. In the regular tumor model using ER+ human breast cancer cells (e.g. MCF7 cells), estradiol tubes were prepared and transplanted to nude mice before cancer cell injection. All animal work was done in accordance with a protocol approved by the Baylor College of Medicine Institutional Animal Care and Use Committee.

Cell Lines

Human breast cancer cell lines MCF7 and MDA-MB-361, human prostate cancer cell line C4-2 and 22Rv1, mouse pre-osteoclast RAW264.7, human monocyte U937, mouse fibroblast NIH 3T3 and human osteoblast hFOB1.19 cells were obtained from ATCC. Mouse breast cancer cell lines 4T1 and 4TO7 cells were purchased from Barbara Ann Karmanos Cancer Center. Human astrocytes were purchased from ScienCell. All these purchased cells were maintained under the manufacturer's recommended media.

4T1.2 cell was a generous gift from Dr. Robin Anderson at Peter MacCallum Cancer Center and cultured in DMEM supplemented with 10% FBS, 1% penicillin-streptomycin, and 0.2% Amphotericin B. The immortalized MSC cell line was a generous gift from Dr. Max Wicha's laboratory at University of Michigan and was cultured in alpha-MEM supplemented with 10% FBS, 1% penicillin-streptomycin, and 0.2% Amphotericin B. The osteocyte cell line MLO-Y4 was gifted from Dr. Florent Elefteriou at Baylor College of Medicine and cultured in alpha-MEM culture medium containing 2.5% FBS and 2.5% Calf Serum. The human mammary fibroblast cell was gifted from Dr. Eric Chang at Baylor College of Medicine and cultured in DMEM supplemented with 10% FBS, 1% penicillin-streptomycin, and 0.2% Amphotericin B. Fluc/GFP labelled C4-2 cell was a generous gift from Dr. Dasgupta Subhamoy's lab at Roswell Park Comprehensive Cancer Center.

METHOD DETAILS

IIA Injection and IVIS Imaging

Intra-iliac injections and IVIS imaging were performed as previously described (Wang et al., 2015; Yu et al., 2016). Briefly, mice were anesthetized by isoflurane or ketamine (100 mg/kg body weight) and xylazine (10 mg/kg body weight) mixture, and then restrained on a Far Infraired Warming Pad (Kent Scientific). A 1.5 cm incision was made between the 4^{th} and 5^{th} nipples in the lower right abdomen. Blunt dissection was performed to separate muscles and expose the common iliac artery. 5 $X10^5$ MCF7 or C4-2 cancer cells were suspended in 0.1 ml PBS were injected via 31G needles. A cotton tip was used to press the artery incision area to stop bleeding (in about 5-10 min). The wound was then closed by a 9 mm EZ clip. All mice receiving IIA injection were monitored until awake and moving normally. In the regular IIA model injecting MCF7 in nude mice, estradiol pellet was implanted under the back neck skin to accelerate the tumor lesion formation. In the ''latency'' model (Figures 8B and 8C), no estradiol was provided to mice. When induced protein expression was demanded, 200 mg/L doxycycline in water was administered to animals right after injection till the end of experiments.

Bioluminescence signaling was checked by injection of 100 μl 15 mg/ml sterilized firefly luciferase substrate D-luciferin (LUCNA-1G, Goldbio) via the intra-orbital sinus. Animals were imaged weekly using IVIS Lumina II (Advanced Molecular Vision). The acquired bioluminescence signals were normalized by the day 0 intensity around the knee joint other than the entire hind limb.

Spontaneous Bone Metastasis Assay

The spontaneous bone metastasis assay was performed as previously described (Wang et al., 2015). Briefly, BALB/c mice recieved mammary fat pad injections of $1X10^5$ 4T1.2 cells suspended in physiological saline with 50% Growth Factor Reduced Matrigel Matrix. Surgical resection was used to remove the tumors when tumors reached >7 mm in diameter. Mice were then randomized into different groups to initialize treatment and closely monitored for up to 2 weeks. Whole-body bioluminescence imaging was performed before mice were sacrificed. BL signals from spines and hind limbs regions were quantified as bone metastasis. Hind limb bones and lungs were extracted right after euthanasia for *ex vivo* bioluminescence imaging.

Pharmacological Treatment

The administration of carbenoxolone, mefloquine and danusertib followed previous reports (Fraedrich et al., 2012; Keiser et al., 2011; Morecki et al., 1997) whereas the dose of the two FDA-approved drugs, everolimus and arsenic trioxide were adjusted from clinical human dose by FDA guidance: mouse dose(mg/kg)=human dose X mouse Km (~37) / mouse Km (~3). Carbenoxolone (CBX, C4790 Sigma) was injected i.p. daily at the dosage of 30 mg/kg. Mefloquine (MEFL, 1379059 Sigma) was administrated once weekly by oral gavage at the dosage of 50 mg/kg. Danusertib (A4116, ApexBio) were injected i.p. daily at the dosage of 15 mg/kg. Arsenic trioxide (A1010, Sigma) was injected i.p. daily at the dosage of 1.9 mg/kg (transferred from 0.15 mg/kg/day for human). Everolimus (A8169, ApexBio) was administrated daily by oral gavage at the dosage of 1 mg/kg. For IIA model, all drug treatments were administrated from the day of injection till the end of experiment unless specifically stated. For spontaneous model, treatments were administrated after resection of primary tumors till the end of experiment.

Bone-in-Culture Array (BICA)

Bone-in-culture samples were set up as previously described (Wang et al., 2017). All the cancer cells used for BICA were labelled by luciferase. After IIA injection, the epiphysis and metaphysis around knee joint of the femurs and tibias were collected and crushed with a sterilized bone plier (F.S.T.16025–14). The generated bone pieces were transferred to low-attachment 96-well plates and cultured in DMEM/F12 media (with 2.438 g/L Sodium Bicarbonate, Gibco Ca#11320-033) with 2% FBS. Medium was changed every 3–4 days. IVIS imaging were performed on 2^{nd} - 3^{rd} week to measure the bioluminescence intensity. BL intensity is normalized to Day 0 signals right after IIA injection unless specified otherwise.

Drug Screening

The John Hopkins University Clinical Compound Library is a generous gift from Dr. Stephen T. C. Wong's laboratory at Houston Methodist Research Institute. 66 anti-neoplasm drugs were selected based on the annotation of compounds. The drug screening was performed as previously reported (Wang et al., 2017). Briefly, BICA samples carrying Fluc$^+$ MCF7 cells were aligned in low-attachment 96-well plates with six replicates per condition. For parallel 2D cultures, MCF7 cells were plated in regular 96-well plates at a density of 500 cells/well. Signals were monitored for 2-3 weeks. In the first screening, 66 anti-neoplasm drugs were randomly grouped at a concentration of 100 nM for each compound (see Table S1). In the secondary screenings, single compounds were tested at 100 nM separately.

Recombinant DNA Generation

Dominant negative CaMKII T286A was cloned from GFP-C1-CAMKIIalpha-T286A (Addgene Cat#21220); Constitutive active CaMKII T286D was cloned from XE118 CAMKII-T286D-CS2+ (Addgene Cat#16736); Dominant negative Calcineurin ΔH161Q was cloned from pET15b CnA CnB (Addgene Cat#11787), mutations introduced by PCR. Wild-type Cx43 and dominant negative Cx43 G138R was cloned from hFOB1.19 cDNA, mutations introduced by PCR.

pInducer22 (a generous gift from Dr. Thomas Westbrook's lab at Baylor College of Medicine) serves as the the backbone of doxycycline-induced overexpression system. The Gateway cloning system (ThemoFisher Scientific) was applied to insert Cx43, E-cadherin, Calcineurin or CaMKII (of wild-type, constitutive active or dominant negative proteins) into pInducer22, following the manufacturer's protocol. To induce gene expression *in vitro* or in BICA, cells were treated with 50-100 ng/ml doxycycline in culture media. To induce gene expression *in vivo*, mice were administrated by 200 mg/L doxycycline in drinking water.

The PWIPZ system (psPAX2 and pMD2,G) was used to introduce Gcamp (carried by pHAGE-RSV-GCaMP6s , #80146, addgene), Cx43, E-cadherin, Calcineurin or CaMKII (carried by pInducer22) or firefly luciferase fused with GFP /RFP (carrie by pWPT) into different cell lines via lentivirus packaging and transduction. Transfection efficiencies were determined by western bolt.

3D Co-culture Assay

For IVIS imaging, a total of 20,000/well luciferase -labeled cancer cells with equivalent number of unlabeled osteogenic cells were cultured in 24-well low-attachment plate with serum-free DMEM/F12 media. The signal of cancer cells were were monitored or 3-7 days through bioluminescence imaging with IVIS Lumina II. Before imaging, sterilized firefly luciferase substrate D-luciferin (LUCNA-1G, Goldbio) was added to the cultures to reach a final concentration of 150 μg/ml.

For IF staining, qPCR or western blots on samples incubated over 48 hr, a total of 250,000/well cancer cells with 50,0000/well osteogenic cells were cultured in 6-well low-attachment plate with serum-free DMEM/F12 media. After 48 hr, organoids were spun down at 500 g for 5 min, rinsed by PBS, and then resuspended for PFA (IF), Trizol (qPCR) or lysis buffer (western blot).

For transient coculture settings (Figures S2D, 4D, and 7E), 500,000 cancer cells were suspended and incubated with/without equal number of osteogenic cells for 3.5 hr in serum and calcium free S-MEM media. After that, 0-2 mM calcium was added along with other inhibitors as designed for 30 min. Cells were spun down at 500 g for 5 min, washed by PBS, and then resuspended in lysis buffer.

Western Blot

Western blots were performed using antibodies against NFAT1(Cell Signalling, 5861S), pS6K(T389) (Cell Signaling, 9234S), pCamKII(T286) (Cell Signalling, 12716S), MeCP2 (Cell Signalling, 3456S), pMeCP2(S421)(Rockland, 600-401-X14), Firefly luciferase (Thermo, PA5-32209). The Electrophoresis and Membrane-Transfer were performed by iBlot (Invitrogen). Imaging was obtained by Odyssey (Li-Cor) system, following the manufacturer's protocol.

Immunofluorsent and Immunohistochemical Staining

On Day 2, the organoids were collected by centrifugation (500 g for 2 mins), fixed in 4% paraformaldehyde, and paraffin embedded. Orthotopic tumor samples were chopped into small chunks and fixed in 4% paraformaldehyde for paraffin embedding. Femur and tibia bones were excised from mice at the end point of each experiment. Mussels were carefully removed by paper towels. BICA or tumor-bearing bone samples were fixed in 4% paraformaldehyde, decalcified in 14% EDTA for 2 weeks, and embedded in paraffin for section. Microtome-sectioning was conducted to prepare 6 μm slides for organoids, othotopic tumor, BICA or bone samples.

Immunofluorescent and immunohistochemical staining was assisted by the BCM Breast Center Pathology Core and performed with the antibody against Cx43 (Sigma, C6219), MeCP2 (Cell Signalling, 3456S) and NFAT (Cell Signalling, 5861S). Sections were deparaffinized and followed by antigen retrieval in 1x citric buffer at 90°C for 10 min. After blocking for 1 hour at RT in blocking buffer (5 % goat serum, 5 % donkey serum, 2 % BSA in PBS-GT), slides were incubated overnight in a humidified chamber at 4°C with primary antibodies. The next day, slides were washed and incubated with Alexa Fluor conjugated secondary antibody (1:250, Jackson ImmunoResearch) for 1 hour at room temperature. Afterwards slides were stained with SlowFade Gold antifade reagent with DAPI (Life technologies, cat # S36936). Washing was performed in PBS between all steps. Immunofluorsent images were obtained using a Leica confocal microscope and ImageJ. Immunohistochemical images were obtained using an Olympus BX50F4 microscope and CellSens. All pictures are representative of at least three biological replicates in each group.

Flow Cytometry

To quantify calcium flow by FACS, cells expressing Gcamp6s were incubated with/without non-Gcamp6s cells for 4 hr in serum and calcium free S-MEM media. After that, 0-2 mM calcium was added along with other inhibitors as designed for 30 min and go for flow. To characterize the Calcein (C3100MP, ThermoFisher) transportation throw gap junction, Osteoblasts were preloaded with Calcein and cocultured with cancer cells for up to 4 hr in DMEM/F12 media before flow. All data were acquired using a BD LSR Fortessa Analyzer and analyzed with Flow Jo v10.0.

MicroCT (μCT) Analysis

For μCT analyzes, hind limb specimens were dissected to remove soft tissues. The bone specimens consisting of the entire femur and tibia were fixed in formaldehyde prior to imaging. The specimens (n=4) were stabilized in a individual holders and kept in ethanol during μCT scanning. To accommodate the length of bone specimens, overscan mode was used which acquired sequentially 7 high-resolution images with a spatial resolution of 6.5 μm (Skyscan1174v2; Bruker, Kontich, Belgium). The X-ray source was set at a voltage of 50kV, a current of 200 μA, and a rotation step at 0.2°. The sequential images were then digitally combined to obtain visualization of the entire femur and tibia. Qualitative analyzes included 2- and 3-dimentional reconstructions performed using NRecon and CTvox software (Bruker, Kontich, Belgium). After determining that the site of most pronounced metastatic destruction occurred in the distal femur and proximal tibia, segments of these bone regions each extending 5mm away from the knee joint space were selected for quantitative analyzes. The region of interest (ROI) were selected, and the gray thresholds of 68 and 120 allowed to calculate total (cancellous and cortical) and cortical bone, respectively. Bone mineral density was assessed using previous calibration against standard mouse density μCT phantoms. μCT results were compares using 1-way ANOVA with Bonferroni-Holm posthoc test for pairwise caparisons. Statistical significance was set at a threshold of 0.05.

RNA Isolation and qRT-PCR Analysis

Total RNAs were extracted from cells using Direct-zol RNA miniPrep kit (Zymo Research) following manufacturer's instructions. RNAs were reverse-transcribed into cDNAs by using Superscript III reverse transcription kit (Invitrogen). Real-time RT-PCR was performed on Biorad CFX connected Real-time system using PowerUp SYBR Green Master Mix (applied biosystems). All real-time RT-PCR assays were performed in at least duplicate in three independent experiments. In 3D assay, human cancer cell and murine MSC were co-cultured. Human-specific primers were used exclusively for gene expression detection in cancer cells. Relative expression values of each target gene were normalized to GAPDH or ACTB mRNA level. The primers are listed in the Key Resources Table.

Chromatin Immunoprecipitation (ChIP)-Assay

Cells were vehicle- or 200 nM As_2O_3 treated for 7 days and harvested for ChIP assay. In brief, DNA/protein complexes were cross-linked using 1% formaldehyde for 10 min, followed by chromatin extraction. Chromatin shearing was performed for 4 cycles of 10 min (30 sec ON/OFF). Pre-cleared samples were immunoprecipitated at 4°C overnight with SP1 antibody (CST # 9389S) or normal rabbit IgG (CST # 2729S) linked to Dynabeads protein G. Beads were sequentially washed 3 times with 1ml of Buffer 1 (50mM Hepes-KOH pH 7.5, 150mM NaCl, 1mM EDTA, 1% Triton X-100, 0.1% sodium deoxycholate, and 0.1% SDS), once with 1ml of Buffer 2 (50mM Hepes pH 7.5, 350mM NaCl, 1mM EDTA, 1% Triton X-100, 0.1% sodium deoxycholate 0.1% SDS), 1ml of Buffer 3 (1mM EDTA, 10mM Tris-HCl pH 8.1, 250mM LiCl, 1mM sodium Deoxycholate, and 1% NP40), and 1ml of Buffer 4 (1x) (1mM EDTA, 10mM Tris-HCl). Chromatin was eluted with 1% SDS buffer, followed by 2 hours protein digestion, and overnight DNA de-crosslinking at 67°C. DNA was purified using a DNA Clean & Concentrator kit (ZYMO # D4013) and used for RT-PCR with the primers FW-SP1-CX43 and RV-SP1-CX43 (see Key Resources Table).

RNA-Seq Experiment

For mice samples, the RNA-seq experiment was performed as previously reported (Wang et al., 2017, Figure S2A). The orthotopic tumor and bone lesion samples were collected 3 weeks after inoculation. Tissues were homogenized by Precellys 24 Homogenizer (Bertin). In 3D assay, human cancer cell and murine MSC were co-cultured in serum-free DMEM/F12 media for 48 hr and centrifuged. Total RNA of either tissues or cells were extracted using the Direct-zol RNA miniprep kit (Zymo Research). The first and second strands of cDNA were prepared by SuperScript III First-Strand Synthesis System and NEBNext mRNA Second Strand Synthesis Module from > 200 ng total RNA/ sample. Sequencing libraries were generated with the Illumina Nextera XT DNA Library Prep Kit (Illumina, San Diego, CA,USA) according to the protocol supplied by the manufacturer. Cluster generation was performed using the Illumina Nextseq 500/550 high output v2 kit and sequenced on the Illumina Nextseq 500 equipment.

The reads containing a mixture of human and mouse reads were separated with *in silico* sorting using Xenome (version 1.0.1). We used the default k-mer size suggested by Xenome (-k 25). After that, the sorted human reads were mapped using STAR RNA-seq aligner (version 2.4.1d). To make full use of the reads not uniquely mapped we used RSEM, which applies estimation maximization to quantify gene and isoform expression. DEseq2 R package was used to normalize the gene/isoform expression matrix. The dataset has been uploaded to GEO with the access number GSE110451.

QUANTIFICATION AND STATISTICAL ANALYSIS

All results are presented in the form of mean±s.e.m. or mean±s.d. Sample sizes for *in vivo* experiments are noted in the corresponding figures or figure legends. Log-transformation were performed to achieve better visualization for samples with large standard deviation. Differences among growth curves and IC_{50} inhibition curves were assessed using repeated measure analysis of variance tests. In experiments containing two groups, 2-tailed student's t-tests were performed with the assumption of equal variation. In experiments consisting of more than two groups, the differences between means of different experimental groups were analyzed using LSD tests. Results using other statistical analysis were noted in respective legends.

Gene Set Variation Analyses were performed using the GSVA package of the R program (Hänzelmann et al., 2013). Default settings are used. Transcription factor target gene sets were downloaded from the MSigDB database (the C3 TFT collection) (Subramanian et al., 2005). The generated GSVA scores of each pathway were compared between bone metastases and other metastases in GSE: GSE14020 using the SAM package of R. In some analyses, we re-scaled GSVA scores linearly between 0 and 1 by (max_score – gsva.score_i)/(max_score – min_score), where gsva_score_i represents the score of the i'th tumor, and max_ and min_scores represent the maximum and minimum scores of all tumors, respectively.

Survival analyses were performed using the ''survival'' package of the R program. The ''survdiff'' function was used to compute log-rank p values between different groups. And the ''survfit'' function was used to generate Kaplan-Meier curves.

For all boxplots, the line inside the box is the median value; top/bottom bars of the box show $75^{th}/25^{th}$ percentile; the upper/lower whiskers show largest/smallest values no further than 1.5 x inter-quartile range from the hinge; data points beyond whiskers are possible outliers.

DATA AND SOFTWARE AVAILABILITY

The *in vivo* Bone Lesion (IVBL) and Orthotopic tumors dataset is available in NIH Gene Expression Omnibus with the accession number GSE110451.

The dataset of ATO treatment on mesenchymal stem cells (MSCs) interacting breast cancer cells is available in NIH Gene Expression Omnibus with the accession number GSE118923.

The Mendeley Dataset of this manuscript is available at: https://doi.org/10.17632/bbbz577rx8.1.

Codes data analysis by R programming is available at: https://github.com/lethesea/Targeting-calcium-signaling-in-bone-micrometastases.

Cancer Cell, Volume *34*

Supplemental Information

The Osteogenic Niche Is a Calcium Reservoir of Bone Micrometastases and Confers Unexpected Therapeutic Vulnerability

Hai Wang, Lin Tian, Jun Liu, Amit Goldstein, Igor Bado, Weijie Zhang, Benjamin R. Arenkiel, Zonghai Li, Meng Yang, Shiyu Du, Hong Zhao, David R. Rowley, Stephen T.C. Wong, Zbigniew Gugala, and Xiang H.-F. Zhang

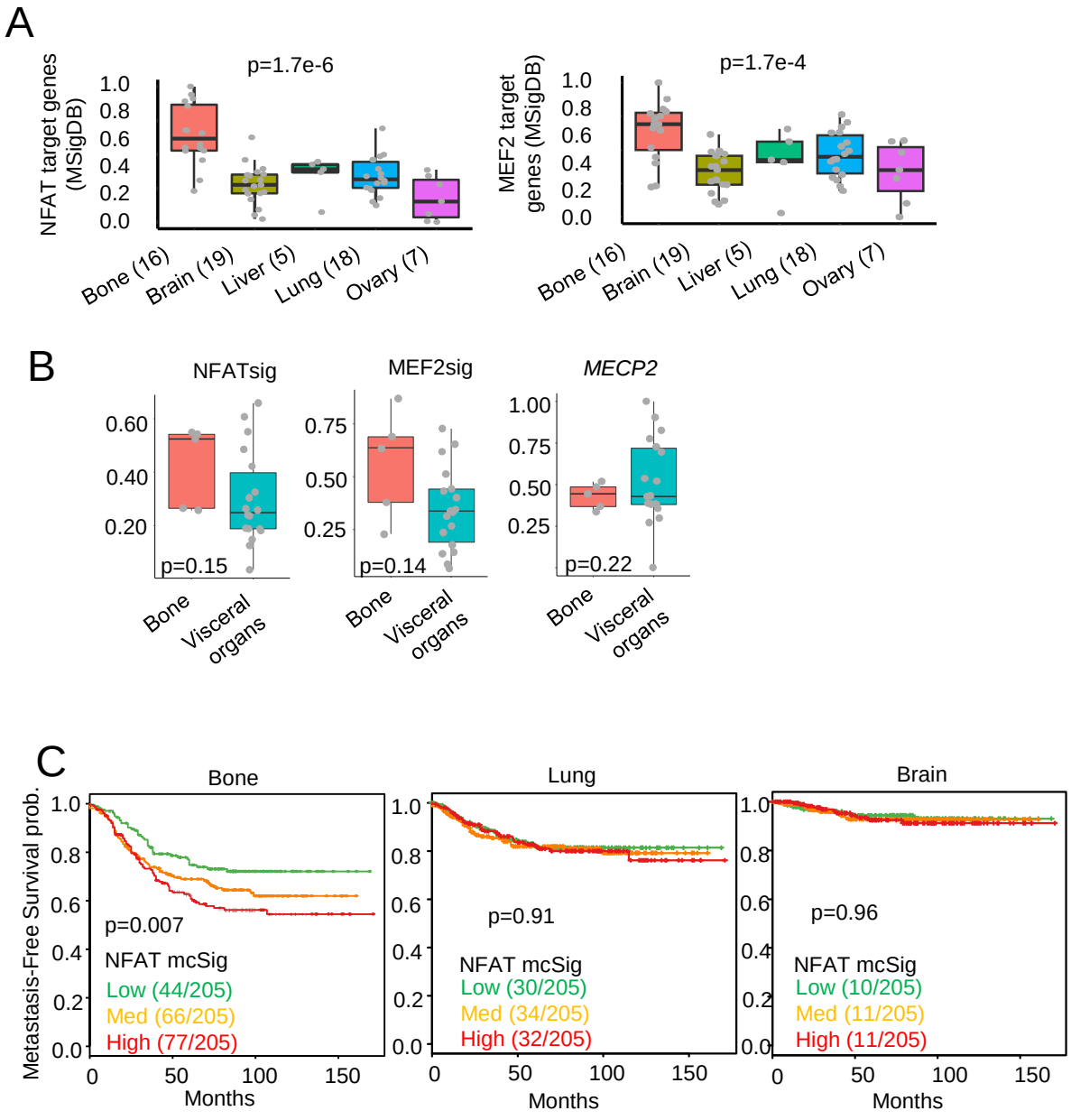
A
NFAT target genes (MSigDB)
p=1.7e-6
1.0
0.8
0.6
0.4
0.2
0.0
Bone (16)
Brain (19)
Liver (5)
Lung (18)
Ovary (7)
MEF2 target genes (MSigDB)
p=1.7e-4
B
NFATsig
MEF2sig
MECP2
0.60
0.40
0.20
p=0.15
0.75
0.50
0.25
p=0.14
1.00
0.75
0.50
0.25
p=0.22
Bone
Visceral organs
C
Bone
Lung
Brain
Metastasis-Free Survival prob.
p=0.007
NFAT mcSig
Low (44/205)
Med (66/205)
High (77/205)
p=0.91
Low (30/205)
Med (34/205)
High (32/205)
p=0.96
Low (10/205)
Med (11/205)
High (11/205)
0
50
100
150
Months

Figure S1. Calcium signaling is enriched in bone metastasis compared to metastases in other organs, Related to Figure 1.

(**A**) Boxplots show the expression of NFAT and MEF2 (GSVA scores) across human breast cancer metastases (GSE14020) in different organs. Numbers in parentheses indicate sample size of each group. p values were calculated by one-way ANOVA.

(**B**) Boxplots show the expression of NFAT / MEF2 target genes and *MECP2* between bone metastases and visceral metastases (GSE46141). p values were computed by Student's t tests.

(**C**) Kaplan-Meier plots of the probability of bone, lung and brain metastasis-free survival in a combined Erasmus/MSKCC dataset (GSE2603, 5327, 2034, and 12276) in relation to the mcSig-predicted NFAT activity. All patients are divided into three groups of equal numbers with low-, medium- and high-activity of mcSig NFAT signature. The number of diagnosed metastasis events and the total number of patients are indicated for each analysis. p value was calculated according to log rank test.

For all boxplots: line inside the box: median value; top/bottom of the box: 75^{th}/25^{th} percentile; upper/lower whiskers: largest/smallest values no further than 1.5 x inter-quartile range from the hinge; data points beyond whiskers: possible outliers. Same for the boxplots in other figures.

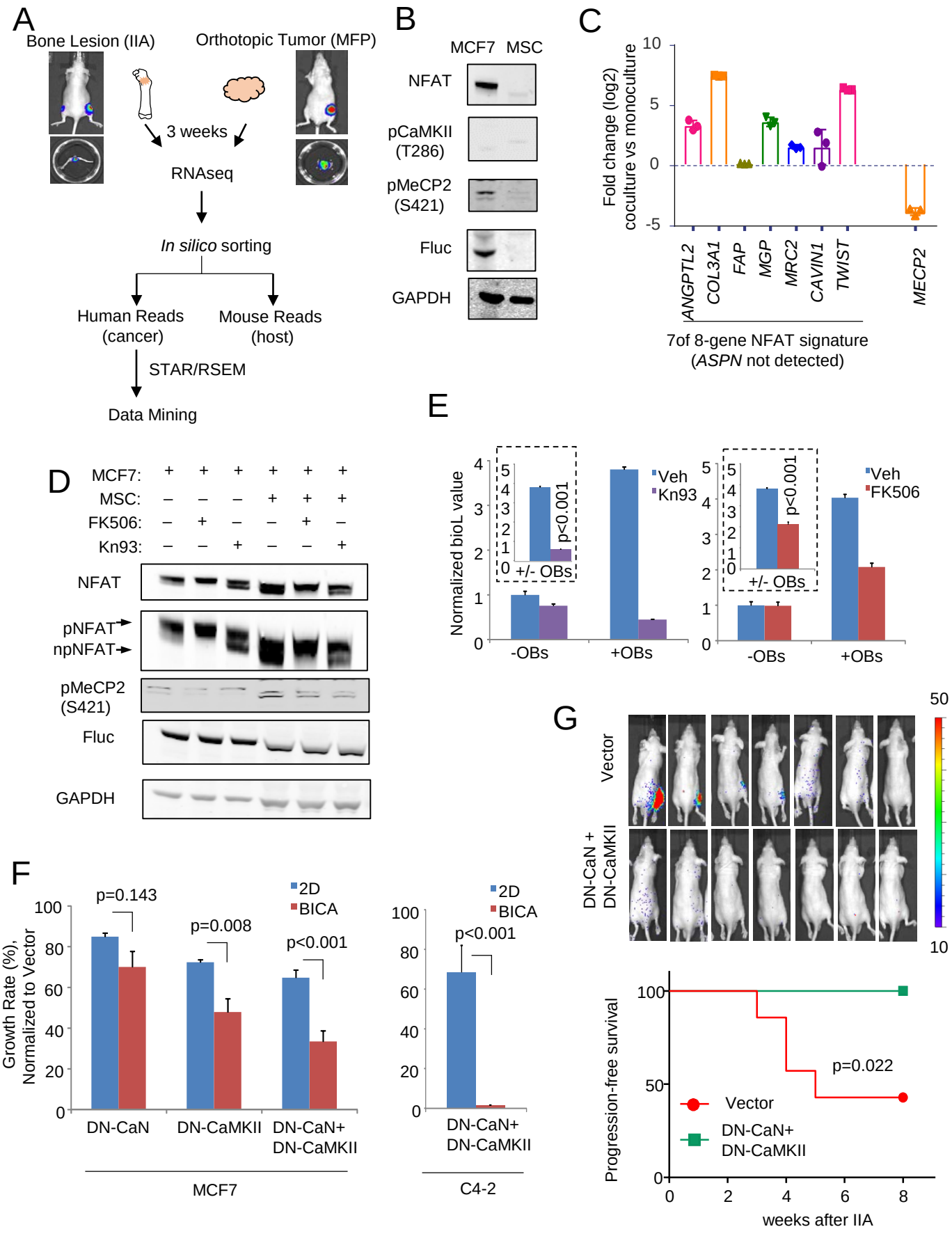
A
Bone Lesion (IIA)
Orthotopic Tumor (MFP)
3 weeks
RNAseq
In silico sorting
Human Reads (cancer)
Mouse Reads (host)
STAR/RSEM
Data Mining
B
MCF7 MSC
NFAT
pCaMKII (T286)
pMeCP2 (S421)
Fluc
GAPDH
C
Fold change (log2) coculture vs monoculture
ANGPTL2
COL3A1
FAP
MGP
MRC2
CAVIN1
TWIST
MECP2
7of 8-gene NFAT signature (ASPN not detected)
D
MCF7:
MSC:
FK506:
Kn93:
NFAT
pNFAT
npNFAT
pMeCP2 (S421)
Fluc
GAPDH
E
Normalized bioL value
Veh
Kn93
FK506
p<0.001
+/- OBs
-OBs
+OBs
F
Growth Rate (%), Normalized to Vector
2D
BICA
p=0.143
p=0.008
p<0.001
DN-CaN
DN-CaMKII
DN-CaN+ DN-CaMKII
MCF7
C4-2
G
Vector
DN-CaN + DN-CaMKII
Progression-free survival
p=0.022
Vector
DN-CaN+ DN-CaMKII
weeks after IIA

Figure S2. Experimental models recapitulate the enhancement of calcium signaling in cancer cells interacting with the bone microenvironment, Related to Figure 2.

(**A**) The pipeline of next-generation RNA sequencing and transcriptomic profiling performed to generate GSE110451. IIA: intra-iliac artery injection. MFP: mammary fat pad injection.

(**B**) Western blot on the basal level of the indicated proteins / phosphor-proteins in cancer cells or MSCs without co-culture or inhibitor treatment.

(**C**) The expression of NFAT signature and *MECP2* gene in human MCF7 cells in co-culture with murine MSCs, as detected by real-time PCR. Human-specific primers were used to exclude transcripts from mMSC and measure only transcripts in cancer cells . All NFAT signature genes were detected except for *ASPN*. Log2-transformed fold change (FC, co-culture over mono-culture) is plotted. Three biological replicates are included. Error bars = S.D.

(**D**) Western blot shows the expression of NFAT and phosphor-MeCP2 at Ser 421 with or without treatments of 10 μM Kn93 or 10 μM FK506 after mono- or coculture for 4 hr. The shift between pNFAT and npNFAT is highlighted in a separate row with stretched height/width ratio. Firefly luciferase (Fluc) was used as loading control exclusively for cancer cells.

(**E**) Bar graphs show the quantification of firefly luciferase-labeled MCF7 cells with or without co-culture of equal number of OBs in 3D suspension cultures under treatments of 10 μM Kn93 or 10 μM FK506. BL signals were measured on Day 5 and normalized to untreated MCF7 cells without OBs. n=3 technical replicates. The fold change between +OB and –OB conditions (+/–OB) is calculated for each condition and shown in the box of dotted line. Error bars = S.D.

(**F**) Related to Figure 2H and 2I. Bar graph shows the growth rate change of MCF7 and C4-2 cells expressing DN-CaN, DN-CaMKII, and both (DN-CaN+DN-CaMKII). BL signals were normalized to empty vector group in either 2D or BICA culture. n=8 wells/group for 2D culture; n=12 bone fragments/group for BICA. Error bars = S.D. p value by Student's t test for E and F.

(**G**) Top: BL pictures of of IIA-injected C4-2 prostate cancer cells, either expressing empty vector or DN-CaN + DN-CaMKII. n=7 for both groups. BL signals were measured on the 6^{th} week after IIA injection. Bottom: Kaplan-Meier curves of the indicated groups. The end point is defined as the time point when detectable hind limb signal intensity was observed and continues to increase at subsequent time points. p value was based on a log-rank test.

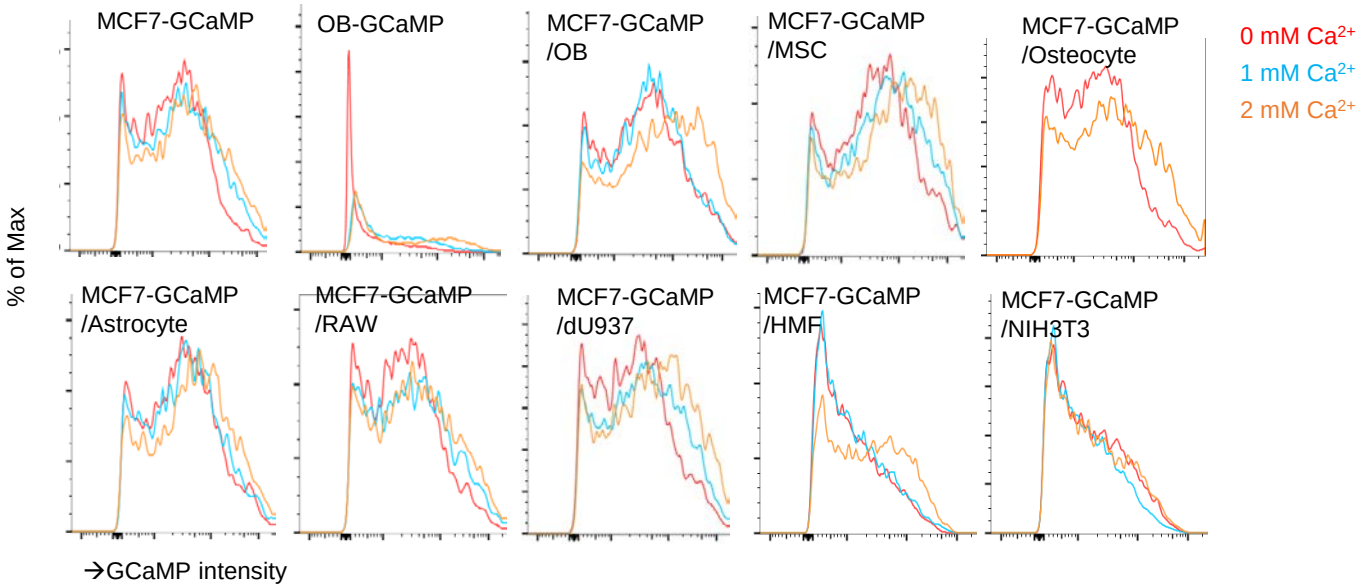

Figure S3. Calcium flows from osteogenic cells to cancer cells , Related to Figure 3.

Intensity curves of GCaMP under 0 mM, 1 mM and 2 mM [Ca^{2+}] in the indicated group.

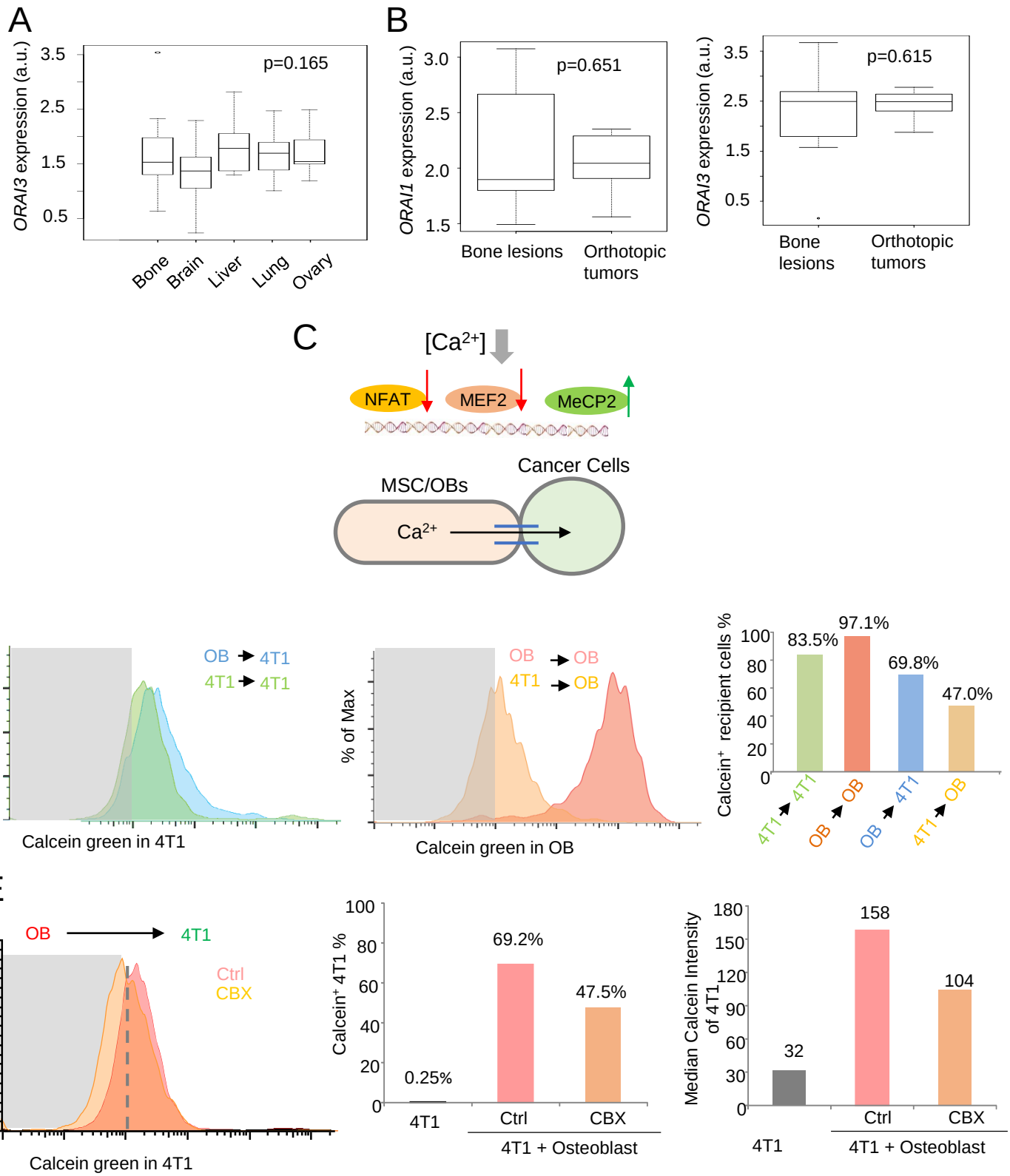
A
ORAI3 expression (a.u.)
3.5
2.5
1.5
0.5
p=0.165
Bone
Brain
Liver
Lung
Ovary
B
ORAI1 expression (a.u.)
3.0
2.5
2.0
1.5
p=0.651
Bone lesions
Orthotopic tumors
ORAI3 expression (a.u.)
3.5
2.5
1.5
0.5
p=0.615
Bone lesions
Orthotopic tumors
C
[Ca2+]
NFAT
MEF2
MeCP2
Cancer Cells
MSC/OBs
Ca2+
D
% of Max
OB → 4T1
4T1 → 4T1
Calcein green in 4T1
% of Max
OB → OB
4T1 → OB
Calcein green in OB
Calcein+ recipient cells %
100
80
60
40
20
0
83.5%
97.1%
69.8%
47.0%
4T1 → 4T1
OB → OB
OB → 4T1
4T1 → OB
E
OB → 4T1
Ctrl
CBX
% of Max
Calcein green in 4T1
Calcein+ 4T1 %
100
80
60
40
20
0
0.25%
69.2%
47.5%
4T1
Ctrl
CBX
4T1 + Osteoblast
Median Calcein Intensity of 4T1
180
150
120
90
60
30
0
32
158
104
4T1
Ctrl
CBX
4T1 + Osteoblast

Figure S4. Gap junction mediates the calcium flow from osteogenic cells to cancer cells, Related to Figure 4.

(**A**) Box-whisker plot shows *ORAI3* gene expression across metastases in different organs (GSE14020). *ORAI1* was not detected in this dataset. p value was computed by one-way ANOVA.

(**B**) Box-whisker plots show *ORAI1* and *ORAI3* expression in bone lesions or orthotopic tumors derived from MCF7 cells. p value was computed by Wilcoxon tests.

(**C**) Schematic illustration of the conclusion based on Figure 4E.

(**D**) Calcein green assay of small molecule transfer through gap junctions in culture of 4T1 cells and OBs. Negative control (no calcein green) is indicated by grey area. The direction of transfer and percent positive recipient cells are indicated.

(**E**) The same as Figure 4G except that murine breast cancer cell 4T1 was used instead of human breast cancer cell MCF7. .

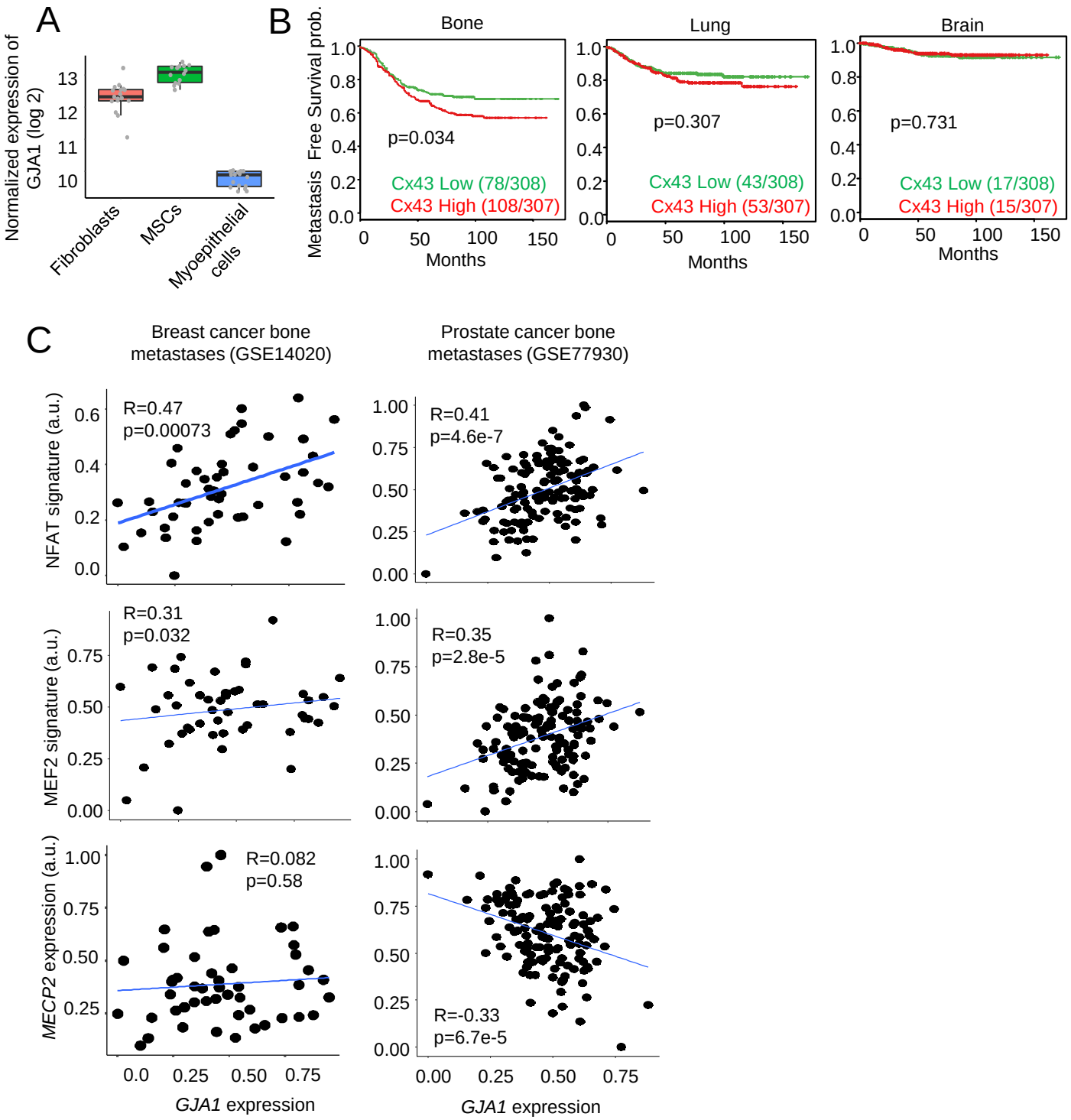
A
Normalized expression of GJA1 (log 2)
13
12
11
10
Fibroblasts
MSCs
Myoepithelial cells
B
Bone
Lung
Brain
Metastasis Free Survival prob.
1.0
0.8
0.6
0.4
0.2
0.0
p=0.034
Cx43 Low (78/308)
Cx43 High (108/307)
p=0.307
Cx43 Low (43/308)
Cx43 High (53/307)
p=0.731
Cx43 Low (17/308)
Cx43 High (15/307)
0
50
100
150
Months
C
Breast cancer bone metastases (GSE14020)
Prostate cancer bone metastases (GSE77930)
NFAT signature (a.u.)
R=0.47
p=0.00073
R=0.41
p=4.6e-7
MEF2 signature (a.u.)
R=0.31
p=0.032
R=0.35
p=2.8e-5
MECP2 expression (a.u.)
R=0.082
p=0.58
R=-0.33
p=6.7e-5
GJA1 expression
GJA1 expression

Figure S5. Connexin 43 (Cx43) is the major constituent of gap junction, Related to Figure 5.

(**A**) Boxplot shows the expression level of *GJA1* (encoding Cx43) in different stromal cells. p values were computed by one-way ANOVA. Data are based on GSE29036.

(**B**) Kaplan-Meier plots of the probability of bone, lung and brain metastasis-free survival in the combined Erasmus/MSKCC dataset in relation to the *GJA1* (encoding Cx43) expression. All patients are divided into two groups of equal numbers with low- and high-expression of Cx43. The number of diagnosed metastasis events and the total number of patients are indicated for each analysis. p value was calculated according to log rank test.

(**C**) Scatter plots show the correlations between Cx43 (*GJA1*) expression and the NFAT signature (Tripathi et al., 2014), the MEF2 signature (Di Giorgio et al., 2017), as well as *MECP2* single gene expression in non-bone metastasis lesions. All values were linearly re-scaled to between 0 and 1. Linear regression trend lines are shown as blue lines. Pearson correlation coefficients and p values based on Student's t tests are shown.

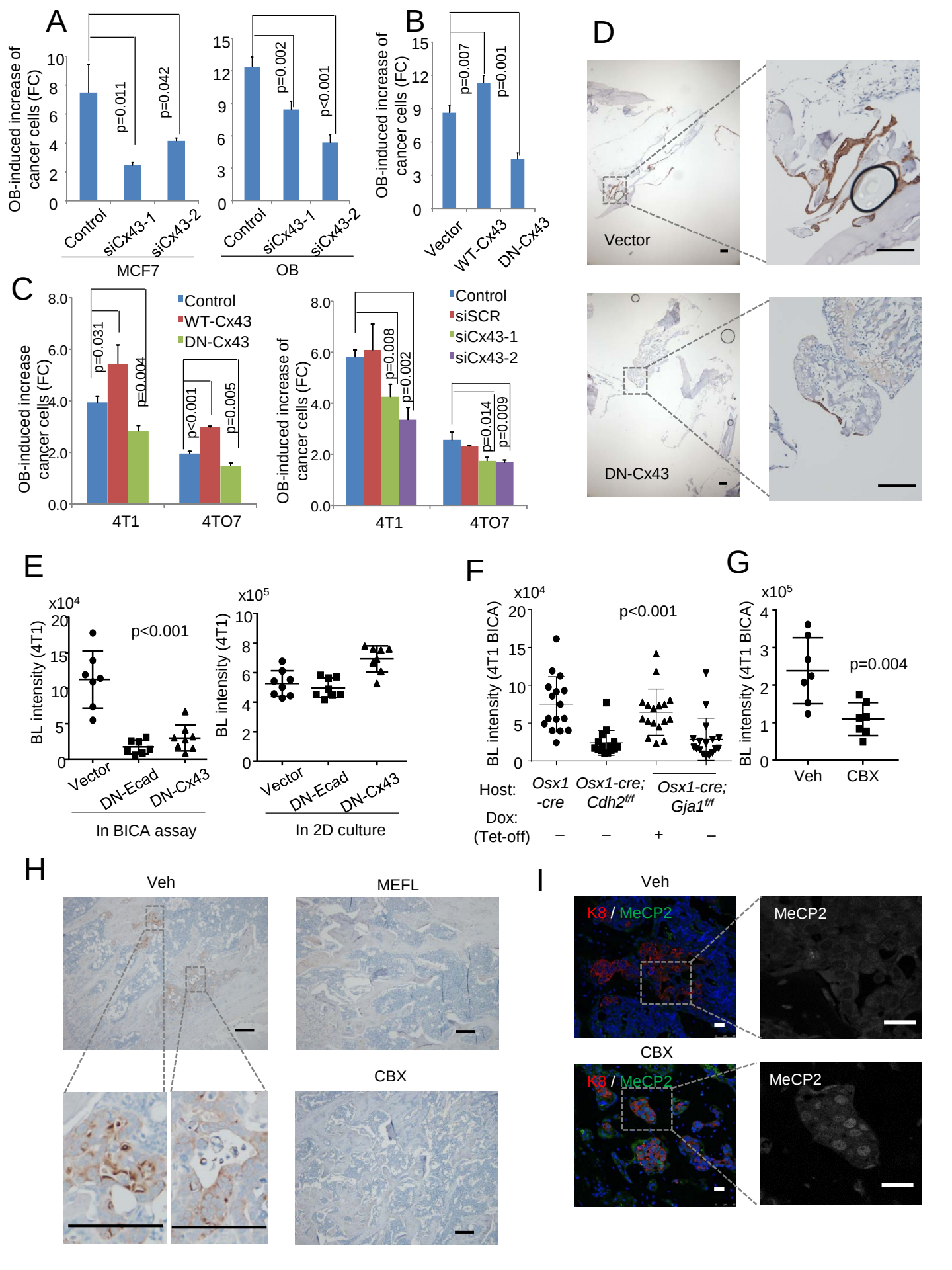
A
OB-induced increase of cancer cells (FC)
p=0.011
p=0.042
p=0.002
p<0.001
Control
siCx43-1
siCx43-2
MCF7
OB
B
p=0.007
p=0.001
Vector
WT-Cx43
DN-Cx43
C
Control
WT-Cx43
DN-Cx43
siSCR
siCx43-1
siCx43-2
p=0.031
p=0.004
p<0.001
p=0.005
p=0.008
p=0.002
p=0.014
p=0.009
4T1
4TO7
D
Vector
DN-Cx43
E
BL intensity (4T1)
p<0.001
Vector
DN-Ecad
DN-Cx43
In BICA assay
In 2D culture
F
BL intensity (4T1 BICA)
p<0.001
Host:
Osx1 -cre
Osx1-cre; Cdh2f/f
Osx1-cre; Gja1f/f
Dox: (Tet-off)
G
BL intensity (4T1 BICA)
p=0.004
Veh
CBX
H
Veh
MEFL
CBX
I
Veh
K8 / MeCP2
MeCP2
CBX

Figure S6. Inhibition of Cx43 and gap junctions retarded bone colonization, Related to Figure 6.

(**A-B**) Quantification of firefly luciferase-labeled MCF7 cells with or without coculture of equal numbers of osteoblasts under different treatments of siRNAs against Cx43 (siCx43) in MCF7 (A, left) and osteoblasts (A, right), or doxycycline (Dox) to induce the expression of DN-Cx43 in cancer cells (B). BL signals were measured on day 5 to allow the treatments to take effects, and normalized to untreated MCF7 cells without OBs. Error bars = S.D. (n=3-5 technical replicates). p value was calculated by LSD test.

(**C**) Same as Figure S6A and S6B except that murine breast cancer cell lines 4T1 and 4TO7 were used instead of human breast cancer cell MCF7.

(**D**) Representative IHC staining of BICA samples derived from Figure 6A. Multiple bone fragments are shown in the same field. Scale bar, 100 μm. Keratin 8 (K8, brown) was stained to distinguish cancer cells. High magnification pictures are shown to highlight Keratin 8 positive cancer cells.

(**E**) Left: Same as Figure 6A except that murine breast cancer cell 4T1 expressing DN-Ecad or DN-Cx43 was used instead of human breast cancer cell MCF7. Right: Result of a parallel 2D culture experiment is shown. n=7-8 for each group. Error bars: S.D. p value by Student's t test.

(**F**) Quantification of tumour burdens in BICA in host mice with inducible and conditional KO of *Cdh2* or *Gja1* in osteogenic cells (Osterix^{+} cells and descendent cells). Conditions are the same as Figure 6C except that murine breast cancer cell 4T1 was used instead of human breast cancer cell MCF7. n=16 for each group. Error bars: S.D. p value by Student's t test.

(**G**) The effects of CBX (10 μM) on 4T1 cells in BICA. n=7 bone fragments in each group. Samples are under corresponding treatment for 1 weeks. p values were determined by Student's t-test. Error bars: S.D.

(**H**) Representative IHC staining of bone lesions derived from Figure 6G-I. Scale bar, 100 μm. High magnification pictures are shown to highlight Keratin 8 (K8, brown) positive cancer cells.

(**I**) IF staining of MeCP2 (green) in shown in bone lesions with or without CBX treatment. Keratin 8 (K8, red) was also stained to distinguish cancer cells. Single channel, high magnification pictures of MeCP2 staining are shown to highlight nuclear localization. Scale bar, 25 μm.

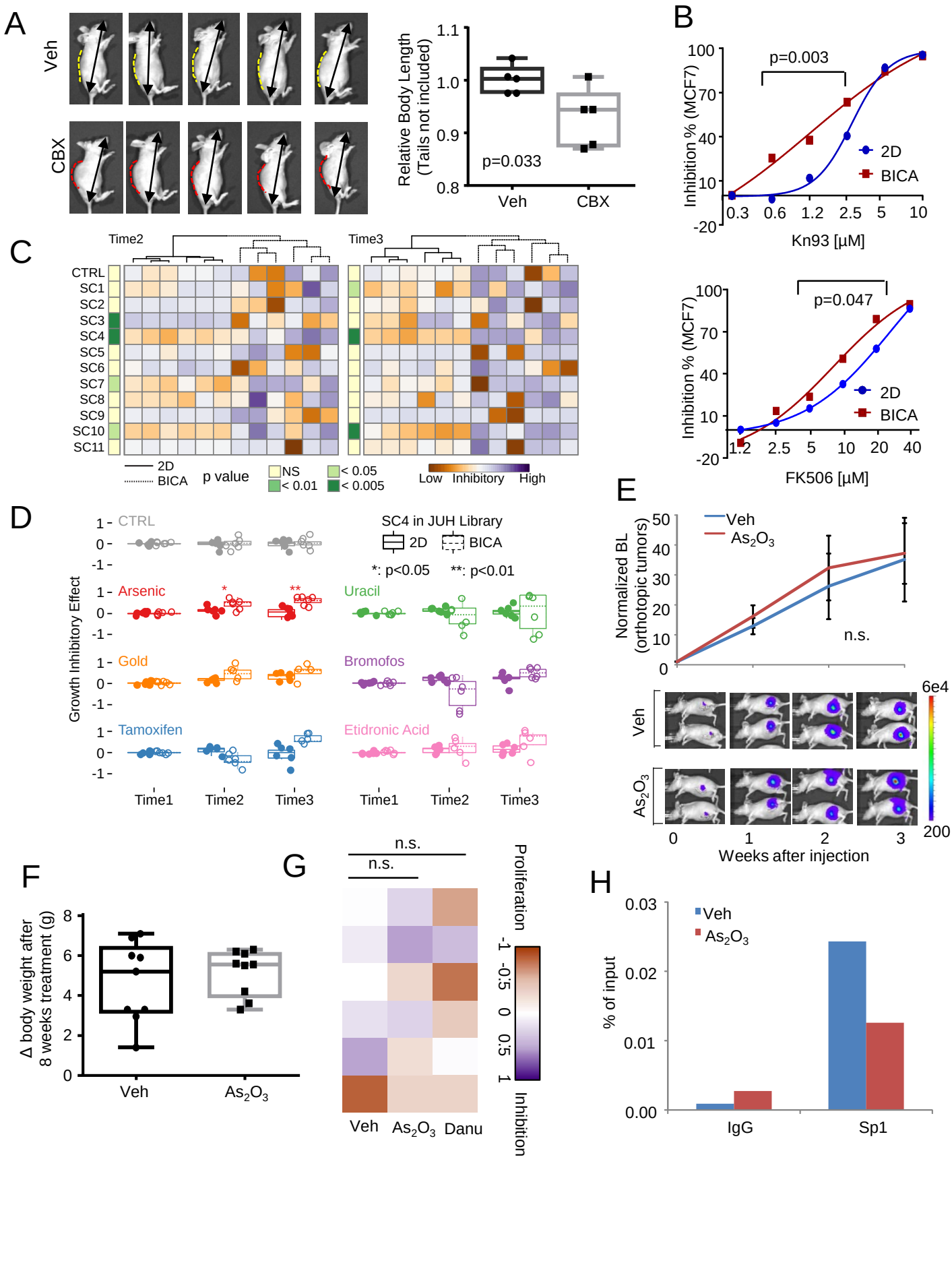
A
Veh
CBX
Relative Body Length (Tails not included)
1.1
1.0
0.9
0.8
p=0.033
Veh
CBX
B
p=0.003
Inhibition % (MCF7)
100
70
40
10
-20
0.3
0.6
1.2
2.5
5
10
Kn93 [μM]
2D
BICA
p=0.047
1.2
2.5
5
10
20
40
FK506 [μM]
C
Time2
Time3
CTRL
SC1
SC2
SC3
SC4
SC5
SC6
SC7
SC8
SC9
SC10
SC11
2D
BICA
p value
NS
< 0.01
< 0.05
< 0.005
Low
Inhibitory
High
D
SC4 in JUH Library
2D
BICA
*: p<0.05
**: p<0.01
Growth Inhibitory Effect
CTRL
Arsenic
Gold
Tamoxifen
Uracil
Bromofos
Etidronic Acid
Time1
Time2
Time3
E
Normalized BL (orthotopic tumors)
Veh
As2O3
n.s.
Veh
As2O3
6e4
200
0
1
2
3
Weeks after injection
F
Δ body weight after 8 weeks treatment (g)
Veh
As2O3
G
n.s.
n.s.
Proliferation
Inhibition
Veh
As2O3
Danu
H
% of input
Veh
As2O3
IgG
Sp1

Figure S7. BICA-screening identified As_2O_3 and danusertib as candidate therapies to eliminate cancer cells interacting with osteoblasts, Related to Figure 7.

(**A**) Pictures and quantification of length from head to tail as a surrogate measurement of vertebral curvature caused by the side effect of 30 mg/kg CBX treatment for 4 weeks. n=5 for each group. p value was calculated by Student's t-test.

(**B**) Dose–response curves of Kn93 (up) and FK506 (below) on MCF7 cells in BICA or 2D cultures. For 2D cultures, six technical replicates were included for each drug concentration. For BICA, n=5 bone fragments for each drug concentration. Samples are under corresponding treatment for 7 days and measured by BL. p values were determined by repeated measures ANOVA tests for the indicated concentration.

(**C**) A heat map summarizing the output of first-round testing using JH anti-neoplasm drugs. (See Table S1 for detailed information on each group.) MCF7 samples are under corresponding treatment for 3 weeks and measured by bioluminescence. Each column represents an independent cell culture (2D) or bone fragment (BICA). p values were determined by two-tailed unpaired Mann–Whitney U-test.

(**D**) Results of the second-round test on Group SC4. Samples are under corresponding treatment for 3 weeks and measured by bioluminescence. CTRL, control. p value was determined by two-tailed unpaired Mann–Whitney U-test with multiple-test correction. n=6 bone fragments in each group.

(**E**) Top: The effects of As_2O_3 on mammary fat pad-injected MCF7 orthotopic tumors. Growth curves were measured by *in vivo* BL imaging. n=5 mice per group. Error bars: S.E.M. Bottom: representative BL images. n.s.: not significant based on repeated measures ANOVA test.

(**F**) Boxplot shows the body weight change with or without 1.9 mg/kg Arsenic treatment for 8 weeks. n=9 for each group. No statistical difference was observed.

(**G**) A heatmap indicates the effects of As_2O_3 [100 nM] and Danu [100 nM] on normal tumor-free bone fragments derived from luciferase transgenic mice. n=6 for each group. n.s.: not significant based on Student's t tests.

(**H**) Sp1 binding to the promoters *GJA1*, as determined by ChIP assay. qPCR shows diminished Sp1 binding on the *GJA1* promoter after arsenic (0.2 μM for 7 days) exposure. IgG serves as control. Mean values of 3 technical replicates are shown.

Table S1, Related to Figure 7.

Group	Names of Modulators					
SC1	mercaptopurine monohydrate	flutamide	quinaldine blue	sulindac	fazarabine	
SC2	amifostine	gallium	samarium	verteporfin	tegafur	nocodazole
SC3	anthracene 0.17%	gemcitabine	streptozocin	alitretinoin	cyproterone acetate	etidronatetidronate disodium
SC4	arsenic	gold	tamoxifen	uracil	bromofos	etidronic acid
SC5	carboplatin	hydroxyurea	temozolomide	amsacrine	nilutamide	raloxifene
SC6	carmustine	letrozole	thioguanine	cycloheximide	polyurethane	sodium fluoride
SC7	chlorambucil	lomustine	thiourea 2.5	decitabine, 5-aza-2'-deoxycytidine	cyclophosphamide	risedronate
SC8	cytarabine	mechlorethamine	toremifene	miltefosine	etoposide	clodronic acid
SC9	dacarbazine	mitotane	vinorelbine	mitobronitol	mercaptopurine	glucosamine
SC10	diethylstilbestrol dipropionate	phenanthrene 0.63%	diethylstilbestrol	puromycin	ancitabine hydrochloride	
SC11	eflornithineflornithine hydrochloridefl ornithine	procarbazine	histamine	semustine	thiodiglycol	

Names and grouping information of the anti-neoplasm drugs used in multiple parallel test on BICA. The grouping was performed in the first round of test, whereas individual drugs from most effective groups were tested in the second round.

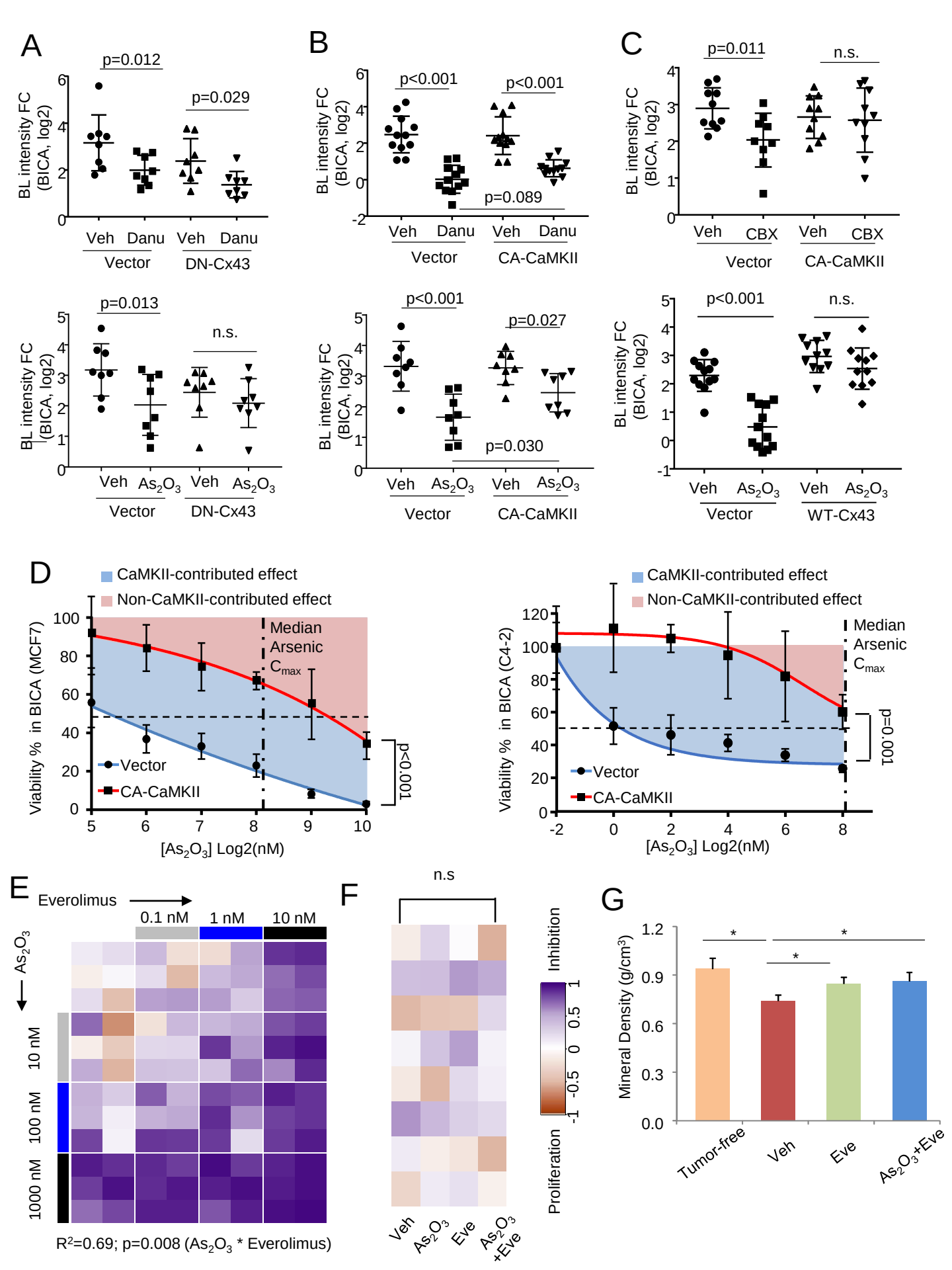
A
p=0.012
p=0.029
BL intensity FC (BICA, log2)
Veh
Danu
Veh
Danu
Vector
DN-Cx43
p=0.013
n.s.
Veh
As2O3
Veh
As2O3
Vector
DN-Cx43
B
p<0.001
p<0.001
p=0.089
Veh
Danu
Veh
Danu
Vector
CA-CaMKII
p<0.001
p=0.027
p=0.030
Veh
As2O3
Veh
As2O3
Vector
CA-CaMKII
C
p=0.011
n.s.
Veh
CBX
Veh
CBX
Vector
CA-CaMKII
p<0.001
n.s.
Veh
As2O3
Veh
As2O3
Vector
WT-Cx43
D
CaMKII-contributed effect
Non-CaMKII-contributed effect
Median Arsenic Cmax
Viability % in BICA (MCF7)
Vector
CA-CaMKII
p<0.001
[As2O3] Log2(nM)
CaMKII-contributed effect
Non-CaMKII-contributed effect
Median Arsenic Cmax
Viability % in BICA (C4-2)
Vector
CA-CaMKII
p=0.001
[As2O3] Log2(nM)
E
Everolimus
0.1 nM
1 nM
10 nM
As2O3
10 nM
100 nM
1000 nM
R2=0.69; p=0.008 (As2O3 * Everolimus)
F
n.s
Inhibition
Proliferation
Veh
As2O3
Eve
As2O3 +Eve
G
Mineral Density (g/cm3)
Tumor-free
Veh
Eve
As2O3+Eve

Figure S8. Adjuvant transient As_2O_3 treatment of reduced latent bone recurrence of ER^+ breast cancer, Related Figure 8.

(**A**) Efficacies of 50 nM Danusertib (Danu, top) or 200 nM As_2O_3 (bottom) on MCF7 cells in BICA with or without overexpression of dominant negative Cx43 (DN-Cx43). Error bars = S.D. n=8 for each group. p values were based on LSD tests.

(**B**) Efficacies of 50 nM Danusertib (top) or 200 nM As_2O_3 (bottom) on MCF7 cells in BICA with or without overexpression of constitutive active CaMKII (CA-CaMKII). Error bars = S.D. n=12 (top) or 8 (bottom) for each group. p values were based on LSD tests.

(**C**) Top: efficacies of 10 μM CBX on MCF7 cells in BICA with or without overexpression of constitutive active CaMKII. Bottom: efficacies of 200 nM As_2O_3 on MCF7 cells in BICA with or without expression of wild-type Cx43 (WT-Cx43). Error bars = S.D. n=10 for each group. p values were based on LSD tests.

(**D**) Dose–response curves of As_2O_3 on MCF7 cells (left) and C4-2 cells (right) in BICA with or without overexpression of constitutive active CaMKII. Six biological replicates were included for each drug concentration. C_{max}: plasma maximum concentration. BL intensity was measured on Week 2-3. n=6 (left) or 5 (right) for each dot. p values were determined by repeated measures ANOVA tests for the indicated concentration. Error bars = S.E.M.

(**E**) A heat map summarizing the output of combined treatment of As_2O_3 and everolimus at different concentration and combination in BICA. MCF7 samples are under corresponding treatment for 3 weeks and measured by bioluminescence. n=6 for each condition. The P and R values are determined by Between-Subjects Effects test, indicating that combined therapy shows advantage over single drug treatment.

(**F**) A heat map showing the toxicity conferred by 100 nM As_2O_3 and 10 nM Everolimus on luciferase-labelled cancer-free bone tissues in BICA. n=8 for each group. p values were determined by one-way ANOVA test.

(**G**) Bar graphs show the quantification of bone mineral density change under different treatment. n=4 samples picked for each group. p value was calculated by Bonferroni-Holm Posthoc test. *: Significant difference. Error bars = S.D.

n.s.: not significant